CHARACTERIZATION OF MATERIAL BEHAVIOR DURING THE MANUFACTURING PROCESS OF A CO-EXTRUDED SOLID OXIDE FUEL CELL

A Thesis
Presented to
The Academic Faculty

by

Prescott L. Eisele

In Partial Fulfillment
of the Requirements for the Degree
Master of Science in Mechanical Engineering

Georgia Institute of Technology
Atlanta, Georgia

April, 2004

CHARACTERIZATION OF MATERIAL BEHAVIOR DURING THE MANUFACTURING PROCESS OF A CO-EXTRUDED SOLID OXIDE FUEL CELL

Approved by:

Dr. David L. McDowell, Chairman

Dr. Joe K. Cochran, Jr.

Dr. Kon Jiun (Jim) Lee

Dr. Richard W. Neu

Date Approved: 4/7/2004

This thesis is dedicated in loving memory

of

John Wilbur Sleeper,

A great husband, father, and grandfather

ACKNOWLEDGEMENTS

First I would like to thank my advisor, Dr. David McDowell, with whom I have had the privilege of working with for the past three and a half years. Dr. McDowell has helped me through an array of challenging problems and given me substantial insight into the field of engineering. Secondly, I would like to thank Dr. Jim Lee who spent an enormous amount of time helping me in every aspect of my research and professional life. Jim would patiently let me bounce lousy idea after lousy idea off of him until I finally got something worth writing down. Jim would always come through for me, whether it was to fix something I broke or to buy me a part I needed on short notice. Third, I would like to thank Dr. Cochran, who was always willing to listen and always had an open door. I would also like to thank Dr. Neu for the effort he put into my committee.

I would like to thank Rajesh Kumar for his patience in explaining most of the field of mechanics to me, and Raymond Oh for all the great samples he made me. I would also like to thank Justin Clark and Ben Church for their help.

I would like to thank all of my friends and roommates for their support and friendship, especially Matt Colgan, Paarin Mehta, Chris (Jessi) Patton, Bart Debacker, and Kevin Recchi. I would like to pay a special thanks to Abra Hewell, who put up with all my whining and was always my number one fan. Thank you Abra.

Finally, I would like to thank any person who actually reads this thesis in its entirety.

TABLE OF CONTENTS

Acknowledgements **iv**

List of Tables **vii**

List of Figures **viii**

Summary **xvi**

Chapter I Background **1**
- I.1 Introduction to Fuel Cells 1
- I.2 Inherent Problems with Solid Oxide Fuel Cells 4
- I.3 Powder Processing 5
- I.4 Terminology 6
- I.5 Overview of the Powder Process: Advantages and Disadvantages 9
- I.6 Motivation for Modeling 15
- I.7 Existing Models 21
- I.8 Problems with Existing Models: Motivation 23

Chapter II Experimental Methodology **25**
- II.1 Porosity Experiments 25
- II.2 Sintering Measurements 28
- II.3 Reduction Measurements 35
- II.4 Characterization of Mechanical Properties 57
- II.5 Characterization of Reduction and Sintering Measurements 72

Chapter III The Model **84**
- III.1 Fundamentals of the Model 84
- III.2 Assumptions and Differences Between Electrolyte and Metal Interconnect Models 86
- III.3 The Electrolyte Model 90
  - III.3.1 Thermal Expansion 90
  - III.3.2 Sintering 92
  - III.3.3 Viscous Behavior 99
  - III.3.4 Elastic Constants and Fracture Strengths 105
- III.4 The Metal Interconnect Model 109
  - III.4.1 Thermal Expansion 109
  - III.4.2 Reduction 111
  - III.4.3 Sintering 117
  - III.4.4 Accuracy and Improvements to Sintering and Reduction Models 120

III.4.5 Evolution of Mass and Density 127
III.4.6 Viscoplastic Model 132
III.4.7 Elastic Constants 135

Chapter IV Conclusions and Future Work 138
IV.1 Summary of Developed Model 138
IV.2 Implementation of Model 141
IV.3 Validation and Extension of Model 142
IV.4 Conclusions and Applications for Model 148

Appendix 156

References 159

LIST OF TABLES

Table II.1: Measured porosities at different temperatures. 27

Table II.2: Unpublished MOR data on ~3mm diameter cylinders in the green state with different volume fractions of binder (Hurysz 2003). 68

Table III.1: Reported MOR at various temperatures for 8% YSZ with less then 3% porosity (Y. Du 2003). 108

LIST OF FIGURES

Figure I.1: The fuel cell schematic above shows how electrons and ions move through a solid oxide fuel cell to make a complete circuit. For simplicity, the metal interconnect is not shown (Tuller 2003). 3

Figure I.2: Co-extruded hybrid honeycomb fuel cell proposed by our group. 3

Figure I.3: SEM pictures were taken of the 53Fe39Ni8Cr system just after binder burnout at 350 ºC (left), during early sintering stages around 900 ºC (middle), and of the fully denseified structure (right). 7

Figure I.4: Typical examples of honeycomb structure. Green state hybrid 4x4 Yittria stabilized Zirconia and Inconell 617 honeycomb shown on left, and densified 8x8 copper honeycomb shown on right. 9

Figure I.5: Outline of manufacturing process for SOFC stacks. Initially the paste is prepared by mixing water, binder, lubricants, and powders in a high shear compounder. The resulting densified paste is then extruded to the desired shape. The extruded structure is then dried for a day to allow the binder to set and achieve a low level of structural strength. Finally, the green compact is fired in a reducing environment to reduce metal oxides and densify the structure. 11

Figure I.6: The extrusion process assembly for hybrid metal-ceramic structures. Two different paste mixtures are compounded into a total of 5 different cylinders. The cylinders are then loaded into the die in alternating metal, ceramic order. An extrusion press then pushes the cylinders through the die that forms the desired hybrid structure. 12

Figure I.7: Fully dense 47.5Fe 47.5 Ni5Cr specimen above exhibited substantial cracking due to hematite expansion during reduction, and mismatches in sintering and thermal expansion coefficients. The partially fired 47.5Fe 47.5 Ni5Cr specimen below shows how premature sintering can lead to specimen separation and failure. 14

Figure I.8: The hybrid structure above failed during cool down most likely because of a substantial difference in thermal expansion between the ceramic and metal. 16

Figure I.9: Thermal expansion of metal interconnect can be modified by changing powder composition (Church 2004). 16

Figure I.10: Despite the same stresses existing in the two joints, the one on the bottom failed, while the one of the top did not. This difference can be attributed, in part, to the difference in the quality of the green state joint. 18 17

Figure I.11: Ripples in green state extrusion are formed from differences in paste rheology and extruder pressure, and can lead to defects in the fired structure. 18

Figure I.12: Inhomogeneities (left) resulting from unmixed binder (center) produce voids on binder removal (J. L. Clark In Press). 18

Figure I.13: Three Fe47.5Ni5Cr hematite compacts fired under similar temperature profiles and in a gas flow rate of 400 sccm, 100 sccm, 20 sccm Ar + 4% H_2 from bottom to top respectively. The lower flow rates resulted in substantially fewer defects because the hematite reduction was pushed off to higher temperatures where the structures were more compliant. 20

Figure II.1: Fired honeycomb specimens were placed in an airtight container full of water, and then a vacuum was applied to fill the open pores with water. 27

Figure II.2: Experimental setup for sintering without hygrometer. 28

Figure II.3: Typical unconstrained shrinkage data that can be measured using the non-contact dilatometer. 32

Figure II.4: SEM pictures at a magnification of ~800 were taken of the Fe39Ni8Cr system in the green state at room temperature (top left), after binder burn out at 300 ºC (top right), after reduction had taken place at 680 ºC (bottom left), and during sintering at 915 ºC (bottom right). 33

Figure II.5: SEM pictures at a magnification of ~3250 were taken of the Fe39Ni8Cr system at 700 ºC (right), and at 750 ºC (left). The early stages of sintering appear to be starting by 750 ºC (left). 34

Figure II.6: Typical temperature profile that was used to separate the sintering behavior from the reduction behavior by holding the specimen at 700 ºC for 6 hours. 35

Figure II.7: A hygrometer was inserted into the exhaust line of the equipment used for the sintering studies to aid in the characterization of reduction. 37

Figure II.8: Hygrometer output from two different mass Fe39Ni8Cr honeycomb samples in 387 sccm Ar + 4% H_2. 38

Figure II.9: Each hygrometer peak was linked to the oxide that generated it by comparing how the peaks changed for different initial compositions of oxide powders. All runs were performed on honeycomb structures in 387 sccm Ar + 4% H_2. 38

Figure II.10: Hygrometer output from reducing samples of similar mass at different temperatures. The samples were honeycomb compacts of Fe39Ni8Cr in 387 sccm Ar + 4% H_2. 40

Figure II.11: Hygrometer output from two samples of different mass at the same temperature. The samples were honeycomb compacts of Fe39Ni8Cr in 387 sccm Ar + 4% H_2. 40

Figure II.12: Normalized isothermal rate of reduction of NiO from honeycomb Fe39Ni8Cr structure in 387 sccm Ar + 4% H_2. 44

Figure II.13: Interpolated parameters in Equation (II.4) for isothermal reduction rate. 44

Figure II.14: Nickel oxide reduction parameter η as a function of temperature and time, based on Equation (II.4). 45

Figure II.15: Comparison of arctangent curve fit surface to reduction surface derived from Equation (II.4). 45

Figure II.16: Uncalibrated hygrometer output from isothermal reductions of magnetite. Samples were loose Fe_3O_4 powder in 387 sccm Ar + 4% H_2. 47

Figure II.17: Deduced rate of reduction of magnetite at constant temperature from experimental observations. 48

Figure II.18: Control volume around reducing specimen in furnace. 50

Figure II.19: Calibrated hygrometer output from isothermal reductions of magnetite. Samples were loose Fe_3O_4 powder on ceramic platelet in 387 sccm Ar + 4% H_2. 52

Figure II.20: Calibrated relative humidity emissions from reducing magnetite specimen at its equilibrium partial pressure. The multi-experiment isothermal hold experiments were from loose Fe_3O_4 powder, while the ramp experiment was from an Fe39Ni8Cr honeycomb. All experiments were performed in 387 sccm Ar + 4% H_2. 53

Figure II.21: Rate of mass loss from reducing samples is constant until approximately 85% of initial oxide mass has left the structure, at which time it slow down. 54

Figure II.22: Comparison of experimentally observed and theoretical thermodynamic equilibrium partial pressure for the reduction of Fe_3O_4. 56

Figure II.23. Dimensions of dog-bone sample used for uniaxial tension tests. 58

Figure II.24: Uniaxial tension tests performed at room temperature at two different strain rates. The tests were performed on Fe39Ni8Cr dog-bone samples with an initial porosity of ~15.5% 59

Figure II.25: Machine drawings for high temperature grips used for high temperature tests. 60

Figure II.26: Layout of high temperature experiments. An MTS load frame (center) was used for the uniaxial tension pulls. The 2-piece ATS furnace was used to heat the gauge length of the specimen, and the ATS power supply (left) was used to power and regulate the furnace temperature. The computer (right) was used to record the measured displacement, time and load on the specimen. 61

Figure II.27: Close-up of two-piece ATS 1050 furnace and experimental setup. 62

Figure II.28: Stress strain curves from high temperature uniaxial tests. Samples were tested at a strain rate of 2×10^{-4} s^{-1} to failure, except for 670 °C (I), and 575 °C that were not tested to failure. The samples were Fe39Ni8Cr dog-bone samples with an initial porosity of ~15.5%. 63

Figure II.29: High temperature uniaxial tension tests performed at 10^{-4} s^{-1} (slow), and 10^{-2} s^{-1} (fast). Tests were performed on Fe39Ni8Cr dog-bone samples with an initial porosity of ~15.5%. 64

Figure II.30: High temperature relaxation tests performed at the terminal strain of the uniaxial tension experiments shown in Figure II.29. Fast and slow refer to the strain rate of the uniaxial tension experiment prior to the relaxation test, as defined in Figure II.29. Tests were performed on Fe39Ni8Cr dog-bone samples with an initial porosity of ~15.5%. 65

Figure II.31: Strain rate exponent at 0.3% and 2% engineering strain. 66

Figure II.32: Modified stress-strain curve obtained from the data in Figure 29 and a more appropriate modulus determined from ultrasonic techniques. 67

Figure II.33: Stress-strain diagram derived from compression experiments on Fe39Ni8Cr prior to sintering. Three types of samples were tested, the green compact, the compact after binder burnout, and the compact before sintering but after reduction. 69

Figure II.34: Cyclic compression tests on two different types of samples to determine level of elasticity of compacts at different stages. 70

Figure II.35: Measured temperature profile in heated stainless steel tube down the length of the tube starting from the center. The position of the TC within the cross-section was changed as well as the flow rate and age of the TC. 74

Figure II.36: Tabulated specifications for the Keyence model LS-7030 micrometer. Table taken from Chapter 9 of the instruction manual (Keyence 2001). 76

Figure II.37: Initially specimens were cut into 10mm wide square samples (left); however, interference from the trailing edges led to erroneous measurements, so the samples were ground into wedge shapes (right). 76

Figure II.38: Affects of water bubbler removing binder from electrolyte during firing. From left to right, YSZ without water bubbler, YSZ with water bubbler from 20 °C to 350 °C, ScSz with water bubbler from 20 °C to 700 °C, YSZ with water bubbler from 20 °C to 700 °C, YSZ with water bubbler from 20 °C to 700 °C. 78

Figure II.39: The isothermal sintering behavior of the electrolyte was adversely affected by incomplete binder burnout when no moisture was present during the firing process. 78

Figure II.40: Relative humidity in furnaces at room temperature after being opened up to room air with 387 sccm of Helium flushing through it. 80

Figure II.41: Background humidity level in empty furnace with 387 sccm Ar + 4% H_2 after 1 hour pre-flush. 81

Figure II.42: Rapid heating and cooling of furnace in an attempt to quantify amount of noise induced on transducers. Flow rate of 387 sccm Helium. 82

Figure II.43: Dilatometer and hygrometer output for two different NiO honeycomb structures undergoing reduction in 387 sccm Ar + 4%H_2. 80 83

Figure III.1: Phase diagram for Yittria Stabilized Zirconia (left) and Scandia Stabilized Zirconia (Right). 88

Figure III.2. Ternary diagram for Iron, Nickel, Chrome system at two different temperatures. 88

Figure III.3: Measured thermal expansion of YSZ is almost constant from room temperature to 1150 °C (Church 2004). 92

Figure III.4: Measured isothermal densification of ScSz compared to model prediction after performing a least squares fit on model parameters. Experiments performed on honeycomb samples in 387 sccm Ar + 4% H_2. 96

Figure III.5: Temperature dependence of β and τ parameters from experimental results. 97

Figure III.6: Comparison of predicted stress free densification and measured stress free densification using a 'realistic' temperature profile on honeycomb sample in 387 sccm Ar + 4%H_2. 98

Figure III.7: Comparison of predicted stress free densification and measured stress free densification using an unusually slow temperature profile, which exacerbates the error in measured low temperature parameters. Experiments performed on honeycomb sample in 387 sccm Ar + 4%H_2. 99

Figure III.8: Experimentally measured uniaxial viscosity versus, uniaxial viscosity predicted by the model. 103

Figure III.9: Figure from Cai (P. Z. Cai 1997), experimentally measured uniaxial viscosity of three different materials. 103

Figure III.10: Figure from Cai (P. Z. Cai 1997), showing relationship between temperature and density. 104

Figure III.11: Evolution of Young's modulus with porosity for 8% YSZ at room temperature, based on Atkinson and Selcuk model. 108

Figure III.12: Measured thermal expansion coefficient from RT to 1200 °C for the Fe39Ni8Cr system (Church 2004). 110

Figure III.13: Linear shrinkage of reducing honeycomb specimen at various temperatures, and the predicted shrinkage after fitting the model parameters to the data with a constant flow of 387 sccm Ar + 4% H_2. 114

Figure III.14: Temperature dependence of β_r and τ_r parameters from experimental results. 115

Figure III.15: Measured isothermal densification from sintering of Fe39Ni8Cr compared to model prediction after performing a least squares fit on model parameters. Experiments performed on honeycomb samples in 387 sccm Ar + 4% H_2. 119

Figure III.16: Temperature dependence of β_m and τ_m parameters from experimental results. 119

Figure III.17: Comparison of predicted and observed shrinkage of the Fe39Ni8Cr system when heated from 370 °C to 1270 °C at two different temperature ramp rates. The measurements were performed on a honeycomb Fe39Ni8Cr in 387 sccm Ar + 4% H_2. 121

Figure III.18: Extrapolated time dependence of β_r and τ_r parameters from experimental results. 125

Figure III.19: Comparison of modified model to experimentally measured shrinkages of the Fe39Ni8Cr system when heated from 370 °C to 1270 °C at two different temperature ramp rates. The measurements were performed on a honeycomb Fe39Ni8Cr in 387 sccm Ar + 4% H_2. 126

Figure III.20: Comparison of modified model to an observed shrinkage (independent of any parameter fitting) undergone by the Fe39Ni8Cr system when being heated from 370 °C to 1270 °C for a 'realistic' temperature history. The measurements were performed on a honeycomb Fe39Ni8Cr in 387 sccm Ar + 4% H_2. 127

Figure III.21: Evolution of Young's modulus with porosity for Fe39Ni8Cr at room temperature, based on Atkinson and Selcuk model. 137

Figure IV.1: Approximate evolution of fracture strength of 15% porous Fe39Ni8Cr and 15% porous YSZ during the manufacturing process. Fracture strengths not to scale. 141

Figure IV.2: Pictures of Fe39Ni8Cr and ScSz hybrid structure in green state (left) and after processing (right) in 0.75 °C/min ramp to 1250 °C with 4 hour hold at 1250 °C and 8 °C/min cool down in 387 sccm Argon + 4% H_2. Pictures to scale with each other. 144

Figure IV.3: Comparison of constrained sintering curve of Hybrid Fe39Ni8Cr, ScSz system with unconstrained sintering curves from ScSz and Fe39Ni8Cr. All runs were performed in 387 sccm Ar + 4% H_2. 145

Figure IV.4: Comparison of constrained sintering curve of Hybrid Fe39Ni8Cr, ScSz system with unconstrained sintering curves from ScSz. All runs were performed in 387 sccm Ar + 4% H_2. Specimen shown in Figure IV.2. 146

Figure IV.5: Constrained sintering curve of Hybrid Fe39Ni8Cr, ScSz system with isothermal hold during reduction, but prior to sintering. Artifact near 200 minutes assumed to be from specimen shape. All runs were performed in 387 sccm Ar + 4% H_2. 147

Figure IV.6: Estimated time required for ScSz system to relax 2% strain under 1 MPa hydrostatic driving stress at a constant temperature assuming only bulk viscous flow. 151

Figure IV.7: Estimated relaxation temperature of ScSz as a function of cool down temperature ramp rate and final relative density assuming a mean hydrostatic stress of 1 MPa is ‘relaxed’. 152

Figure IV.8: Modeled evolution of density in unconstrained reducing Fe39Ni8Cr sample being heated at 8 °C/min from 350 °C to 800 °C in 387 sccm Argon + 4% H_2. No substantial sintering had taken place, and the material was 88% reduced by 800 °C. 153

Figure IV.9: Modeled evolution of density in unconstrained reducing Fe39Ni8Cr sample being heated at 1 °C/min from 350 °C to 800 °C in 387 sccm Argon + 4% H_2. Slight sintering was occurring over 710 °C, and the material was 100% reduced by 542 °C. 154

SUMMARY

Recent developments in powder metal oxide processing have enabled co-extrusion of a honeycomb structure with alternating layers of metal and ceramic. Such a structure is envisioned for use as a Solid Oxide Fuel Cell (SOFC) if defects can be minimized during the manufacturing process. The two dissimilar materials tend to shrink at different rates during hydrogen reduction and sintering, inducing internal stresses that lead to structural defects such as cracks, or high residual stresses. The objective of this thesis is to characterize the shrinkage and relaxation mechanisms inherent in both the metal and ceramic so that internal stresses developed during manufacturing can be estimated and ultimately minimized.

Constitutive models are adapted from the literature to simulate the sintering and viscoelastic behaviors of the ceramic. Likewise, existing models in the literature are used to characterize the viscoplastic relaxation of the porous powder metal phase and its sintering behavior. Empirical models are developed for the reduction behavior of the metal oxides, based on a series of experiments conducted that measure water vapor (hygrometry) and dimensional change (dilatometry) during reduction and sintering. Similarly, the necessary parameters for the sintering model and viscoplastic model were determined through a series of experiments. The constructed system of constitutive equations appears to have the essential elements for modeling dimensional change, porosity/strength and development of internal (residual) stresses in co-extruded SOFC structures.

CHAPTER I

BACKGROUND

I.1 Introduction to Fuel Cells

Developing fuel cell technology is receiving considerable attention because of the wide array of possible applications for a multi-scaled independent power generation devices, with high efficiency and low emissions (Nguyen 1995; Huijsmans 1997; F.P.F. van Berkel 1999; 2002). The term "fuel cell" covers a wide range of different designs and materials, all of which are based around the direct electrochemical reduction of a fuel with an oxidant. Therefore, fuel cells range widely in operating temperature, power densities, and size. Furthermore, most fuel cells tend to be highly modularized, allowing them to be stacked in various configurations. Therefore, it is possible to design a fuel cell that has applications from small consumer electronics, to cars, to large-scale power generation devices used in power plants. Moreover, fuel cells are inherently different from conventional power generation techniques because they directly produce electricity through electrochemical combination of a fuel with an oxidant. The electrochemical reaction is a much more direct and efficient way to produce electricity then more conventional methods, which rely on combustion of fuel to generate heat and kinetic energy. Finally, by avoiding the combustion process, fuel cells generate only negligible quantities of environmentally unfriendly agents such as NO_x, SO_x. Furthermore, the electrochemical process used in fuel cells is a viable way to generate electricity from any gaseous fuel that can be electrochemically reduced and oxidized. This allows further

control over the emissions from the fuel cell as well as allowing the fuel cell to operate with a wide range of fuels.

Fuel cell technology has many advantages, but is still in its early stages and faces many technical problems. The scope of this thesis is to address some of the manufacturing problems associated within co-extruded solid oxide fuel cells (SOFCs).

SOFCs are comprised of 4 main components: the anode, the electrolyte, the cathode, and the interconnect. Generally some desired fuel such as hydrogen gas flows through the anode, where it undergoes an oxidation reaction and release electrons through the interconnect to the attached external circuit. Meanwhile, ionic atoms, such as oxygen diffuse through the electrolyte, which is impervious to electron flow, and meet up with an oxidant gas flow in the cathode. Finally, the electrons rejoin the ions after traveling through the external circuit, and undergo a reduction reaction with the oxidant gas. The above process is illustrated in Figure I.1 and I.2 below.

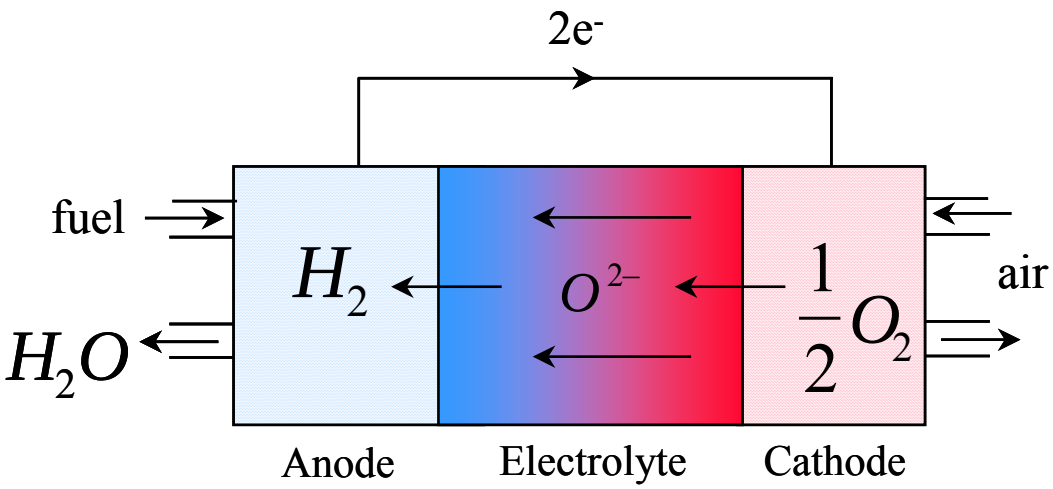

Figure I.1: The fuel cell schematic above shows how electrons and ions move through a solid oxide fuel cell to make a complete circuit. For simplicity, the metal interconnect is not shown (Tuller 2003).

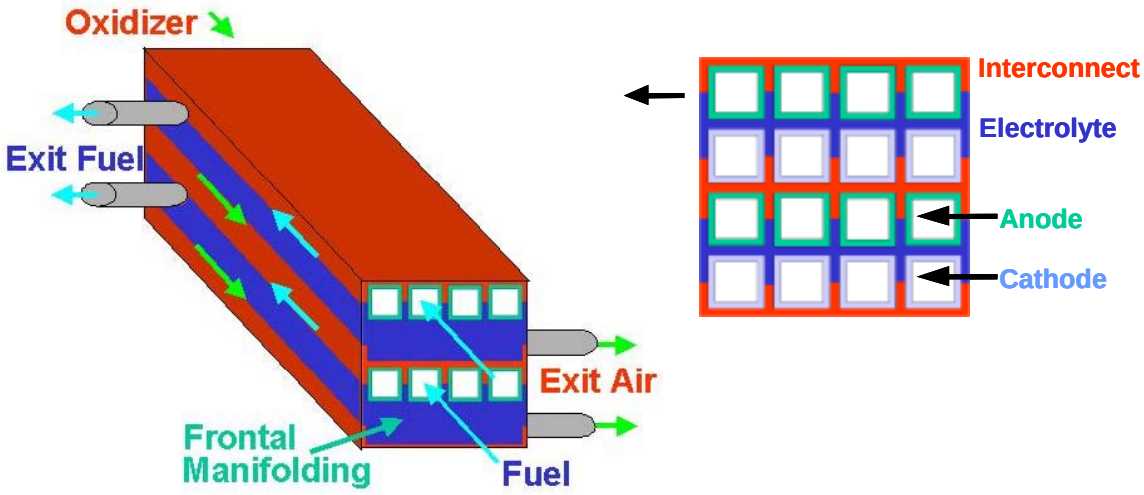

Figure I.2: Co-extruded hybrid honeycomb fuel cell proposed by our group.

The above outlined electrochemical process is only possible because of several unique material properties inherent in the materials chosen for different components in the fuel cell. Specifically, the ceramic electrolyte must be a good ionic conductor to

allow the oxygen ion to pass through it, but a poor electronic conductor to prevent the fuel cell from electrical shorting. Furthermore, the electrolyte must be physically thin enough to minimize the resistance to ionic conductivity, but dense enough to keep the fuel and oxidant separate. Moreover, the anode and cathode must allow fuel and oxidant to flow through it with an acceptable pressure drop, but still have a high concentration of surfaces for the reduction oxidation reaction to occur. The metal interconnect needs to be a good electrical conductor to minimize resistive losses, and oxidation resistant to hold up in the extremely oxidative environment at operating temperatures of 600 ºC and above. Finally, all components of the fuel cell must have similar coefficients of thermal expansion to prevent delamination during startup and shutdown of the fuel cell.

I.2 Inherent Problems with Solid Oxide Fuel Cells

Solid oxide fuel cells are an advanced technology and as such have many associated problems that need to be overcome before they can be considered a viable energy source (Nguyen 1995; 2002). The first and foremost problem keeping SOFCs off the market is their high cost per power output. SOFCs cost over an order of magnitude more then most of their competing energy sources. The elevated costs associated with SOFCs are due to a combination of complex fabrication processes and exotic material expenses. Because of the highly specialized needs of fuel cells, it is very difficult to find suitable cheaper material substitutes. However, it is possible to lower manufacturing costs and increase the dollar per kilowatt ratio.

Another one of the leading problems with SOFCs is that they require a high temperature hermetic seal between the ceramic electrolyte and metal interconnect to prevent leakage of fuel or oxidant to the surroundings. The presence of this metal ceramic joint is one of the leading reasons for fuel cell delamination and failure, as well as increased manufacturing costs. Specifically the fuel cell body tends to fracture at or near this joint because of the thermal expansion stresses that arise in it during startup and shut down. Often hermetically sealing the fuel cell is a separate step in the manufacturing process, and therefore adds substantial cost to the fuel cell. Therefore, one of the main objectives of the research grant that this thesis was funded under is to develop a low cost manufacturing process that results in a hermetically sealed fuel cell body composed of the electrolyte and metal interconnect.

Yet another major problem with SOFCs is that the metal interconnect tends to oxidize, degrading its electronic conductivity. Specifically, the metal interconnect is subjected to an extremely oxidative environment, and only the most dense inert metals do not oxidize. Therefore, both the material composition and porosity of the metal interconnect are extremely important to its long-term usability.

I.3 Powder Processing

Powder metallurgy (P/M) techniques have been around since the early 1900s and have the capacity to produce parts to net dimensions from a wide array of metal and ceramic powders. Powder metallurgy is comprised of four main steps: blending of powders, compaction of powders, forming of powders, and firing (Kalpakjian 2003). The

blending of powders is done for three reasons: to improve the packing ratio by mixing powders of different size distributions, to tailor the final composition of the materials, and to add enough lubricants and binder to hold the structure together through the forming processes. The compaction of powder blends is done to increase the density and strength of the compact so the firing process results in a higher quality product. Compaction of powders is usually done through hydraulic presses or high shear compounding presses. The powder material is called a green compact after it has been compounded. The forming of the powder is done so that the powders end up in the desired shape prior to firing. Powders can be formed in numerous ways, but our group uses an extrusion press to form the compact. Firing of the compacts is done to promote sintering and reduction and result in a body with mechanical properties equivalent to that of the solid powders used to form it.

I.4 Terminology

The "porosity" of a material is defined as

$$\varphi = 1 - \frac{\rho}{\rho_s}, \tag{I.1}$$

where ϕ is the porosity, ρ is the current density of the material, and ρ_s is the theoretical solid density of the material with no voids. The porosity of a material can be used as an indicator for the degree of sintering that has taken place.

"Sintering" will be defined as "The coalescence of powders at an elevated temperature via extensive solid-state diffusion" (Kalpakjian 2003). The sintering process is driven by a minimization of free energy. Specifically, reducing the total free surface area within the material by fusing the particles into a more dense homogenous structure minimizes the free energy in the powder system. The sintering process results in an isotropic volume shrinkage in the material for an initially random particle distribution. The sintering process is illustrated in Figure I.3 through a series of scanning electron microscope (SEM) images of an iron nickel powder material at different temperatures. The sintering process has an associated volume shrinkage with it.

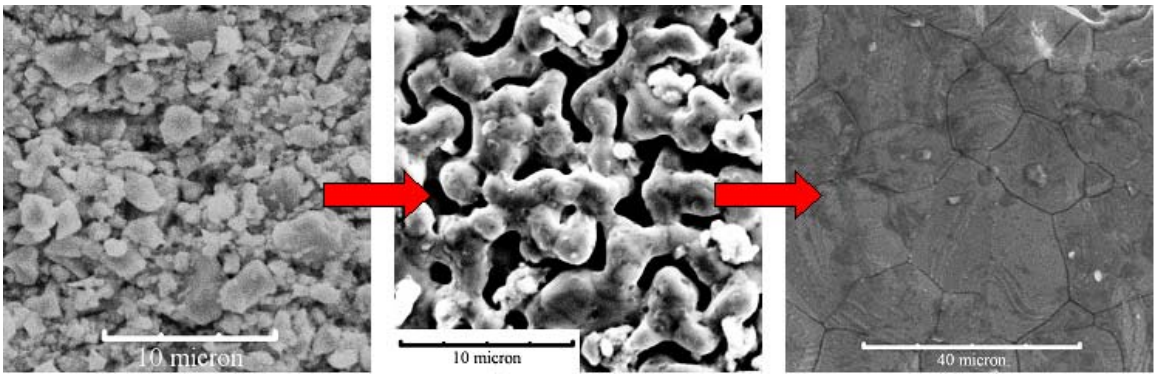

Figure I.3: SEM pictures were taken of the 53Fe39Ni8Cr system just after binder burnout at 350 ºC (left), during early sintering stages around 900 ºC (middle), and of the fully denseified structure (right).

The term "reduction" refers to a chemical reaction that removes oxygen from a material in a reducing environment such as Hydrogen. In contrast oxidation adds oxygen to a material. For example, rust formation is an oxidation process. Reduction is often associated with an isotropic volume shrinkage because the voids left from oxygen

diffusing out of the structure rearrange in a more compact form. The following reduction process is of particular interest:

$$17.6Fe_3O_4 + 39NiO + 8Cr + 109.6H_2 \rightarrow 53Fe39Ni8Cr + 109.6H_2O \ . \qquad (I.2)$$

The above reduction reaction shows nickel oxide, and Magnetite, a form of iron oxide, reacting with hydrogen to form a nickel iron chrome composition with water as a by-product.

A special notation is used to describe various powder compositions, where the weight percent of the composition appearing in the mixture is displayed in front of the element name. For example, a final metal composition that is 53% iron, 39% nickel, and 8% chrome by weight would be written as 53Fe39Ni8Cr.

"Binder" is the term used to refer to the polymeric substance that is mixed with the powders to form a rigid material upon drying. The binder is responsible for making the pre-fired extruded powder structure hold its shape. A wide variety of binders exist; however, all the compacts used here contained approximately 5 weight percent of methycellulose. During the firing process around 250 ºC to 350 ºC, the binder sublimes, resulting in a porous structure in a process generically called 'binder burnout.'

A green compact, which is often just referred to as a "compact," is the material that makes up the mixture of powders, lubricants and binder after compounding has occurred. Green compacts are typically 30-70% of the final density of the material after firing. Green compacts are inherently very weak, because they are held together entirely

by the binder and geometrical interlocking of powder particulates. Specifically, green compacts have no direct bonding between powder particles.

The term "honeycomb" is generically used to describe the geometry of specimens after extrusion, before or after firing. Specifically, honeycomb usually refers to the linear array of square channels in the specimen as shown in Figure I.4. The other prevalent geometry used during these studies was extruded flat strip specimens.

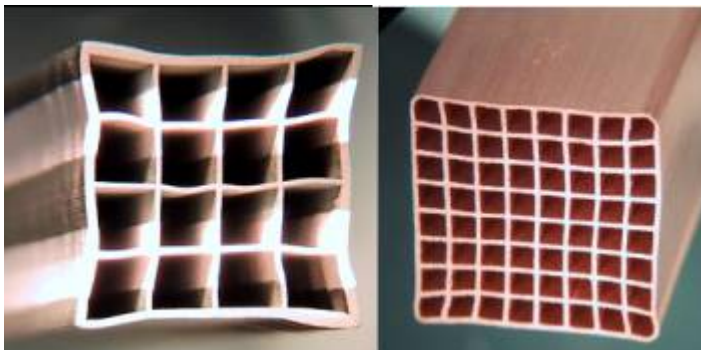

Figure I.4: Typical examples of honeycomb structure. Green state hybrid 4x4 Yittria stabilized Zirconia and Inconell 617 honeycomb shown on left, and densified 8x8 copper honeycomb shown on right.

I.5 Overview of the Powder Process: Advantages and Disadvantages

The current powder process that is used by our group (Clark 1999; Church 2002) to manufacture SOFC stacks is shown in Figure I.5 below. Two different powder systems are mixed and compounded during the manufacturing process, a Zirconia based ceramic powder, and an iron oxide nickel oxide based metallic powder. The powders are compounded in a Buss Kneader high shear compounder. The compacts are then layered in the extruder, and co-extruded through a honeycomb die shown in Figure I.6. The

extruded compacts are then allowed to dry so the binder sets, and a degree of mechanical strength is achieved. The extruded compacts are then fired in a reducing environment to reach final density and become hermetically sealed. In summary, the fabrication of the SOFC body is a powder processing approach where the electrolyte and metal interconnect are co-extruded in the green state, and then fired at high temperatures to achieve reduction of the metal interconnect, sintering to full densification and a hermetic joint.

On a side note, metal oxide powders are used in place of metal powders when the metal powders cannot be used, or when certain reduction behaviors are desired. Specifically, some metal powders, such as iron, tend to be unstable because of the oxidative nature of the metal and the powder's high surface area to volume ratio. Consequently, either magnetite (Fe_3O_4) or hematite (Fe_2O_3) is substituted to form a stable powder compact. Furthermore, the substitution of a metal oxide powder for a metal powder can promote positive manufacturing behaviors. For example, substitution of nickel oxide for nickel will result in a greater volume change during firing, which can be beneficial in attempting to match the total volume change of the sintered electrolyte. Finally, extruded wall thicknesses can be reduced using metal oxide powders, because oxide powders are finer then metal powders.

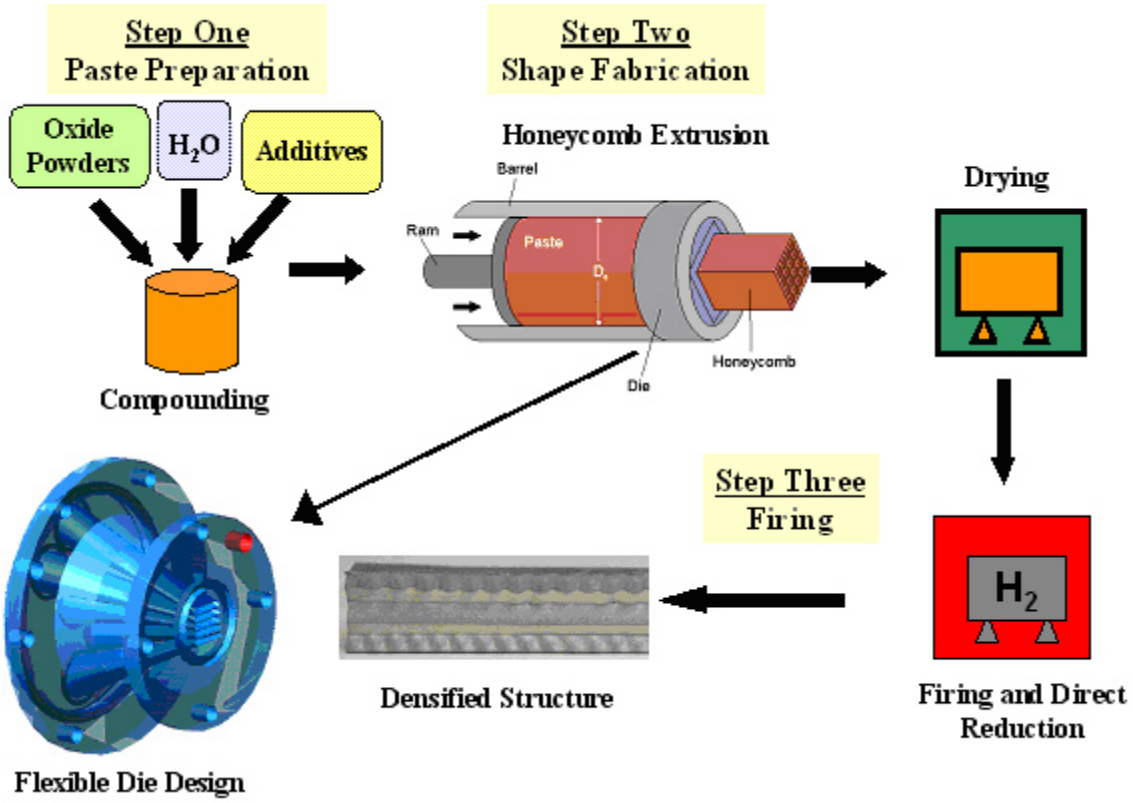

Figure I.5: Outline of manufacturing process for SOFC stacks. Initially the paste is prepared by mixing water, binder, lubricants, and powders in a high shear compounder. The resulting densified paste is then extruded to the desired shape. The extruded structure is then dried for a day to allow the binder to set and achieve a low level of structural strength. Finally, the green compact is fired in a reducing environment to reduce metal oxides and densify the structure.

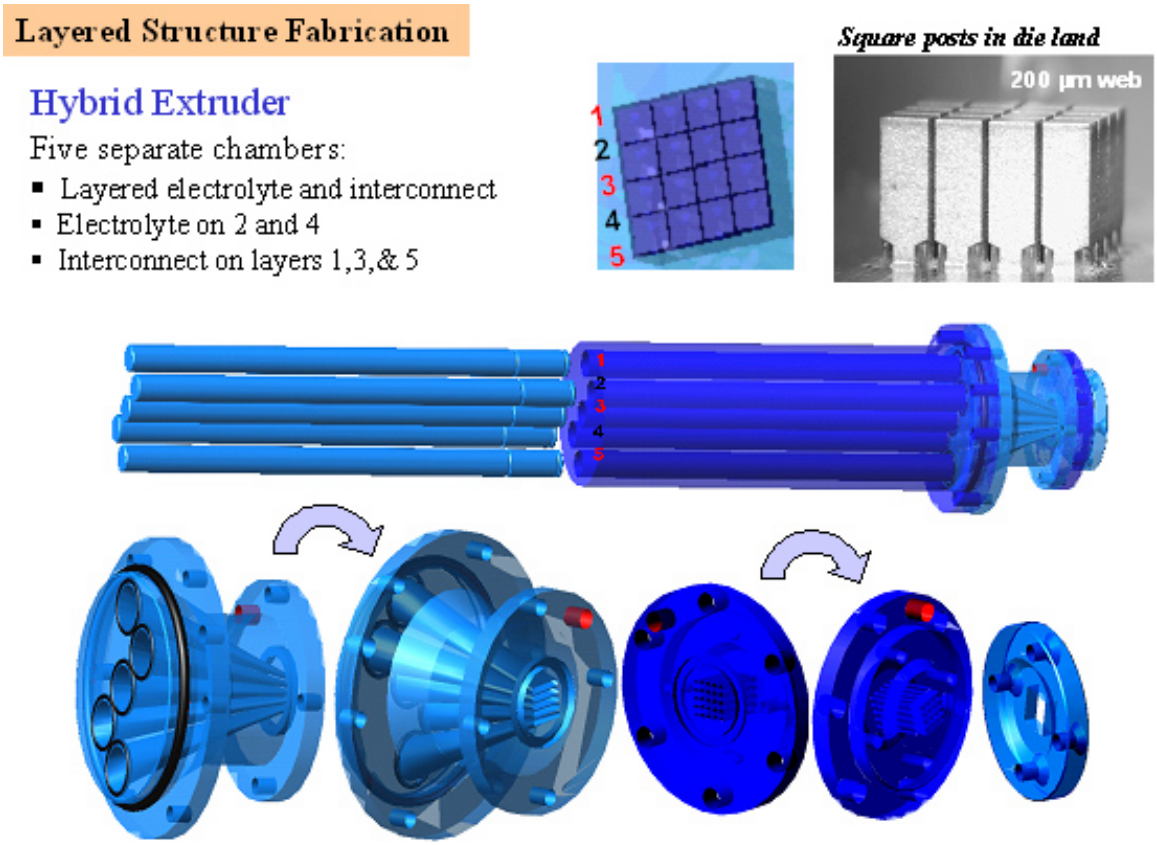

Figure I.6: The extrusion process assembly for hybrid metal-ceramic structures. Two different paste mixtures are compounded into a total of 5 different cylinders. The cylinders are then loaded into the die in alternating metal, ceramic order. An extrusion press then pushes the cylinders through the die that forms the desired hybrid structure.

The powder process approach has several advantages. First of all, processing allows alteration of the initial composition of powders in the green state. For example, if a more oxidation-resistant metal interconnect is desired, then a higher percentage of chromium can be added to the powder compact in the green state. Additionally, the extrusion process allows for a wide range of different two-dimensional cross-sectional geometries to be extruded. This allows for a more optimal fuel cell design to be manufactured at no extra cost. Finally, the co-extrusion process allows the electrolyte and metal interconnect to be joined at a hermetic joint during the extrusion process. The

formation of a hermetic joint in a single process should substantially reduce manufacturing costs.

Powder metal processing offers many manufacturing advantages, but it also has drawbacks. For starters, the powder process has not eliminated the need for the hermetically sealed joint between the electrolyte and metal interconnect. The powder process makes it less expensive to form the joint and can minimize thermal expansion coefficients by tailoring material properties. However, fundamentally all the problems that plague metal-ceramic joints (R. O. Ritchie 1993; B. J. Dalgleish 1994; J. M. McNaney 1994) still exist with the powder processing. Furthermore, the powder process gives rise to a new set of problems related to converting a green compact to a densified structure. First of all, green compact system is made up of two distinctly different powders that sinter differently at a given temperature. The metal and ceramic powders undergo large volumetric shrinkages during the firing process, but they shrink different amounts as a function of temperature. Because the shrinkage of the ceramic and metal are constrained by each other at the common joint, stresses build up in the compact during the firing process. These stresses can result in cracks and other defects as shown in Figure I.7 before the specimen ever reaches full density.

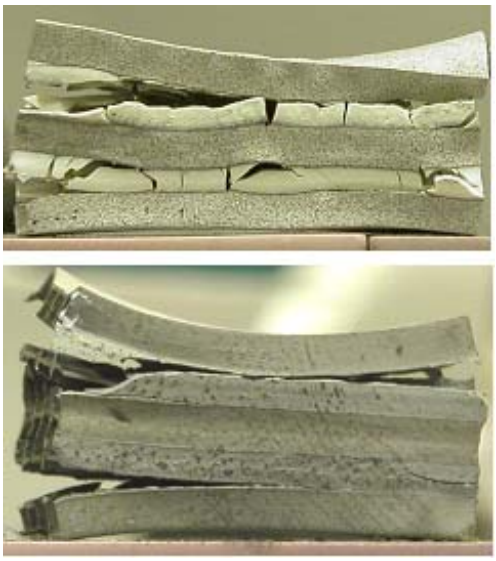

Figure I.7: Fully dense 47.5Fe 47.5 Ni5Cr specimen above exhibited substantial cracking due to hematite expansion during reduction, and mismatches in sintering and thermal expansion coefficients. The partially fired 47.5Fe 47.5 Ni5Cr specimen below shows how premature sintering can lead to specimen separation and failure.

The SOFC fabrication process is further complicated by shrinkage and cracking that occurs during the reduction of the metal oxide powers. Specifically, as the oxide powders start to reduce the resulting oxygen gas must leave the structure, leaving a porous, partially bonded substrate. The structure then begins to shrink as oxygen vacancies are consolidated. However, the metal is constrained from shrinking by the ceramic. Hence, the reduction process can also result in specimen fracture during manufacturing.

I.6 Motivation for Modeling

The primary problem with converting a green hybrid extrusion to a fully densified structure is to maintain a fracture-free, hermetically sealed joint between the ceramic and metal phases. Simply put, the success or failure of the hermetic joint during the manufacturing process depends primarily on three things: the final material properties, the quality of the green state extrusion, and the shrinkages or morphological changes during the manufacturing process. Therefore, improvement in any one of these areas will result in more defect free fuel cells being manufactured.

The final material properties have a substantial affect on the successful manufacturing of a fuel cell. For example, if the thermal expansion coefficients of the solid metal interconnect and electrolyte are not closely matched, then structure will fracture during firing as shown in Figure I.8. Likewise, if the metal interconnect has low ductility, then even a slight thermal expansion mismatch may result in a fractured electrolyte. The properties of the metal interconnect can be altered substantially by varying the composition of metals in the metal compact. This is represented in Figure I.9, which shows the thermal expansion characteristics of various manufactured metal compacts. Simple models can be formulated to predict the end state material behavior of a given powder composition, but their discussion is beyond the scope of this thesis.

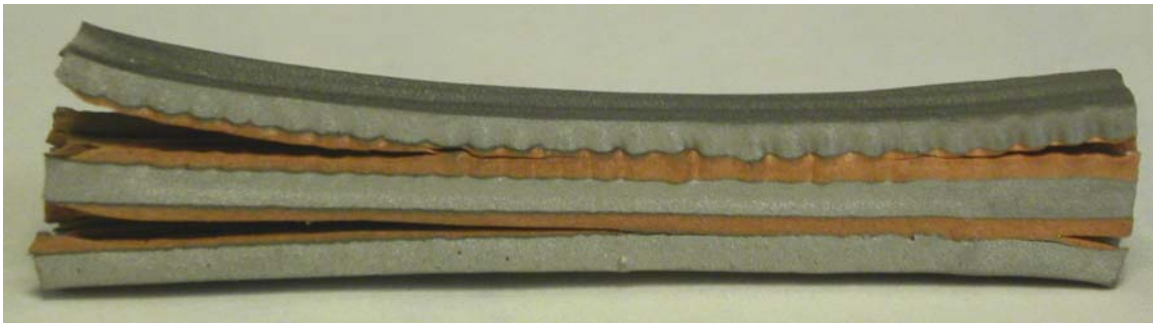

Figure I.8: The hybrid structure above failed during cool down most likely because of a substantial difference in thermal expansion between the ceramic and metal.

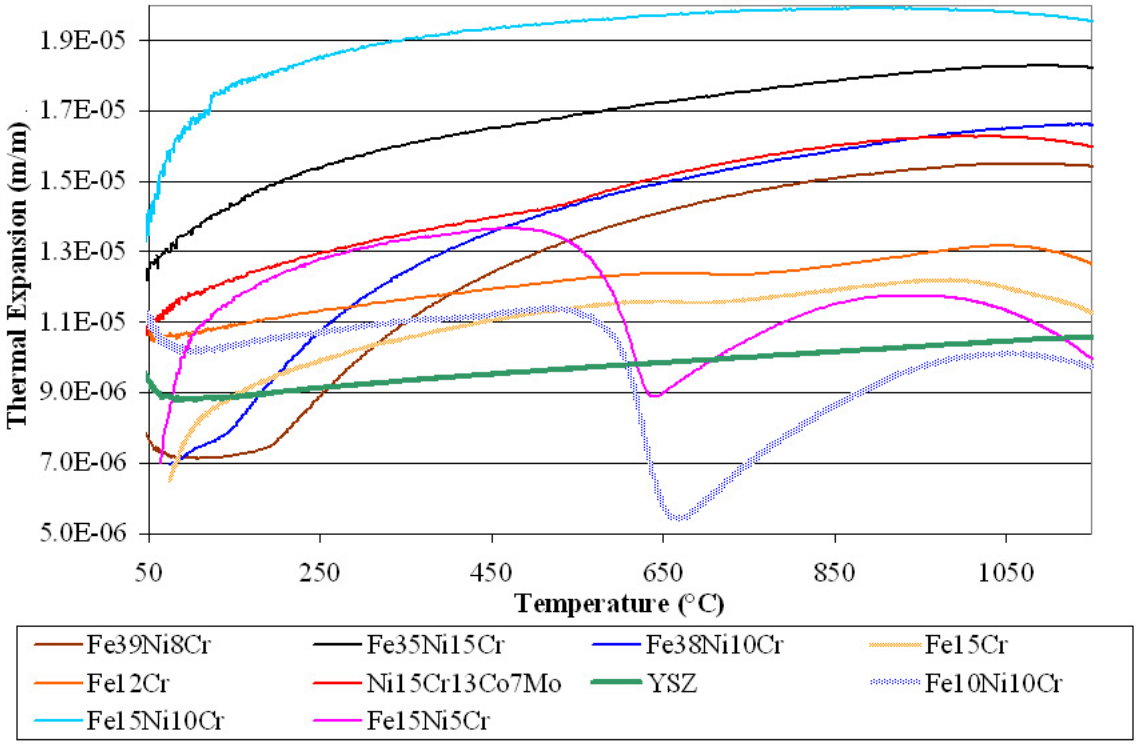

Figure I.9: Thermal expansion of metal interconnect can be modified by changing powder composition (Church 2004).

The quality of the green state extrusion also plays a substantial role in the successful manufacturing of a fuel cell body. Defects such as missing cell walls during the extrusion process obviously result in deficient fuel cell stacks. Likewise the quality

of the interface between the electrolyte and metal interconnect after the extrusion process is very important. Specifically, as shown in Figure I.10, some joints are more intimately formed in the green state, resulting in joints that are less prone to de-lamination during firing. Likewise, ripples in the green extrusion as shown in Figure I.11 can affect the degree of bonding after reduction and sintering. Finally, the quality of the powder compact itself is important. Specifically, poor compounding and mixing of the powders can result in large voids in the fired material which deteriorate the overall mechanical and electrical behavior of the fuel cell stacks. Figure I.12 shows the propagation of a compounding defect through the manufacturing process. Characterization and improvement upon the current extrusion methods and paste rheology can be found in the literature (Clark 1999; Church 2002; J. L. Clark In Press), and are beyond the scope of this thesis.

Figure I.10: Despite the same stresses existing in the two joints, the one on the bottom failed, while the one of the top did not. This difference can be attributed, in part, to the difference in the quality of the green state joint.

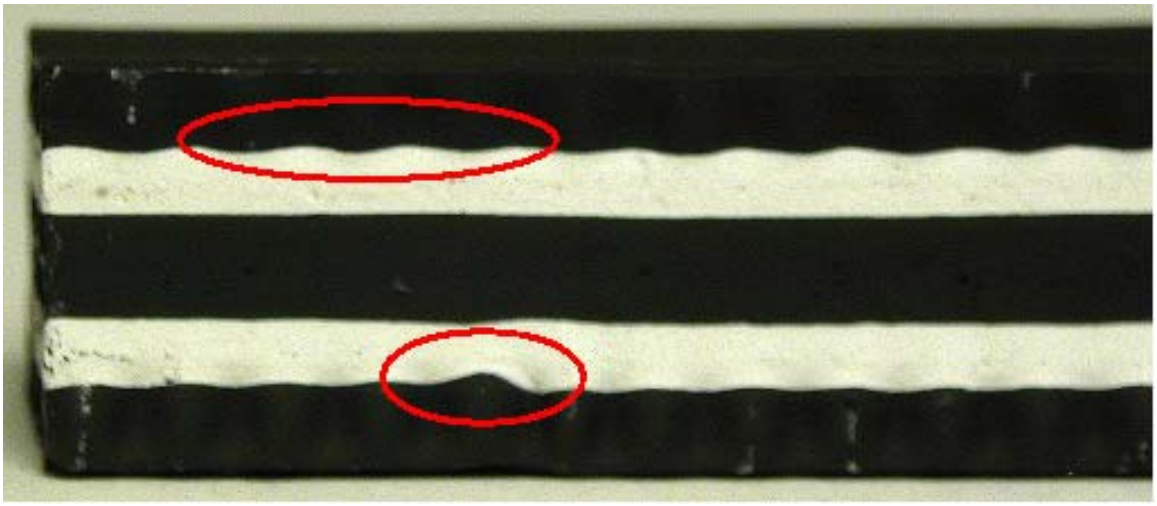

Figure I.11: Ripples in green state extrusion are formed from differences in paste rheology and extruder pressure, and can lead to defects in the fired structure.

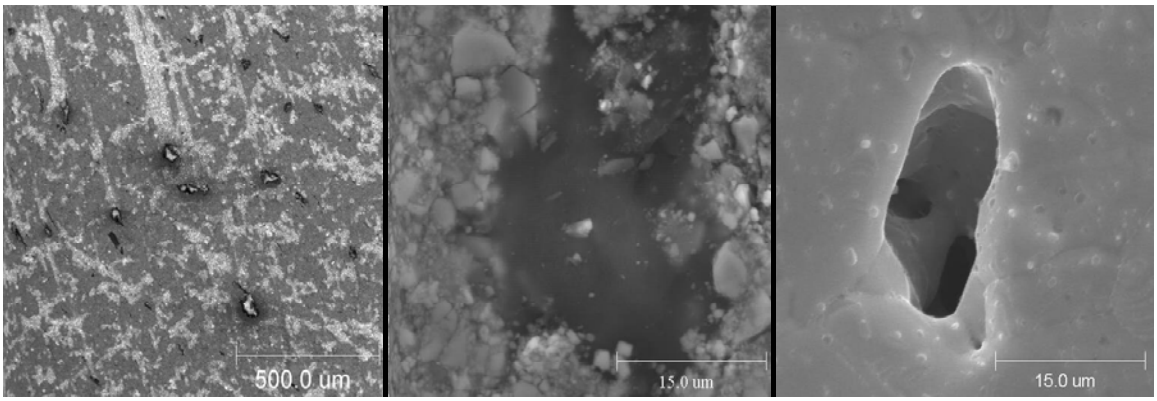

Figure I.12: Inhomogeneities (left) resulting from unmixed binder (center) produce voids on binder removal (J. L. Clark In Press).

The manufacturing conditions also play a substantial role in the fabrication of defect free fuel cell stacks. Although the total unconstrained shrinkage mismatch (from sintering and reduction) between any two compacts is independent of the manufacturing process, the stresses that develop within the system from these mismatches can be minimized. Specifically, much freedom exists in choosing the processing schedule, such

as temperature ramp rate, peak temperature, gas flow rates and concentrations, all of which can affect the internal stress evolution of the SOFC stack. The modification of any one of these parameters can have a dramatic effect on the build-up and relaxation of stresses during the manufacturing process. For example, lower hydrogen flow rates and more rapid temperature ramp rates tend to defer reduction and its associated shrinkage until higher temperatures, at which the specimen is more compliant. Similarly, slow cool-down ramp rates after firing allow the structure to relieve more of its internal stresses, while fast cool-downs usually results in high internal stresses and fracture. Figure I.13 shows a series of identical green compacts that were subjected to different processing environments. Specifically, a very similar temperature profile was used, however, the gas flow rate was varied from 400 sccm to 20 sccm in an attempt to force the reduction reaction into occurring at higher temperatures, where the structure would be more compliant. As shown in Figure I.13, the slower flow rates did result in a structure with substantially fewer and more minor defects; however the given composition could never be made defect free because the shrinkage associated with the two compact compositions in the hybrid structure were very poorly matched. Nonetheless, an effective processing schedule can be very important in minimizing defects in the final structure. Unfortunately, determining an optimal set of processing conditions to minimize structural defects by a trial and error procedure is extremely difficult because of the large number of degrees of freedom in the manufacturing process. Therefore, a model that could predict defect formation from a given set of process conditions would be a useful tool in developing defect free fuel cell stacks. However, such a model would require an intimate

knowledge of the behavior of the specific material composition under a wide array of process conditions.

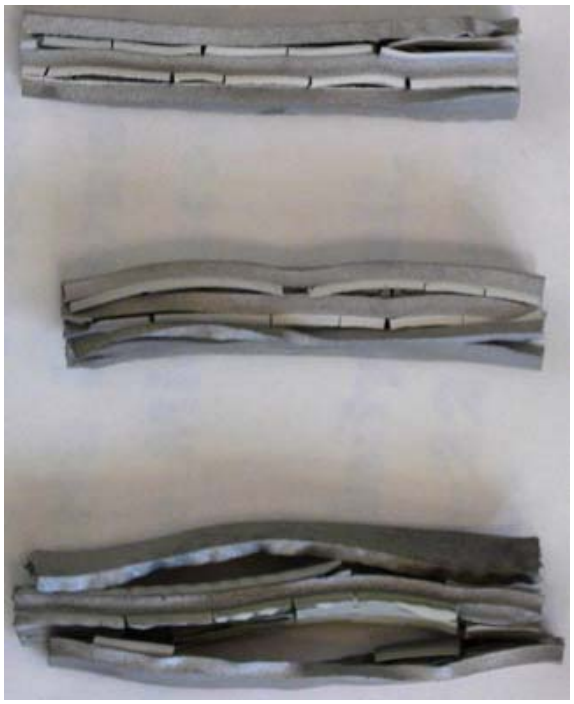

Figure I.13: Three Fe47.5Ni5Cr hematite compacts fired under similar temperature profiles and in a gas flow rate of 400 sccm, 100 sccm, 20 sccm Ar + 4% H_2 from bottom to top respectively. The lower flow rates resulted in substantially fewer defects because the hematite reduction was pushed off to higher temperatures where the structures were more compliant.

Most methods that involve the improvement of green compact quality require substantial equipment costs, which are not a viable alternative. Therefore, the modeling effort that is developed in this thesis only addresses processing and material property issues. Specifically, the goal of this project is to develop a model that is capable of supporting assessment of near optimal processing environments and an acceptable range of solid material properties. As mentioned before, the construction of such a model

would give substantial insight into the sintering, reducing, thermal expansion, and relaxation behaviors of the different materials. Ideally, the model would give key insight into the manufacturing process, and result in changes that allowed for more defect free structures to be manufactured.

I.7 Existing Models

Several groups, namely Hsueh et al., Bordia, Scherer, Cai et al., and N.J. Shaw (Scherer 1977; C. H. Hsueh 1986; R. K. Bordia 1988b; Shaw 1989; L. Chandra 1997; P. Z. Cai 1997a; Johnson 2003) have attempted to model or measure the internal stresses that develop during the firing and cool-down of powder compacts. The objective of most of these groups is to estimate the stresses that arise in powder compacts as they sinter in a constrained manner. The models are usually made up of two parts, stress-builders and stress-relievers. The stress builders are usually attributed to the thermal expansion and sintering of a constrained powder compact. The primary stress-reliever is usually assumed to be a viscous or visco-elastic relaxation mechanism that takes place in the powder compact at elevated temperatures. The ultimate viability of the model is dependent on how well the stress-builder and stress relaxation mechanisms are simulated.

Several different approaches have been used to determine the sintering behavior of powder compacts. Scherer (Scherer 1977) developed a micro-mechanical model for free sintering based on the assumption of an initial particle size and behavior. Hseuh et al. (C. H. Hsueh 1986) developed a similar model based on micro-mechanics, but augmented the model by incorporating an empirical grain growth model for improved

accuracy. Cai et al. (P. Z. Cai 1997a) used experimental results to determine the shrinkage associated with sintering, in lieu of an analytic model. All the above groups used Scherer and Bordia's (R. K. Bordia 1988a) model to convert a free sintering behavior into a constrained sintering behavior. Generally, most of the sintering models project similar shrinkage behavior.

The vast majority of models in the literature focus on using a viscous or visco-elastic analogy to model the high temperature relaxation behavior of the powder compacts. Bordia and Scherer (R. K. Bordia 1988b) showed that these types of models are representative of sintering ceramic compacts. However, one of the major sources of error associated with these types of models is in the determination of mechanical properties of the sintering compact. Initially, many of the early modeling approaches assumed constant mechanical properties, such as viscosity and modulus. However, later experiments showed this to be a very poor assumption. Later models allowed for property variation, however, there was a substantial difference in opinion on how the properties actually varied. Several groups, such as Bordia and Raj (R. Raj 1984), attempted to directly measure how some of the mechanical properties varied with time and temperature. However, even the experimental were inconclusive. To date, one of the most difficult parts of modeling the firing of powder compacts is in the determination of how the mechanical properties, especially the viscosity, varies with time, temperature, and porosity.

I.8 Problems with Existing Models: Motivation

Before any of the above models can be implemented, three major factors need to be addressed. First, most of the analytical sintering models require several parameters that are material and process-specific, and must therefore be determined experimentally for the specific compact of interest. Specifically, the sintering behavior of a compact is strongly dependent on its initial properties such as packing ratio and average particle size, as well as powder composition (Lu 1996). These parameters have not been published for our material and process, and therefore must be experimentally determined. For the purposes of this study, 12% Scandia 1.5% Ceria Stabilized Zironia (ScSz) was the used for the electrolyte, and Fe39Ni8Cr was used for the metal interconnect. Secondly, the visco-elastic models were only found to be valid for ceramic-based compacts, and not metallic compositions. Therefore, an alternative model needs to be used for the metal that is capable of predicting the flow behavior at high temperatures and porosity levels. Several suitable viscoplastic models exist (Perzyna 1966; K.S. Chan 1984; M. Ortiz 1986; Li 1992; E. B. Marin 1996; E. B. Marin 1998). Lastly, none of the current models to date take reduction into consideration although experiments have been performed on the reduction behavior of NiO and Fe_3O_4 (Haase 1976; Hayes 1990; Chakraborty 1999). Specifically, all the sintering models in the literature assume the compact remains in oxide form throughout the firing process. Therefore, none of the current models take the density changes or other property changes associated with reduction into account. Obviously that diminishes the applicability of the current models to the current situation. Therefore, the objective of this thesis is to formulate an all-encompassing model that accurately represents the sintering, reducing, and relaxation behavior of the electrolyte

and metal interconnect. To our knowledge, such an ambitious undertaking is unique in the literature.

CHAPTER II

EXPERIMENTAL METHODOLOGY

II.1 Porosity Experiments

The porosity of extruded honeycomb compacts were measured after being fired in a variety of different temperature profiles using the Archimedes method i.e.,

$$\begin{aligned} \varphi_{total} &= \varphi_{open} + \varphi_{closed} \\ \varphi_{open} &= \frac{m_{sat} - m_{dry}}{m_{sat} - m_{sus}} \\ \varphi_{closed} &= 1 - \frac{m_{dry}}{\rho_s \left(m_{dry} - m_{sus} \right)} \end{aligned} \quad , \qquad \text{(II.1)}$$

where φ_{total} is the total measured porosity, φ_{open} is the porosity of the specimen that is open to the surface, φ_{closed} is the trapped (closed) porosity, ρ_s is the theoretical solid density of the material, m_{dry} is the mass of the dry specimen, m_{sat} is the mass of the specimen with the open porosity filled with water, and m_{sus} is the mass of the saturated specimen when suspended under water (Church 2002). The dry mass was determined by weighing the dry, non-saturated sample on a Denver Instruments TR-203 electric balance. The saturated mass was determined by submersing the specimen in water that was under a vacuum for 20 to 60 minutes, then patting it dry with a damp cloth and weighing it. The vacuum and manual agitation of the container sped up the rate that the water diffused into the open pores of the structure. Figure II.1 shows how the specimen

was placed under vacuum. The saturated and suspended mass was determined by weighing the saturated sample while it was submerged in water. The theoretical density of the material was determined by a weighted average of the solid density of the powders based on the final mass percent of each composition in the specimen. Table II.1 shows the measured porosity of the ScSz and Fe39Ni8Cr systems that sintered at different temperatures. The porosity measurements for Fe39Ni8Cr and ScSz were measured on extruded Fe39Ni8Cr and ScSz honeycomb samples respectively that were ground into wedges prior to firing, and weight approximately 0.5 grams in the green state. Ideally, the porosity of the materials in the fuel cell stacks should be as low as possible, but 5% to 6% total porosity was considered an achievable level of porosity. The excessive porosity in the measured samples can be attributed to incomplete reduction of chromium in the Fe39Ni8Cr system, and inadequate formation and powder packing of the ScSz paste. Uncertainty in the mass measurements of the specimen led to an uncertainty of approximately +/- 2% of the total porosity of the specimen being measured.

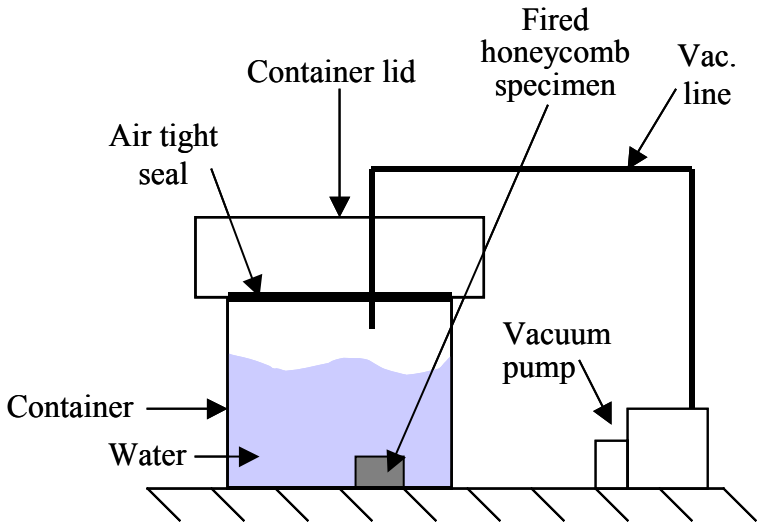

Figure II.1: Fired honeycomb specimens were placed in an airtight container full of water, and then a vacuum was applied to fill the open pores with water.

Table II.1: Measured porosities at different temperatures.

Material	**Temperature (°C)**	**Hold Time (Hours)**	**Open Porosity (%)**	**Closed Porosity (%)**	**Total Porosity (%)**
Fe39Ni8Cr	1050	10	31.8	8.9	40.7
Fe39Ni8Cr	1100	10.5	27.5	7	34.6
Fe39Ni8Cr	1150	10	20.6	9.2	29.8
Fe39Ni8Cr	1250	10	1.8	16.5	18.3
ScSz	1050	7	51.7	6.1	57.8
ScSz	1100	7	40.7	11.5	52.2
ScSz	1150	8	26.5	11.3	37.8
ScSz	1250	10	5.0	15.2	20.2

II.2 Sintering Measurements

The sintering behavior of powder materials results in large dimensional changes that can be measured during the sintering process. Figure II.2 shows the experimental setup that was used to measure the shrinkage behavior during sintering.

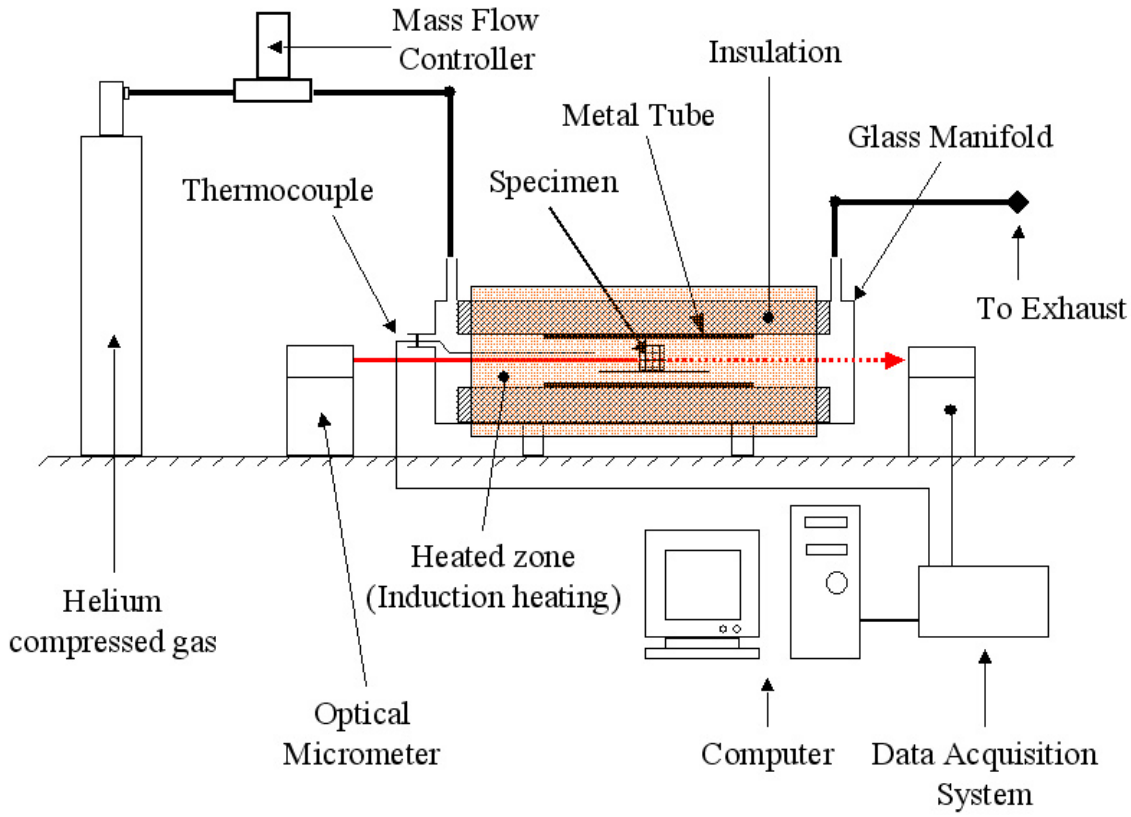

Figure II.2: Experimental setup for sintering without hygrometer.

The experimental setup consisted of a Keyence LS-7030MT high speed, high precision digital micrometer, which is also referred to as the non-contact dilatometer, a custom-built furnace, and a National Instrument 4351 and TBX 68T running Virtual Bench logger 2.5 data acquisition system. The furnace was designed and built with the

constraint imposed by the dilatometer that required a direct line of sight through the furnace. The furnace consisted of an inductively heated stainless steel tube wrapped in high temperature insulation and fit inside of a custom-built glass manifold. The glass manifold was air tight at atmospheric pressure, and allowed the environment around the sample to be controlled. A mass flow controller controlled the flow rate of a dry compressed gas, usually helium or a nonflammable mixture of Argon and Hydrogen, which was flowed through the glass manifold (it was observed that the sintering shrinkage was independent of the carrier gas used, although this is not true for reduction). A Honeywell DCP 200 temperature controller controlled the temperature of the sample in the pipe using a thermocouple input near the sample, and an output to the induction heater. The non-contact dilatometer was aligned such that it could send a light beam down the axis of the stainless steel tube, and then receive the transmitted light on the far side of the tube. If an object such as the sample was placed in the middle of the tube so that it partially blocked the emitted light beam, the receiving part of the dilatometer could measure the shadow cast upon it, and output a dimension that corresponded to the length of the sample. The data acquisition system was then used to record the dimensional measurement from the dilatometer, the temperature history of the thermocouple near the sample, and the elapsed time of the experiment. For safety reasons, an over-temperature protection circuit was added to the instrument shown in Figure II.2 that consisted of an Omega temperature controller, which turned off the induction heater when the control TC indicated temperatures over a preset value. Furthermore, the exhaust was plumbed through a double bubbler of silicon and exited into an 800 °C furnace to prevent back streaming and consume volatile gases.

A less accurate non-contact micrometer was used to characterize the shrinkage behavior of the specimens during the experiments instead of a stick type dilatometer because of concerns that a stick type dilatometer might fracture the specimen. Specifically, it was believed the force imparted on the thin walled specimens by a stick type dilatometer could distort or fracture the specimen during and after binder burnout (see section II.4 for fracture strength after binder burnout). Therefore, a digital micrometer was used for dimensional measurements; however, the recorded dimension from the dilatometer is less accurate than desired, because the light beam bends slightly in transmission through the glass manifold and heated gases. However, the optical micrometer is extremely precise. Therefore, the ratio of current length to initial length, or percent shrinkage of the specimen, is accurate to less then a tenth of a percent, which was deemed acceptable enough to support the choice of the optical micrometer.

The sintering behavior of the electrolyte is easier to characterize then the sintering behavior of the Fe39Ni8Cr system, because sintering is the sole mechanism that results in a dimensional shrinkage from the electrolyte. The Fe39Ni8Cr system, on the other hand, has a shrinkage associated with reduction that must be separated out of the sintering measurements to accurately characterize the sintering behavior. Figure II.3 shows a representative unconstrained shrinkage curve for ScSz and the Fe39Ni8Cr system for a typical manufacturing temperature profile. It is important to realize that the difference in total shrinkage of ScSz and Fe39Ni8Cr, and the difference in rate of shrinkage as a function of temperature all lead to stress build-up in a constrained system. The slight expansion of ScSz in the first 60 minutes can be attributed to thermal expansion. The shrinkage that occurs after 60 minutes can be entirely attributed to sintering for the ScSz.

Assuming the mass is constant during the experiment, which is a valid assumption for the electrolyte, the relative density of the structure can be estimated from the current shrinkage, i.e.,

$$\frac{\rho}{\rho_f} = \frac{\rho_o}{\rho_f}\left(\frac{L_o}{L}\right)^3 \quad , \tag{II.2}$$

where ρ is the current specimen density, ρ_f is the final (theoretical) density, ρ_o is the initial green state density, L_o is the initial length of the shadow measured by the dilatometer and L is the current length of the shadow measured by the dilatometer. The measured porosity was within +/- 3% of the porosity calculated from shrinkage, on average.

The shrinkage measured for the Fe39Ni8Cr system, on the other hand, is due to a combination of reduction and sintering. The dilatometer only measures the total shrinkage, and cannot differentiate the shrinkage that occurs from sintering versus reduction. Therefore, additional information was needed to determine when the onset of sintering first occurred.

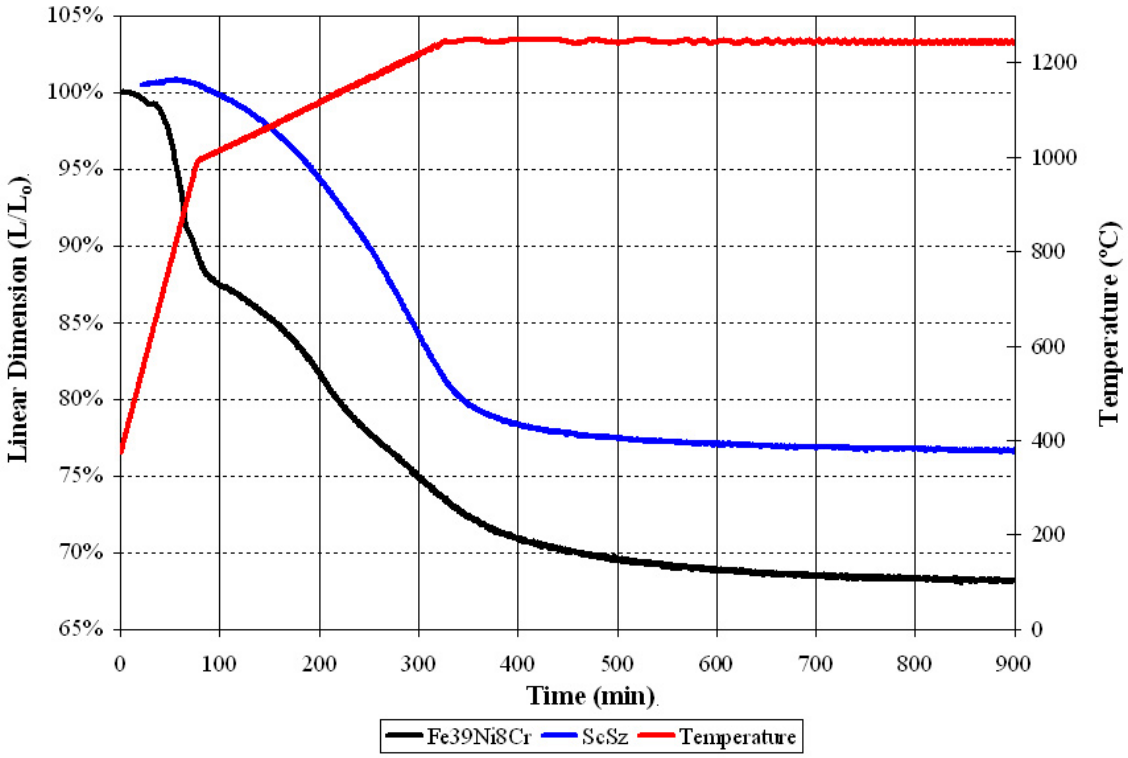

Figure II.3: Typical unconstrained shrinkage data that can be measured using the non-contact dilatometer.

Scanning electron microscope, or SEM, pictures were taken of the Fe39Ni8Cr system after they had been held isothermally at different temperatures for 2 hours. Figures II.4 and II.5 indicate the onset of sintering to be between 700 ºC and 750 ºC. Therefore it can be assumed that any shrinkage measured by the dilatometer below 700 ºC is not associated with sintering. However, the shrinkage above 700 ºC can still be attributed to both reduction and sintering.

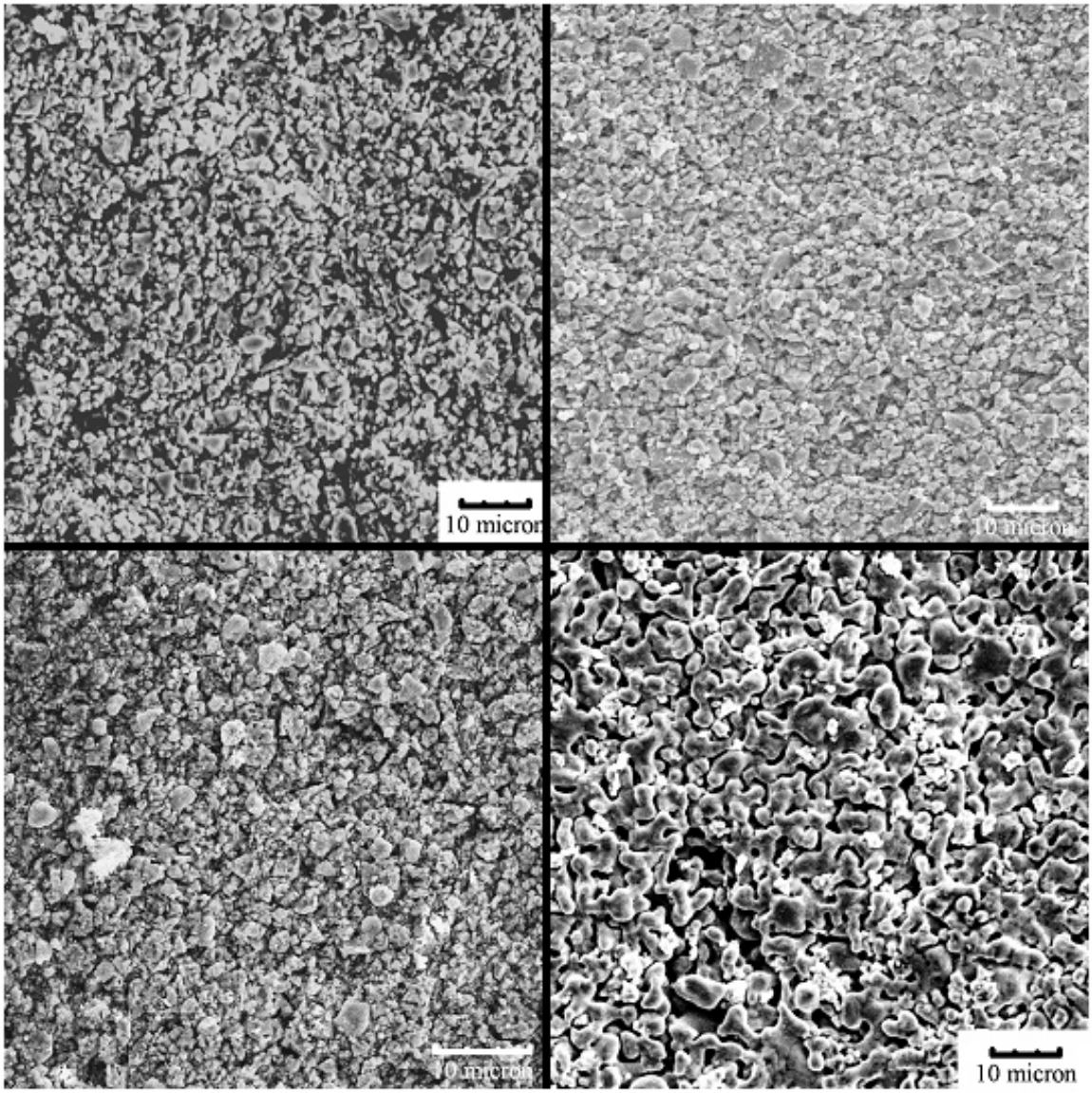

Figure II.4: SEM pictures at a magnification of ~800 were taken of the Fe39Ni8Cr system in the green state at room temperature (top left), after binder burn out at 300 ºC (top right), after reduction had taken place at 680 ºC (bottom left), and during sintering at 915 ºC (bottom right).

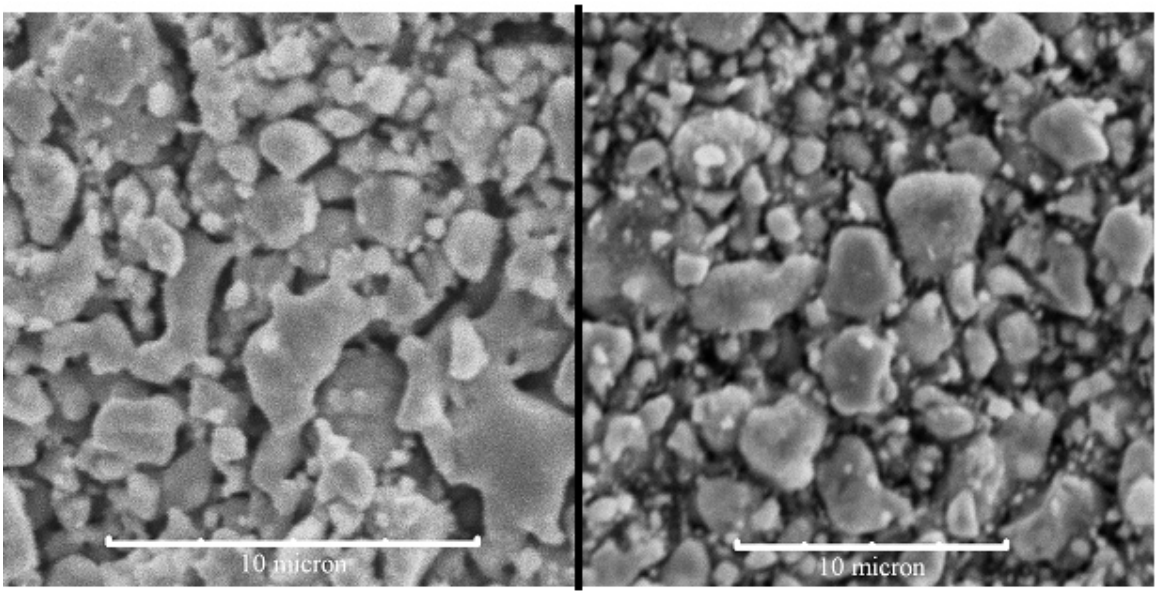

Figure II.5: SEM pictures at a magnification of ~3250 were taken of the Fe39Ni8Cr system at 700 ºC (right), and at 750 ºC (left). The early stages of sintering appear to be starting by 750 ºC (left).

It was then determined that the sintering characteristics of the Fe39Ni8Cr system could be separated from the reduction shrinkage by isothermally holding the sample at 700 ºC for 6 hours before proceeding to higher temperatures to characterize the sintering behavior. The 6-hour hold time was chosen because the reduction shrinkage was changing by less then 0.3% per hour after 6 hours, and the 700 ºC temperature was chosen because sintering had not started to take place yet at that temperature. Figure II.6 shows the total dimensional shrinkage, and a representative temperature profile that was used to characterize sintering. The sample in Figure II.6 was held at 350 ºC to allow the binder to burn out. The sample was then rapidly (200+ ºC/min) heated to 700 ºC to allow reduction to proceed at the highest rate possible before the onset of sintering. Finally, the temperature was ramped to the desired isothermal hold period to characterize the pure

sintering behavior. The above outlined temperature profile seemed to successfully separate the sintering shrinkage from the reduction shrinkage.

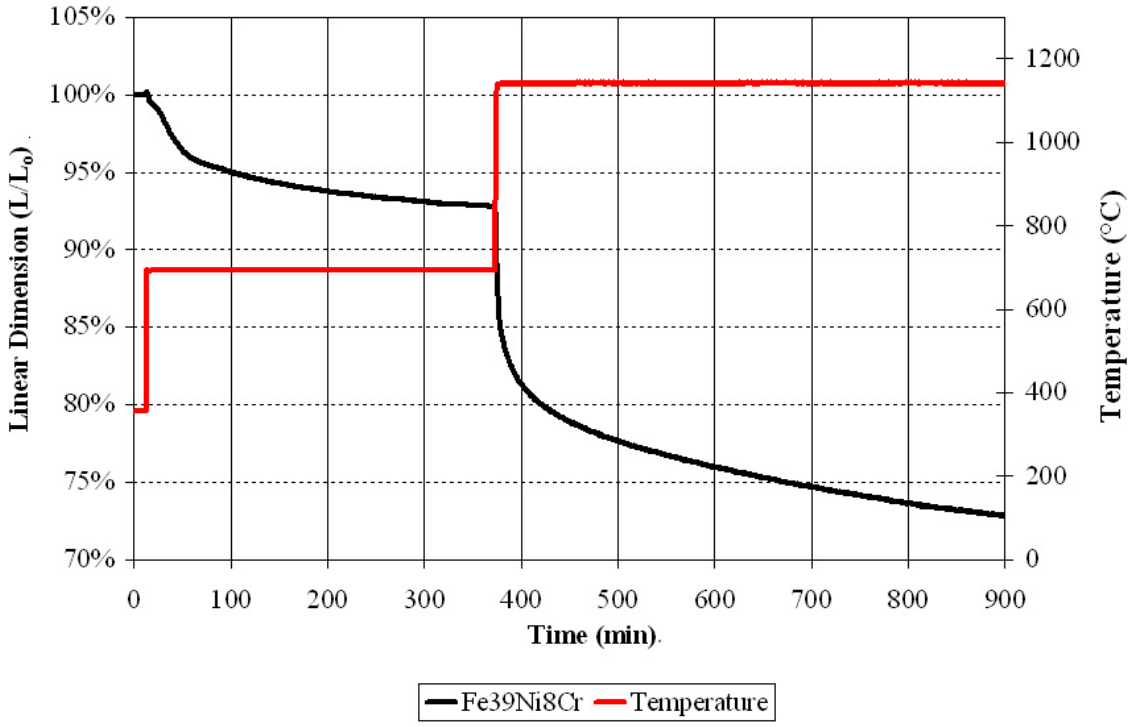

Figure II.6: Typical temperature profile that was used to separate the sintering behavior from the reduction behavior by holding the specimen at 700 ºC for 6 hours.

II.3 Reduction Measurements

Reduction of the Fe39Ni8Cr system requires the reduction of two different oxides, Nickel oxide (NiO), and Magnetite (Fe_3O_4), which are present in the green compact. When the reduction occurs in a hydrogen environment, the reduced oxygen atom combines with hydrogen to form water vapor (hence the switch to using a nonflammable mixture of hydrogen in the experiments) as outlined in the reaction

$$17.6Fe_3O_4 + 39NiO + 8Cr + 109.6H_2 \rightarrow 53Fe39Ni8Cr + 109.6H_2O \ . \qquad \text{(II.3)}$$

Assuming the gas flow entering the reducing sample contains no water vapor, the quantity of water vapor from reduction of the specimen is indicative of the rate of reduction that is occurring in the specimen. Therefore, an Omega RH62C-MV, stick-type hygrometer was inserted into the exhaust line from the furnace to monitor the water vapor from reduction of the specimen, as shown in Figure II.7. The apparatus shown in Figure II.7 could measure both the shrinkage of the specimen with the non-contact dilatometer, and the humidity of the air exiting the system with the hygrometer. First, the measurements of the rate of mass loss from the specimen will be discussed, followed by discussion of the measurements that characterized the shrinkage behavior of the material.

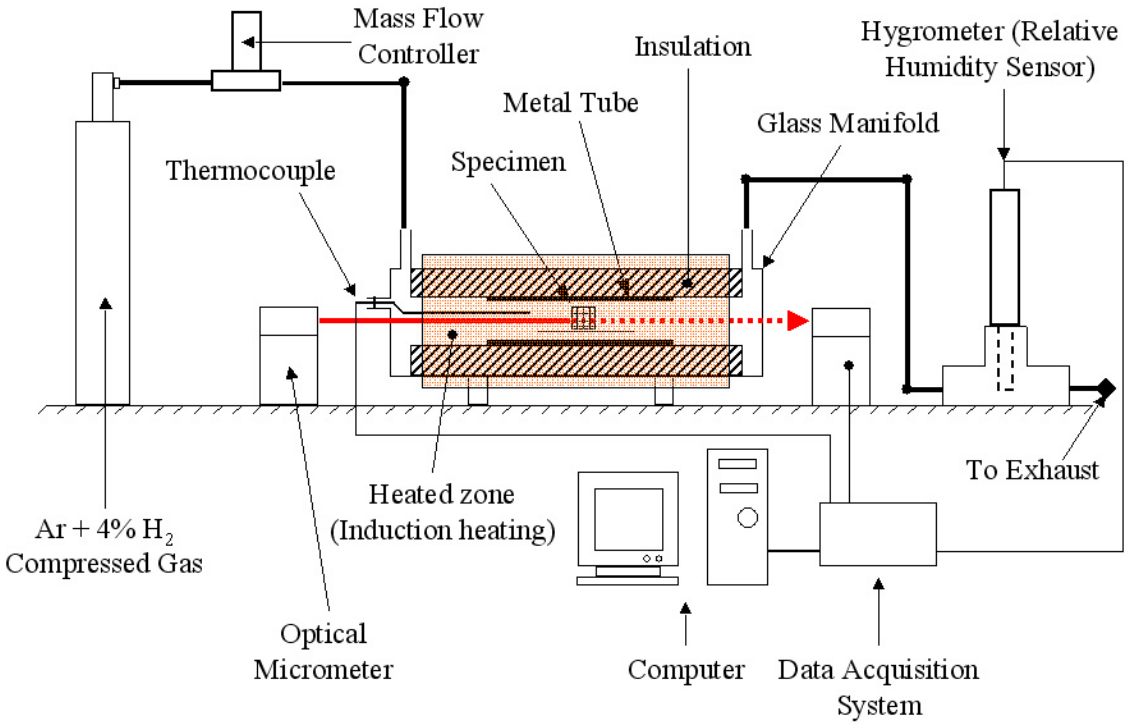

Figure II.7: A hygrometer was inserted into the exhaust line of the equipment used for the sintering studies to aid in the characterization of reduction.

The reduction kinetics were primarily determined through experimental observations, using the hygrometer to measure water emissions from similar honeycomb structures at different temperatures and of different compositions. The samples used for the reduction studies were the Fe39Ni8Cr composition that had been extruded into a honeycomb shape and ground into a wedge, with an initial green state mass of approximately 0.5 grams. Figure II.8 shows the hygrometer output from two reducing Fe39Ni8Cr samples of different masses in the same conditions. The two peaks were identified as being the reduction of NiO and Fe_3O_4, by comparing the temperatures the peaks occurred at to similar runs that contained different ratios of the two oxides, as shown in Figure II.9. Specifically, runs that contained more nickel had larger first peaks, and smaller second peaks. First the reduction kinetics of nickel oxide will be discussed.

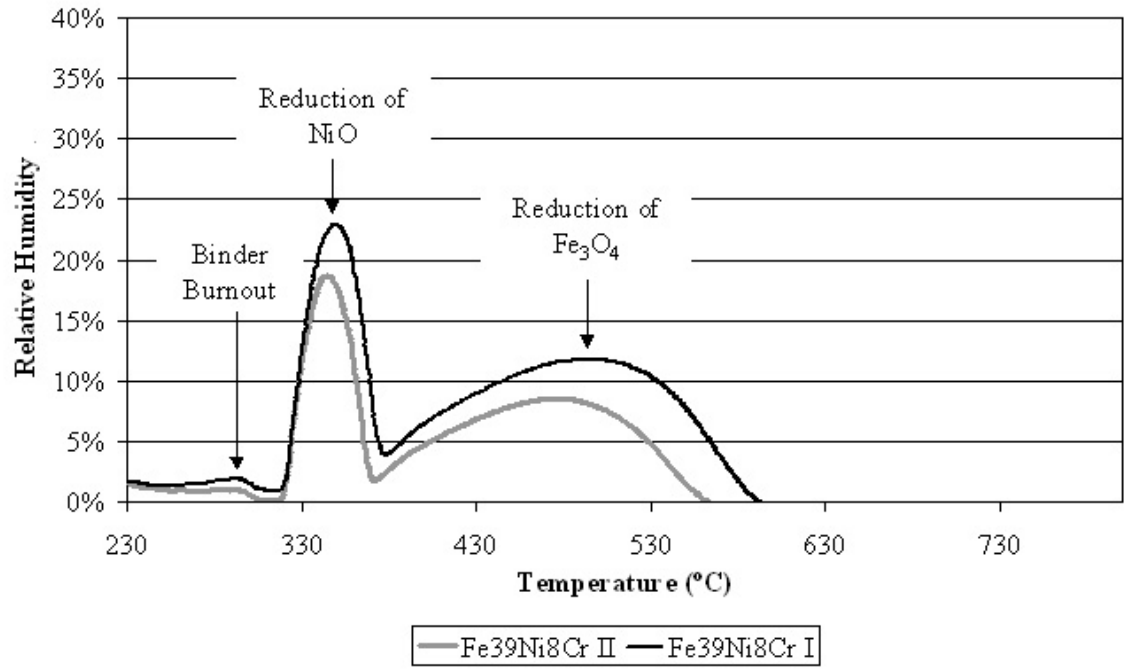

Figure II.8: Hygrometer output from two different mass Fe39Ni8Cr honeycomb samples in 387 sccm Ar + 4% H_2.

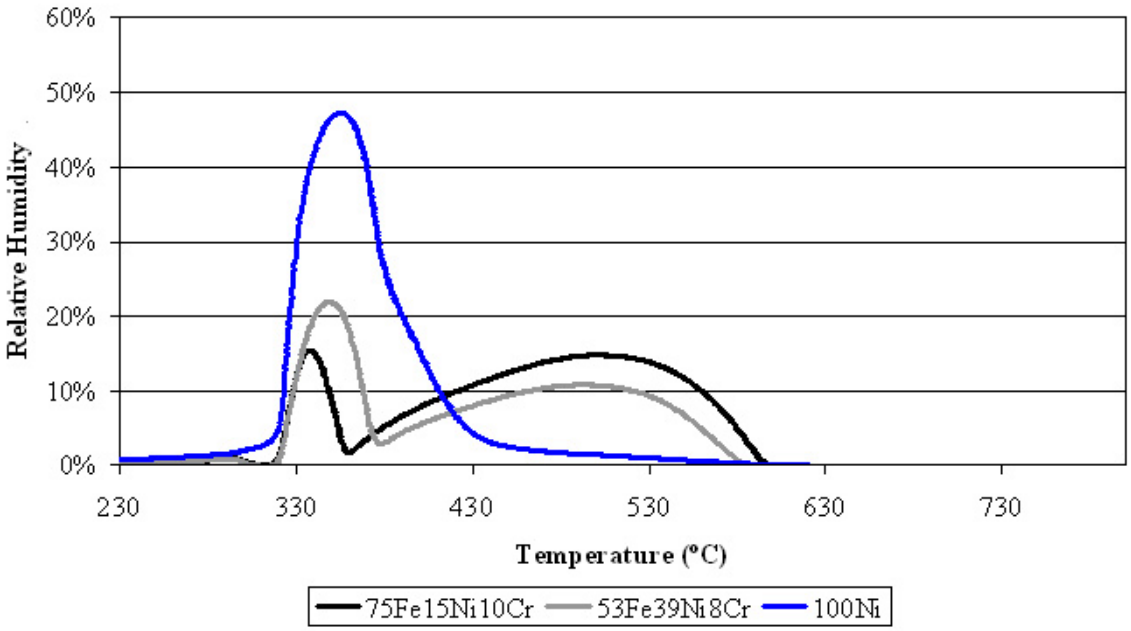

Figure II.9: Each hygrometer peak was linked to the oxide that generated it by comparing how the peaks changed for different initial compositions of oxide powders. All runs were performed on honeycomb structures in 387 sccm Ar + 4% H_2.

The water emissions from similar NiO honeycomb samples of similar masses were measured in a reducing environment at different temperatures as shown in Figure II.10. The slight peak at 4 minutes in the 350 ºC and 372 ºC runs shown in Figure II.10 can be attributed to residual binder burning out of the structure. The hygrometer signal does not return to zero for any run over 372 ºC because the hygrometer starts to pick up the water emissions from reducing magnetite over that temperature. Figure II.11 shows the hygrometer output for two reducing samples of substantially different mass at the same temperature. Figure II.11 shows that the water emissions increased from the larger sample, but the total reduction time for the two samples of different mass was the same at the same temperature. Therefore, from Figure II.10, and Figure II.11, it can be deduced that the time required to reduce nickel oxide is solely dependent on the temperature of the sample, and is independent of the mass of NiO that needs to be reduced. Furthermore, the time required to reduce nickel oxide above 445 ºC appears approximately constant. Assuming this is true, the characterization of the process is specific to the high surface area, low volume geometry of the honeycomb compact.

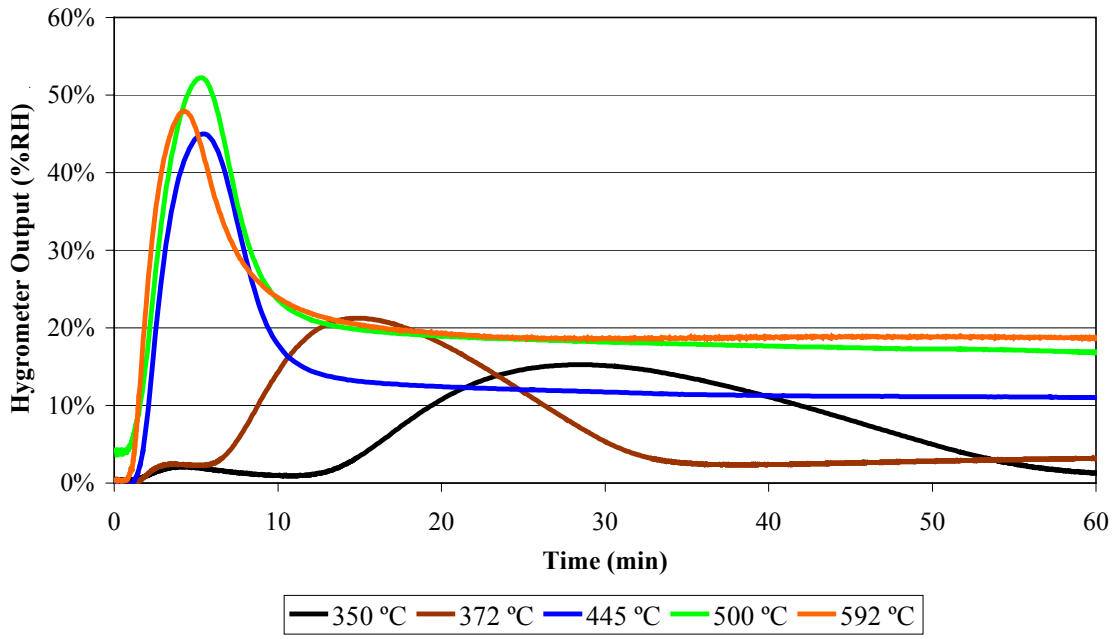

Figure II.10: Hygrometer output from reducing samples of similar mass at different temperatures. The samples were honeycomb compacts of Fe39Ni8Cr in 387 sccm Ar + 4% H_2.

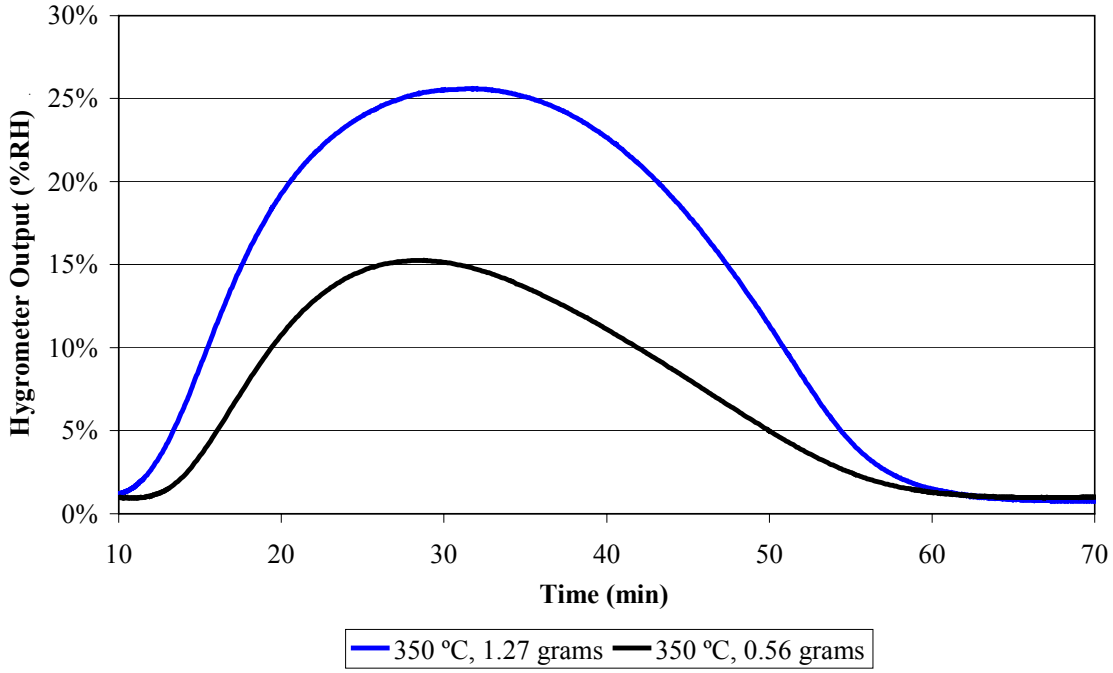

Figure II.11: Hygrometer output from two samples of different mass at the same temperature. The samples were honeycomb compacts of Fe39Ni8Cr in 387 sccm Ar + 4% H_2.

Characterization of the nickel oxide reduction was done by curve fitting a 3-parameter log normal distribution to the data shown in Figure II.10 after modifying it slightly. In other words, it was determined that the measured relative humidity versus time curve at each temperature was representative of the rate of the NiO reduction reaction. Therefore, Figure II.10 was re-plotted after subtracting out the binder burn out peaks, the humidity contribution from the reduction of magnetite, and after normalizing the area under each peak to 1, as shown in Figure II.12. Equation (II.4) was then fit to the normalized data at 350 ºC, 372 ºC, and 445 ºC. The curves at other temperatures were then determined by using temperature-dependent parameters that were obtained by interpolating between the 3 known sets of parameters at different temperatures, as shown in Figure II.13.

$$\dot{\eta}_{NiO}\big|_{T=const} = \frac{a(T)}{f(T)}\exp\left(-0.5\left(\frac{1}{b(T)}\ln\left(\frac{t}{Xo(T)}\right)\right)^2\right)$$
$$a(T) = (0.001285)T - 0.4183,\ b(T) = (0.003218)T - 0.7383,$$
$$Xo(T) = (-0.2200)T + 100.471 \qquad \text{(II.4)}$$
$$f(T) = (-8.277\times10^{-9})T^4 + (9.678\times10^{-6})T^3 + (0.00415)T^2 + (0.799)T - 61.292$$
$$(\text{Normalization function})$$
$$\eta_{NiO}(T,t) = \int_{T_i}^{T_f}\left[\int_0^t\left(\dot{\eta}_{NiO}\big|_{T=const}\,dt\right)\right]dT,\ \eta_{NiO}(T,0) = 0,\ [0 \le \eta_{NiO} \le 1]$$

Here, T is temperature in Celsius and t is time in minutes. Unfortunately, equation (II.4) is only the isothermal rate of reduction equation, and is not valid for temperature change. Therefore, to form a generalized rate of reduction equation, Equation (II.4) was integrated with respect to time at different temperatures to form the surface shown in

Figure II.14. An arctangent function with temperature-dependent properties was then fit to the surface as shown in Figure II.15. Finally, the arctangent function was differentiated to give the rate of reduction for NiO under varying temperatures as

$$\frac{d\eta}{dt} = \frac{d\left[CC(T)\right]}{dT}\frac{dT}{dt} + \frac{d\left[DD(T)\right]}{dT}\frac{dT}{dt}\arctan\left(\frac{\left(t - AA(T)\right)}{BB(T)}\right) + DD(T)\left(\frac{\frac{1 - \frac{d\left[AA(T)\right]}{dT}\frac{dT}{dt}}{BB(T)} - \frac{\left(t - AA(T)\right)}{BB(T)^2}\frac{d\left[BB(T)\right]}{dT}\frac{dT}{dt}}{1 + \frac{\left(t - AA(T)\right)^2}{\left(BB(T)\right)^2}}\right)$$

$$\frac{d\left[AA(T)\right]}{dT} = \left(-0.00156\right)T + 0.387, \quad \frac{d\left[BB(T)\right]}{dT} = \left(-0.00163\right)T + 0.5947 \qquad \text{(II.5)}$$

$$\frac{d\left[CC(T)\right]}{dT} = \left(8.174\times10^{-6}\right)T - 0.00317,$$

$$\frac{d\left[DD(T)\right]}{dT} = \left(-6.825\times10^{-8}\right)T^2 + \left(4.698\times10^{-5}\right)T - 0.00811 \ .$$

Equation (II.5) should be valid for the reduction of NiO at any flow rate, assuming a 4% Hydrogen concentration, and that there is sufficient H_2 to prevent the reduction reaction from being stoichiometrically limited. The mass at which the process becomes stoichiometrically limited can be written as

$$M_{st} = \frac{\left(X_{H2}\right)\left(Q\right)\left(\rho_{H2}\right)\left(t\right)\left(c_o\right)}{\left(m_o\right)\left(c_{H2}\right)} \ , \qquad \text{(II.6)}$$

where M_{st} is the stoichiometrically limited mass, X_{H2} is the volume fraction of H_2 in the flow rate, Q is the volumetric flow rate of gas, ρ_{H2} is the density of hydrogen gas at atmospheric pressure, t is the time required for NiO reduction, c_o is the molar mass of oxygen, m_o is the initial weight percent of oxygen associated with NiO in the green compact, and c_{H2} is the molar mass of H_2. For a flow rate of 387 standard cubic centimeters per minute (sccm) of Ar + 4% H_2, the green compact must weigh approximately 36 grams before the process is stoichiometrically limited.

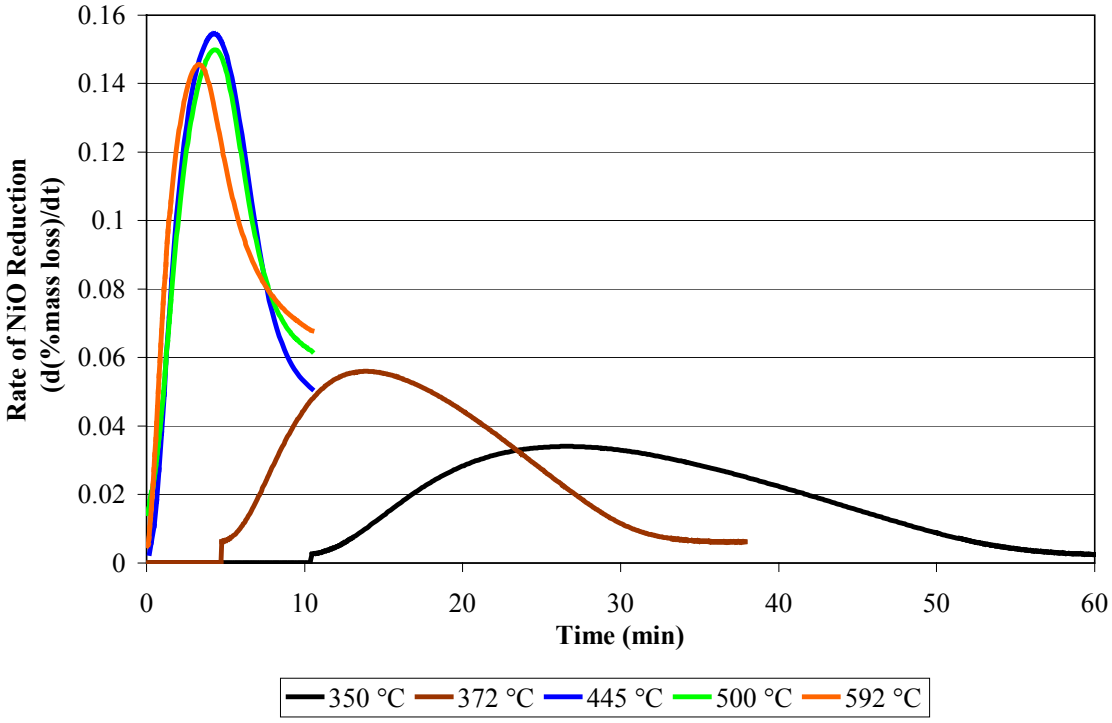

Figure II.12: Normalized isothermal rate of reduction of NiO from honeycomb Fe39Ni8Cr structure in 387 sccm Ar + 4% H_2.

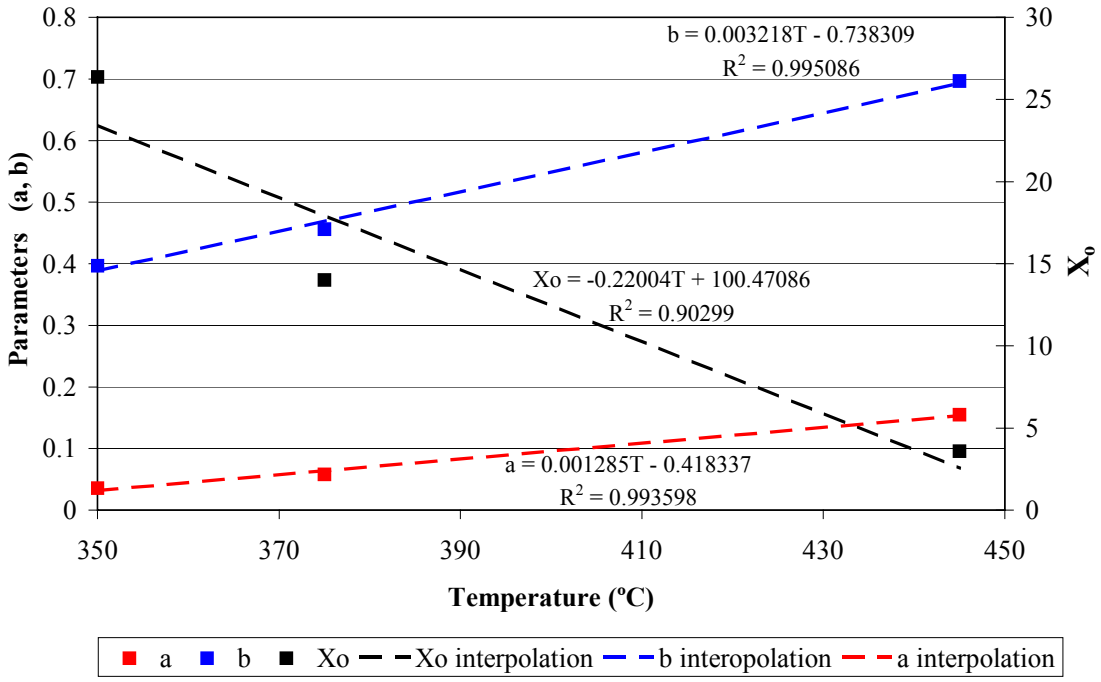

Figure II.13: Interpolated parameters in Equation (II.4) for isothermal reduction rate.

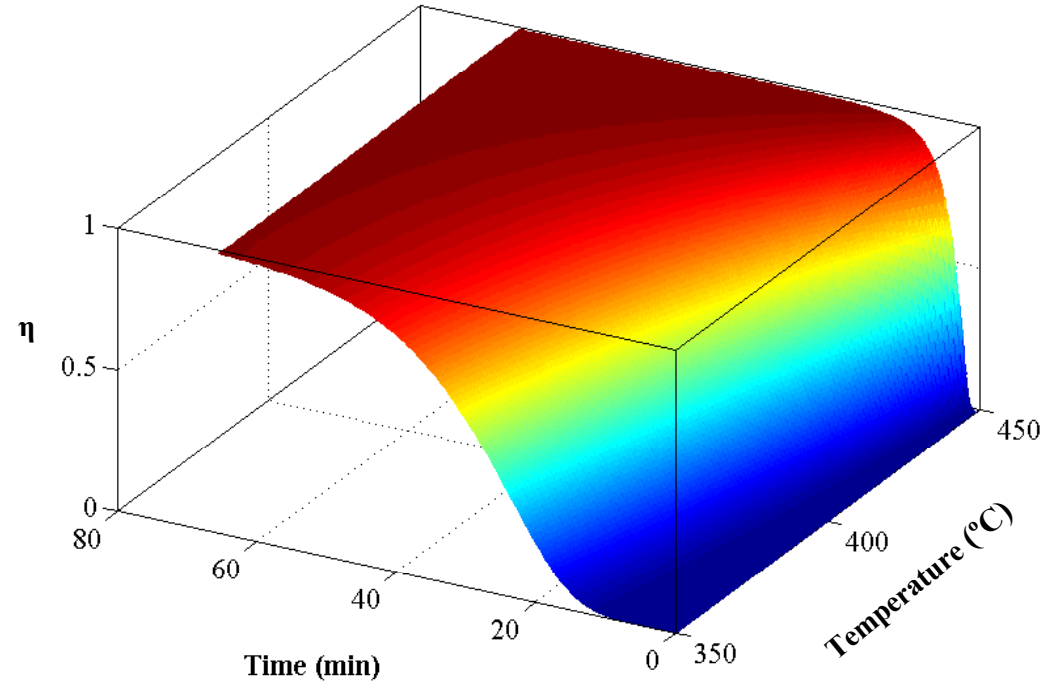

Figure II.14: Nickel oxide reduction parameter η as a function of temperature and time, based on Equation (II.4).

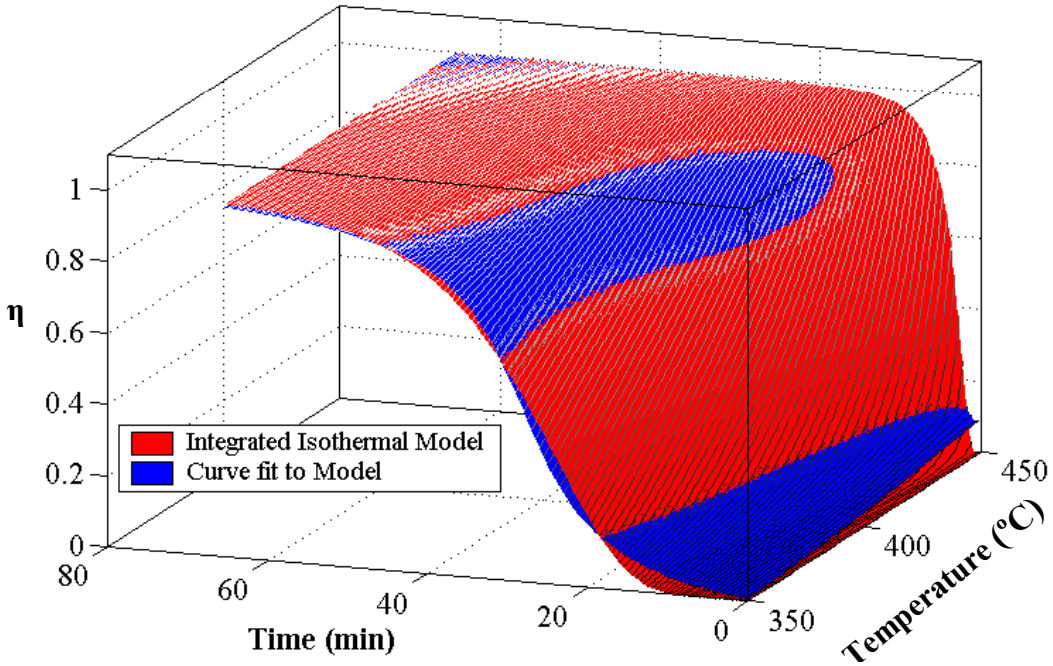

Figure II.15: Comparison of arctangent curve fit surface to reduction surface derived from Equation (II.4).

The water emission from the reduction of loose magnetite powder spread ~2mm thick on a ceramic platelet was measured under isothermal conditions for several different temperatures, as shown in Figure II.16. Similar reduction studies were performed on Fe39Ni8Cr honeycomb compacts with very similar results to the ones outlined below. However, the presence of binder and NiO in the honeycomb samples made the results more difficult to interpret, so for conciseness, only the loose magnetite powder results are shown. The time for magnetite to reduce was observed to depend on the initial mass of the specimen, the gas flow rate, the gas concentration, and the temperature of the sample. After careful observations, it was determined that the reduction of magnetite was limited by the partial pressure of water vapor in the furnace. Specifically, it was determined that the rate of reduction of magnetite at a given temperature proceeded at a constant rate proportional to the partial pressure of water vapor in the furnace until the majority of the magnetite had reduced. After the majority of the magnetite had reduced, the rate of reduction slowed significantly. Figure II.17 outlines the deduced reduction process, which demonstrates similar trends to the measurements in Figure II.16. The initial humidity spike in the measurements was assumed to be a transient by-product of rapidly heating the specimen from a temperature where reduction does not occur to one where it occurs rapidly. Specifically, the furnace environment rapidly changed from near zero relative humidity to an artificially high humidity as the specimen came up to temperature and started to rapidly reduce in a very favorable dry environment, and then the reduction slowed to the equilibrium reducing partial pressure. There is no need to characterize the transient reduction rate, because the

actual samples will never be heated near the 200 ºC/min ramp rate that caused the transient effect in the experiments.

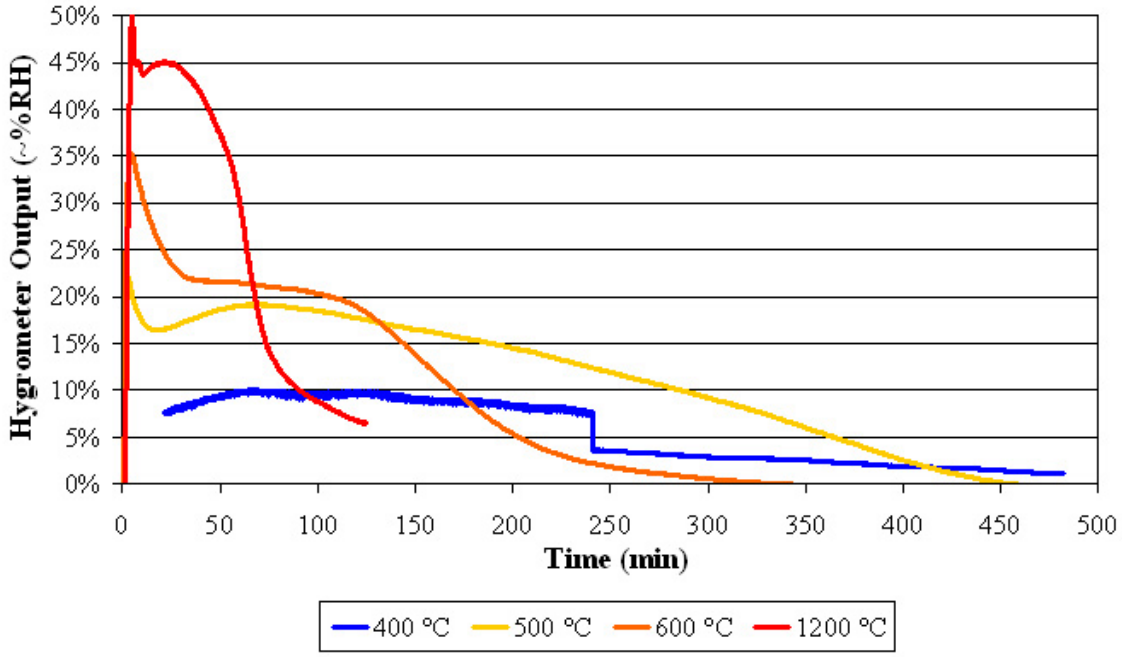

Figure II.16: Uncalibrated hygrometer output from isothermal reductions of magnetite. Samples were loose Fe_3O_4 powder in 387 sccm Ar + 4% H_2.

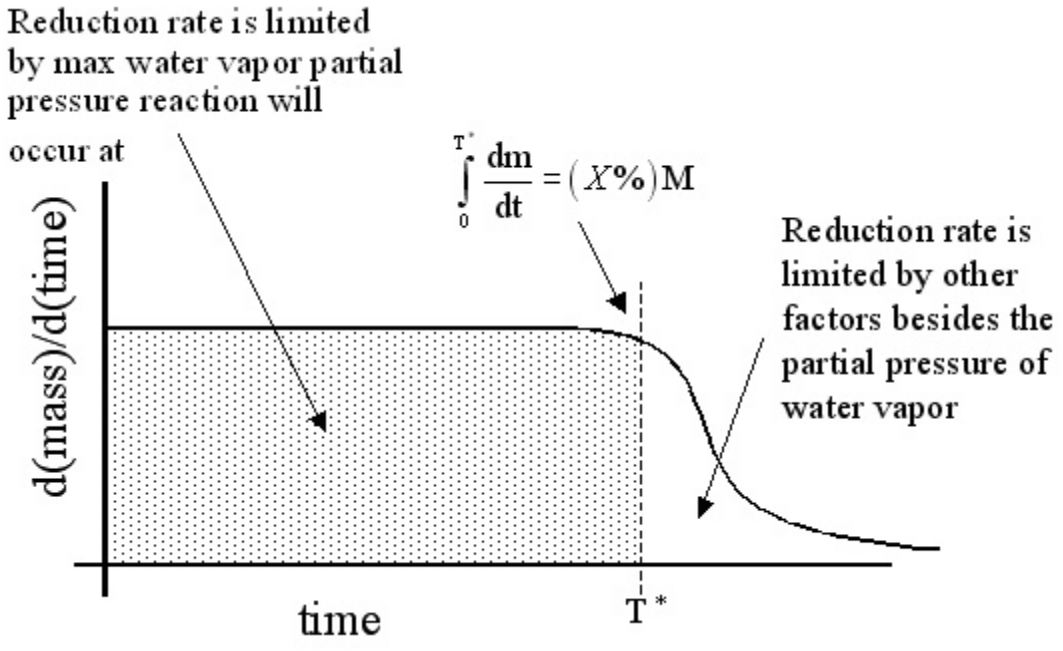

Figure II.17: Deduced rate of reduction of magnetite at constant temperature from experimental observations.

Assuming that reduction at a constant temperature occurs at a constant partial pressure as shown in experimental observations, then the total mass loss from the specimen can be written from the ideal gas law i.e,

$$m_{Oxygen}\left(P_{H_2O}\right) = \frac{P_{H_2O} V_{total}}{RT} c \ , \qquad \text{(II.7)}$$

where P_{H_2O} is the partial pressure of water vapor, V_{total} is the total volume of gas at that partial pressure, R is the universal gas constant, T is the temperature of the gas in Kelvin, and c is the molar mass of oxygen. Equation (II.7) can be differentiated and written in terms of the volumetric flow rate i.e.,

$$\dot{m}_{Oxygen} = \frac{P_{H_2O} Q_{total}}{RT} c \ , \tag{II.8}$$

where Q_{total} is the total volumetric flow rate of air passing over reducing sample. Taking a control volume around the reducing sample as shown in Figure II.18, Dalton's Law of partial pressures leads to

$$\begin{aligned}
&\text{Entering} \\
&P_{Ar} + P_{H_2} = P_{total} = P_{atm} \\
&\text{Leaving} \\
&P'_{Ar} + P'_{H_2} + P'_{H_20} = P_{total} = P_{atm} \\
&\text{Relations} \\
&P_{Ar} = P'_{Ar} \ \Rightarrow \ \text{moles, flow rate, and temperature} \\
&\qquad\qquad \text{remain constant for Argon} \\
&\therefore \ P_{H_2} = P'_{H_2} + P'_{H_20} \ ,
\end{aligned} \tag{II.9}$$

where P_{Ar} is the partial pressure of Argon gas entering, P_{H_2} is the partial pressure of H_2 gas entering, P_{total} is the total pressure, P_{atm} is the atmospheric pressure, P'_{H_2O} is the partial pressure of water vapor exiting, and the other primes denote the partial pressure of the indicated gas leaving the control volume.

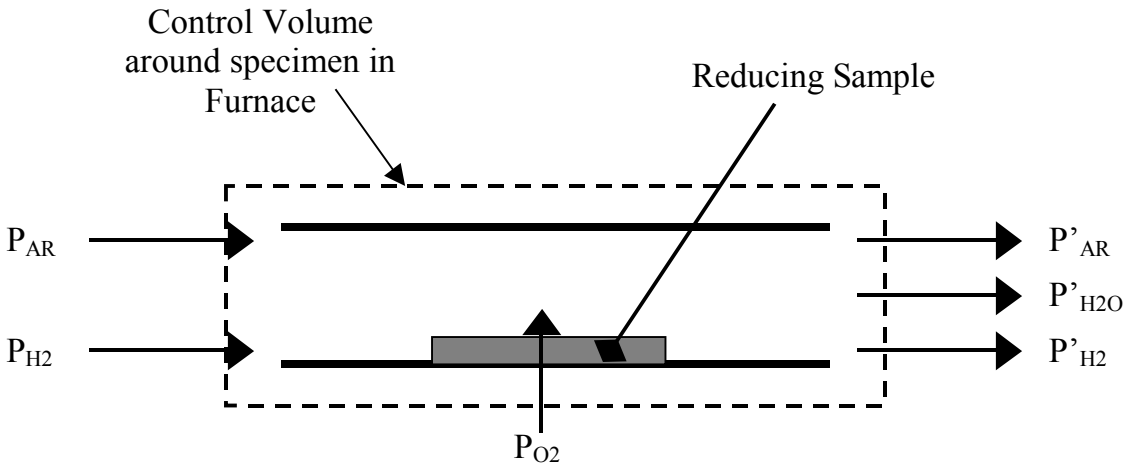

Figure II.18: Control volume around reducing specimen in furnace.

Taking into consideration the observation that the reduction process is limited by the partial pressure of water vapor to hydrogen, which was observed to only depend on the temperature of the reducing sample, the following holds

$$\frac{P'_{H_2 0}}{P'_{H_2} + P'_{H_2 0}} = \frac{P'_{H_2 0}}{(1\text{-}X_{Ar})P_{atm}} = f(T) \quad . \tag{II.10}$$

Here, X_{Ar} is the volume percent or mole fraction of Argon gas entering the system and f(T) is the equilibrium partial pressure of the reducing magnetite as a function of temperature. Using the definition of relative humidity, the equilibrium partial pressure can be can be rewritten as

$$\begin{aligned} RH &= \frac{\text{Current Partial Pressure of Water vapor}}{\text{Saturation Vapor Pressure of Water}} = \frac{\left[P_{H_2O}\right]}{\left[P_{sat.\ VP}\right]} \\ \Rightarrow f(T) &= \frac{\left[RH(T)\right]\left[P_{sat.vap.}\right]}{\left[1\text{-}X_{Ar}\right]\left[P_{atm}\right]} \ , \end{aligned} \tag{II.11}$$

where RH(T) is the relative humidity of the system as a function of temperature, and $P_{sat.vap.}$ is the saturation vapor pressure of water. Substituting Equation (II.11) and (II.10) back into Equation (II.8) yields

$$\dot{m}_{Oxygen} = \frac{\left[f(t)(1 - X_{Ar})P_{atm}\right]Q_{total}}{RT}c \quad . \tag{II.12}$$

Equation (II.11) could be used in conjunction with the measured relative humidity to determine the temperature-dependent equilibrium partial pressure associated with reducing magnetite. Unfortunately, the stick type hygrometer used was not accurate enough to give a repeatable steady state relative humidity. Specifically, when Equation (II.12) was integrated at a constant temperature using the measured relative humidity, the total mass lost from the system was usually found to be ~40% more then the mass that actually left, based on mass measurements before and after reduction. Therefore, a corrected value of relative humidity was used such that when it was integrated in Equation (II.12), it would give the measured oxide mass loss. The implicit assumption in correcting the hygrometer output in this manner is that the accuracy of the hygrometer is constant over the measured range of humidity for each individual experiment. This seems to be a valid assumption based on the published tolerances of the hygrometer, and the relatively small range that the measured humidity varied over during most

experiments. Figure II.19 shows the 'calibrated' relative humidity output from the reducing samples at each temperature. Figure II.20 shows the calibrated equilibrium reducing humidity from each isothermal experiment, as well as the equilibrium reducing humidity from a single slow ramp rate (0.85 °C/min) experiment. Figure II.21 shows the time required for a given mass percent of the oxide to leave the structure for the given starting mass. The total time for all the oxide mass to leave is dependent on the initial mass of the structure. However, if the reduction process is as deduced in Figure II.18, then the slope of the line in Figure II.21 should be constant up until a constant mass percent of oxide lost. As illustrated in Figure II.21, the rate of mass loss appears to be constant, until approximately 85% of the initial mass has reduced, at which time the rate of reduction slows.

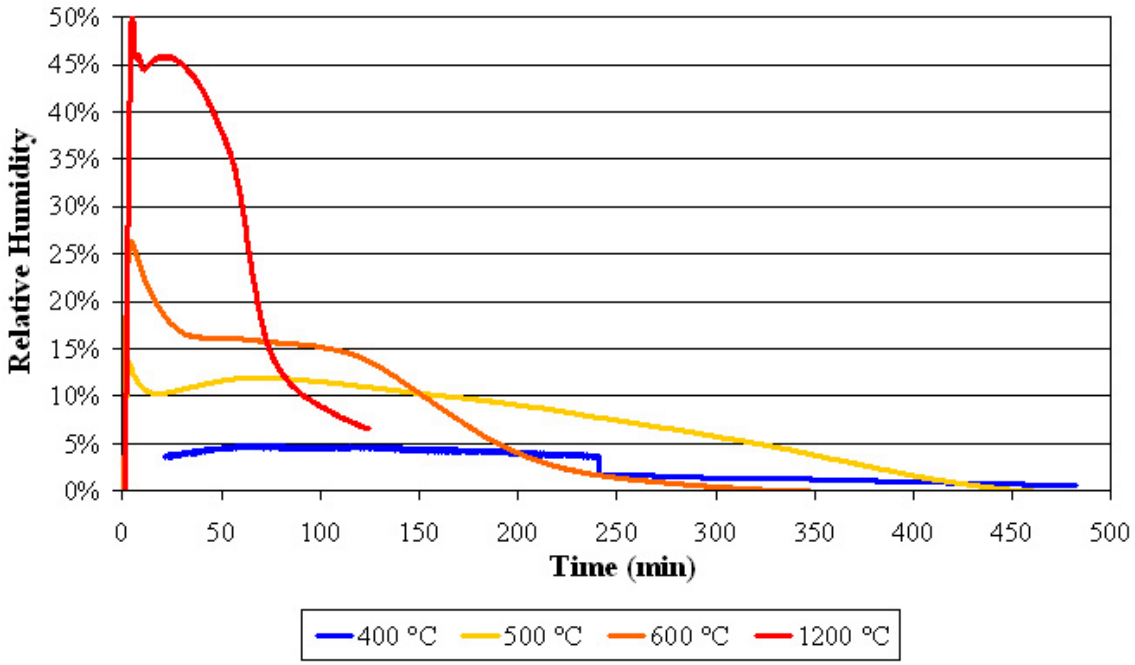

Figure II.19: Calibrated hygrometer output from isothermal reductions of magnetite. Samples were loose Fe_3O_4 powder on ceramic platelet in 387 sccm Ar + 4% H_2.

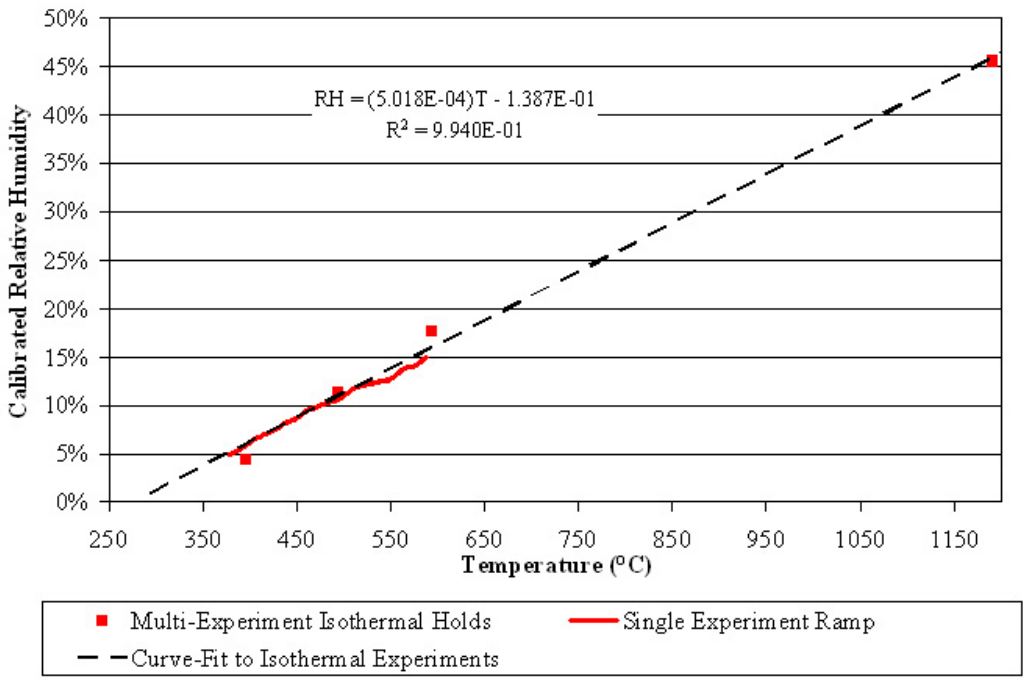

Figure II.20: Calibrated relative humidity emissions from reducing magnetite specimen at its equilibrium partial pressure. The multi-experiment isothermal hold experiments were from loose Fe_3O_4 powder, while the ramp experiment was from an Fe39Ni8Cr honeycomb. All experiments were performed in 387 sccm Ar + 4% H_2.

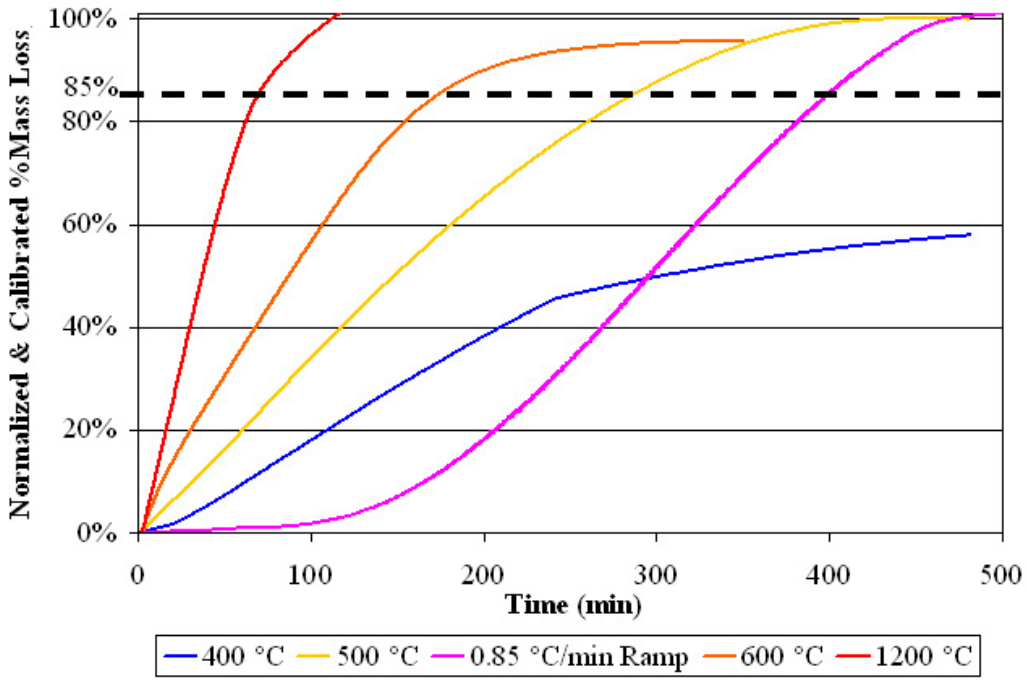

Figure II.21: Rate of mass loss from reducing samples is constant until approximately 85% of initial oxide mass has left the structure, at which time it slow down.

Equation (II.11) was then used in conjunction with the calibrated relative humidity data shown in Figure II.20 to determine the temperature dependent equilibrium partial pressure of reducing magnetite, i.e.,

$$f(T) = 3.23\times10^{-4}(T) - 0.0893 \quad , \qquad \text{(II.13)}$$

where T is the temperature in Celsius. The experimentally observed equilibrium partial pressure for the reduction of Fe_3O_4 at different temperatures was then compared to the theoretical thermodynamic equilibrium partial pressure at different temperatures (given by the Ellingham diagram) as shown in Figure II.22 (O. Kubaschewski 1979). The overall agreement between the experimental results and theoretical results are very good,

with the deviations most likely being attributed to the kinetics of reduction lagging behind the thermodynamic limit, and some experimental error. From Figure II.21, and other experiments, it was determined that the rate of reduction after the first 85% of the mass had reduced was approximately 1/5 the rate of the equilibrium rate. A non-dimensional parameter was then formulated from the above equations that gave the percent of magnetite that would reduce as a function of time, temperature, and partial pressure, i.e.,

$$\eta_{Fe} = \frac{\int_0^t \dot{m}_{Fe}\, dt}{X_{Fe} m_0} \quad , \tag{II.14}$$

where $\dot{m}_{Fe}$ is the rate of lass loss given by equation (II.12), X_{Fe} is the percent of magnetite oxide in the unfired green compact, and m_o is the initial mass of the green compact.

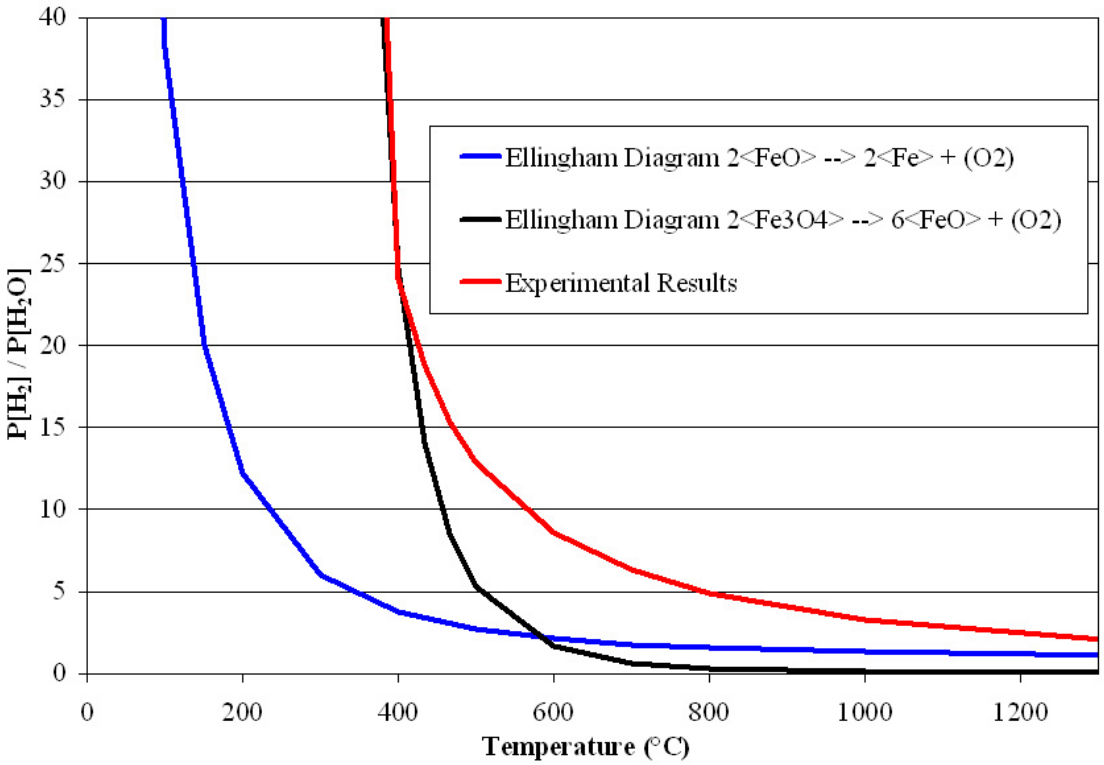

Figure II.22: Comparison of experimentally observed and theoretical thermodynamic equilibrium partial pressure for the reduction of Fe_3O_4.

II.4 Characterization of Mechanical Properties

Uniaxial tension tests were performed on thin dog-bone strip specimens at room temperature and elevated temperatures under stroke control. The dimensions of the specimens tested in all cases are shown in Figure II.23. The test samples were made from extruded Fe39Ni8Cr strips that were stamped out into dog-bone shaped specimens while in the green state using a special dog-bone shaped template. The test specimens were formed using the same extrusion process used to extrude the hybrid structures. The test specimens were fired 3 times to minimize the porosity in the structure and ensure complete reduction. The first two times they were fired to 1300 °C and held for 10 hours. The third time they were fired to 1350 °C and held for 2 hours. The result was strip specimens with an average porosity of 15%, which is ~ 3% lower then the level of porosity achieved in most of the manufacturing sintering runs. The long firing times most likely also resulted in extensive grain growth, which is somewhat representative of the actual manufactured specimens that are cooled very slowly to anneal the stresses.

The room temperature tests were performed on a 1020 Instron test frame with, a 1000 Lb load cell and screw driven displacement control. Four samples were tested at two different strain rates as shown in Figure II.24. The engineering strain was calculated by dividing the stroke control displacement by the initial measured gauge length. The engineering stress was measured by dividing the recorded force output by the initial measured cross-sectional area. The material exhibited no substantial strain rate affects at room temperature. The large difference in the elongation to failure can be attributed to the different defect structures in each of the specimens. Specifically, upon examining the fractured specimens, a large void was observed at the fracture surface in run ‘C’, a small

void was observed at the fracture surface of runs ‘B’ and ‘D’, and no defects were visible on the fracture surface of run ‘D’. The tested specimens are highly sensitive to defects because of how thin they are, and the manufacturing process. However, the defects did not seem to have a substantial affect on the repeatability of the experiments prior to fracture.

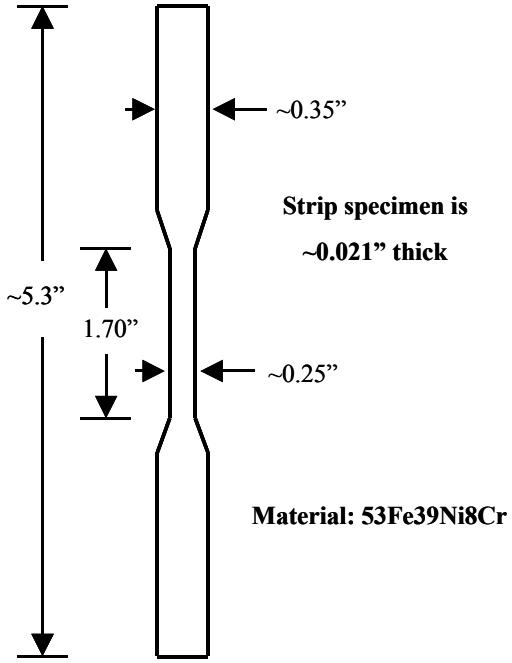

Figure II.23. Dimensions of dog-bone sample used for uniaxial tension tests.

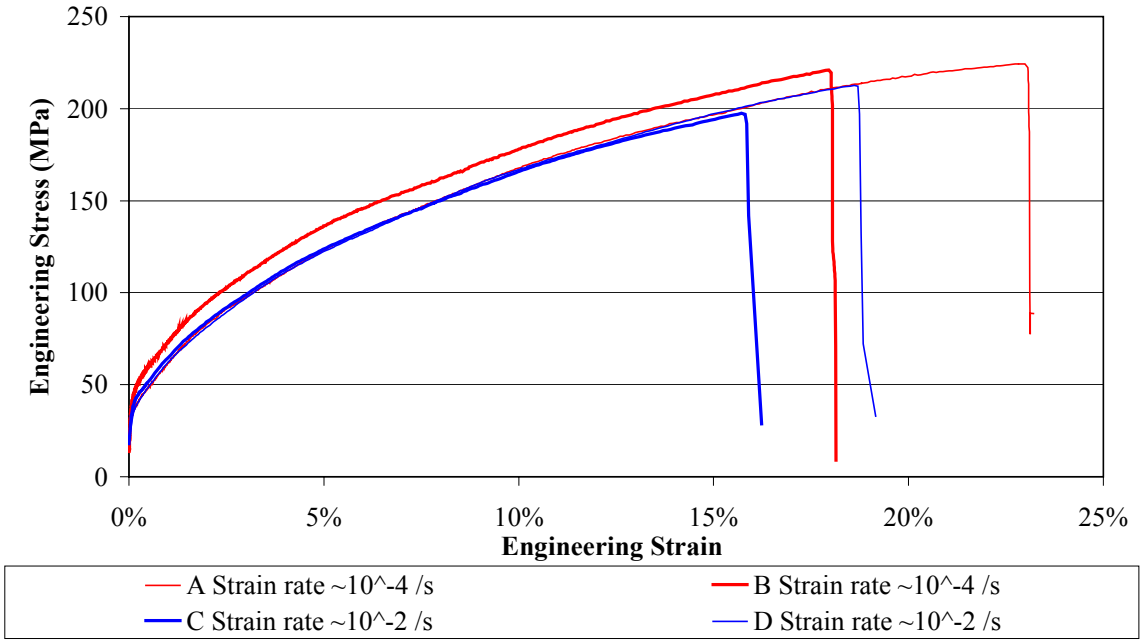

Figure II.24: Uniaxial tension tests performed at room temperature at two different strain rates. The tests were performed on Fe39Ni8Cr dog-bone samples with an initial porosity of ~15.5%

The high temperature tension test measurements required substantially more setup to perform. The tests were performed on a hydraulic 810 MTS load frame with a 2000 lb load cell using an Applied Test Systems (ATS) 1050 furnace. A special high temperature set of grips was built out of high temperature A-286 like super alloy as shown in Figure II.25. The grips had a 0.7" wide slot to allow a ceramic plate to be inserted to keep the high temperature test sample from coming directly in contact with the grips. The grips were externally cooled with water coils and an air jet, as shown in Figure II.26. The entire experimental setup is shown in Figure II.26, with a close-up of the grips and furnace shown in Figure II.27.

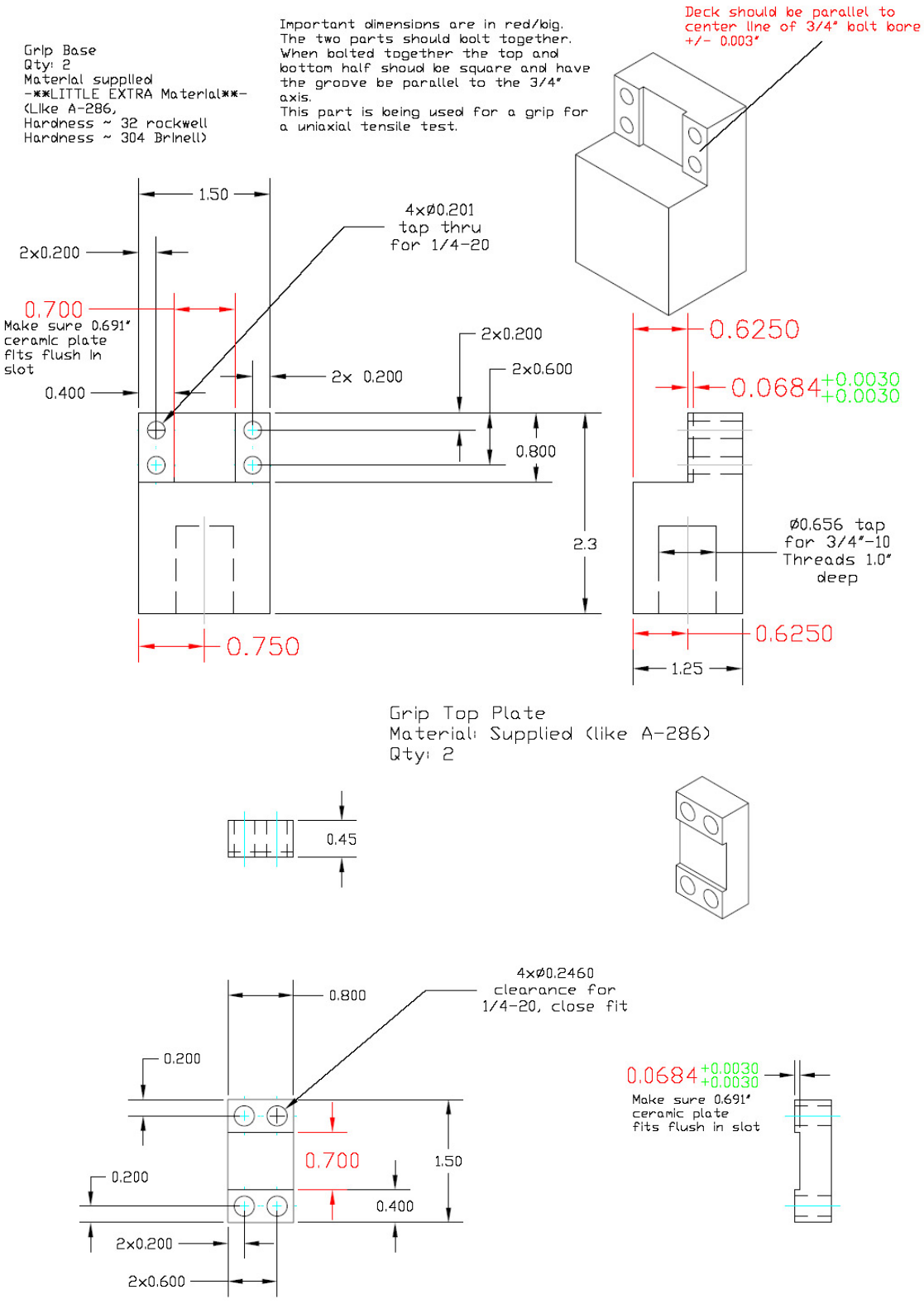

Figure II.25: Machine drawings for high temperature grips used for high temperature tests.

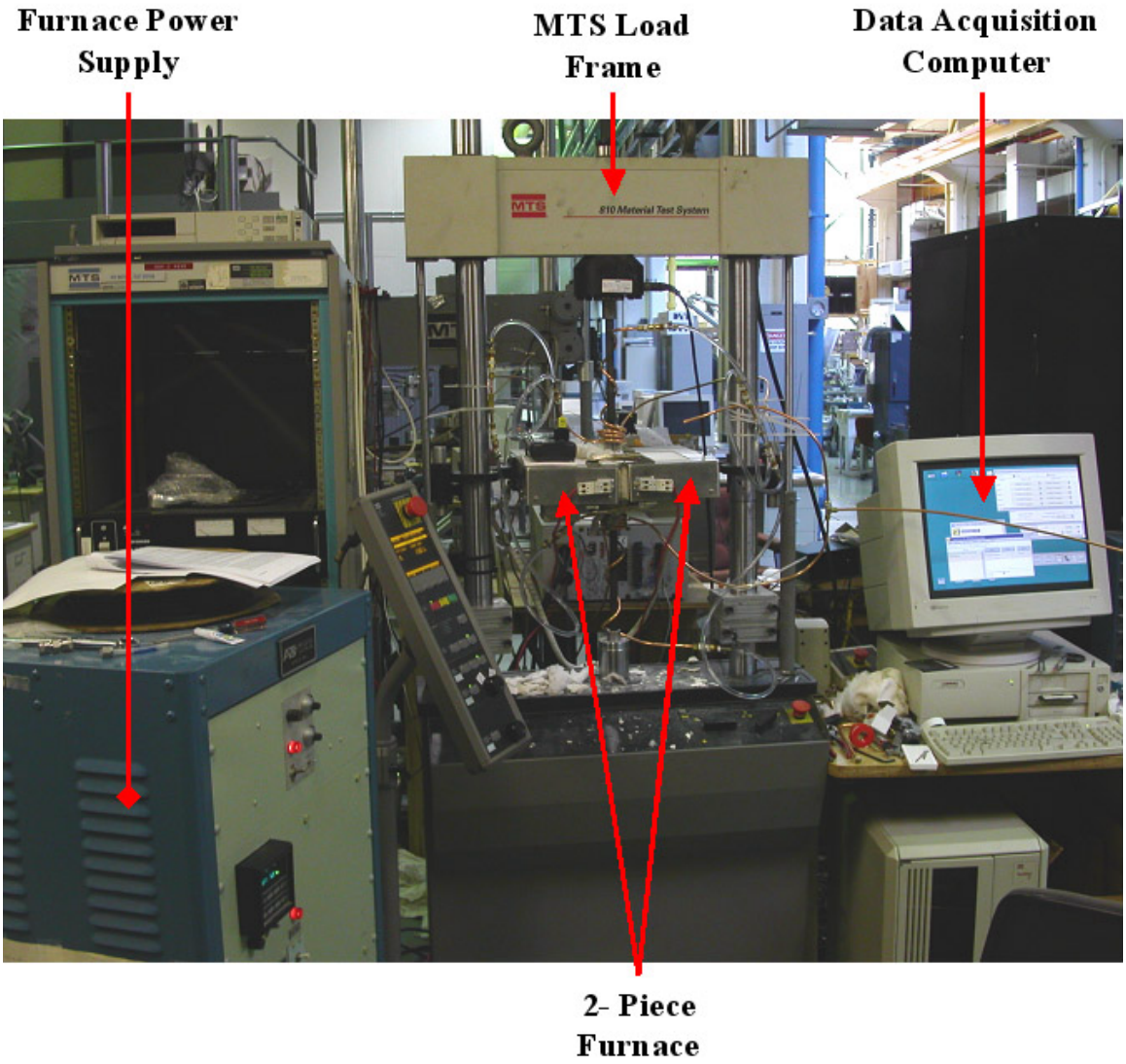

Figure II.26: Layout of high temperature experiments. An MTS load frame (center) was used for the uniaxial tension pulls. The 2-piece ATS furnace was used to heat the gauge length of the specimen, and the ATS power supply (left) was used to power and regulate the furnace temperature. The computer (right) was used to record the measured displacement, time and load on the specimen.

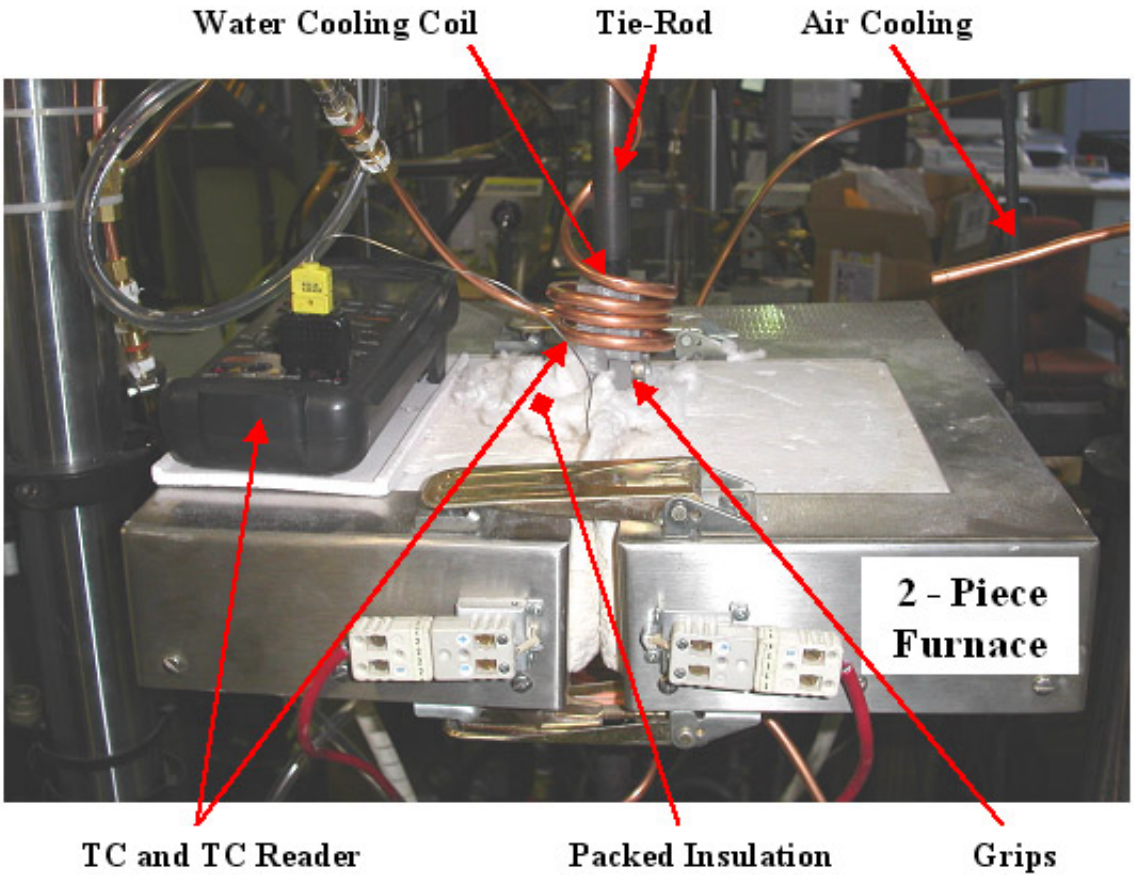

Figure II.27: Close-up of two-piece ATS 1050 furnace and experimental setup.

The given experimental setup was first used to determine the approximate range of temperature where the plastic deformation of the samples was affected. Figure II.28 shows the resulting stress strain curves measured from 360 °C to 820 °C on the Fe39Ni8Cr dog-bone samples. The significant decrease in elongation to failure at increased temperatures is most likely due to the high level of porosity in the samples and rapid localization of deformations at high temperatures. From Figure II.28, it was determined that viscoplastic relaxation started taking place above approximately 575 °C. Furthermore, it was determined that uniaxial tests that were supposed to include a

relaxation hold period should not exceed approximately 2.25% strain or the specimen would be in jeopardy of failing before the relaxation period.

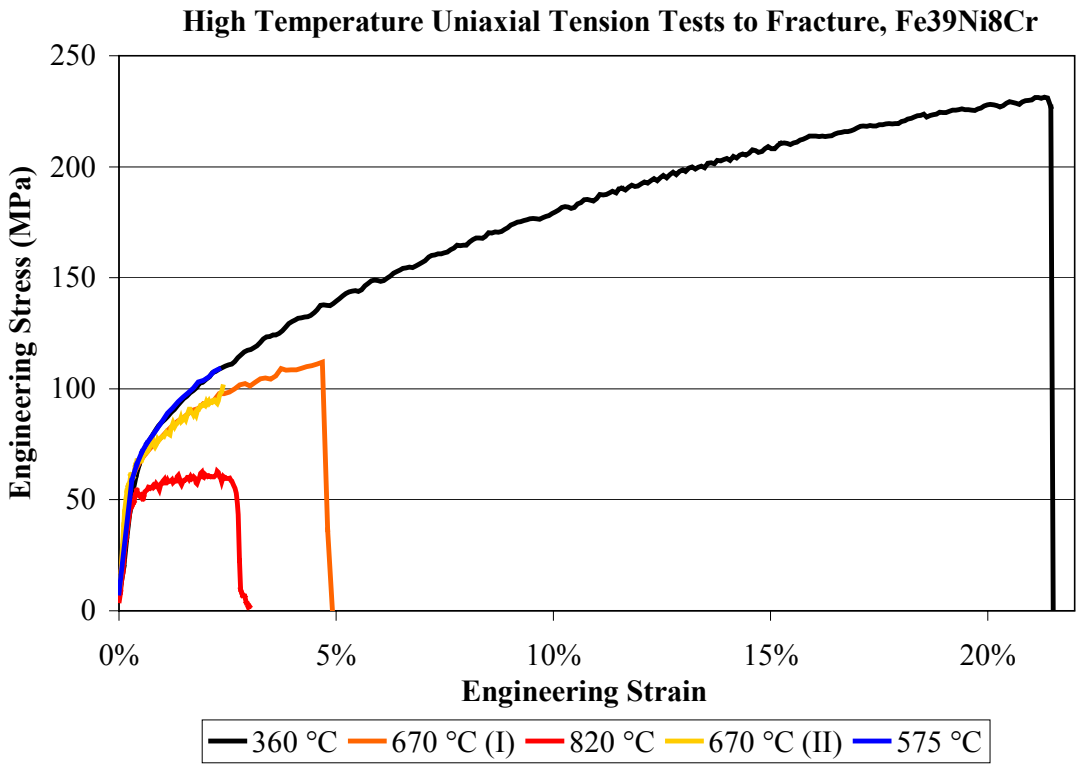

Figure II.28: Stress strain curves from high temperature uniaxial tests. Samples were tested at a strain rate of 2×10^{-4} s^{-1} to failure, except for 670 °C (I), and 575 °C that were not tested to failure. The samples were Fe39Ni8Cr dog-bone samples with an initial porosity of ~15.5%.

After the relaxation temperature region was determined, uniaxial tension tests were performed at two different strain rates until ~2.25% strain at which point a relaxation test was performed by holding the displacement constant and measuring the decay of force in the sample. This type of experiment was performed at several temperatures at and above 575 °C. Figure II.29 shows the measured stress-strain curve

up to ~2.25% strain. Figure II.30 shows the measured relaxation data from the terminal strain value during the tension test as shown in Figure II.29. Figure II.31 shows the calculated strain rate exponent at a strain of 0.3% and 2% using equation (II.15).

$$\sigma\big|_{\varepsilon_1,\,\dot{\varepsilon}_2}\ m = \ln\left(\frac{\sigma\big|_{\varepsilon_1,\,\dot{\varepsilon}_1}}{\sigma\big|_{\varepsilon_1,\,\dot{\varepsilon}_2}}\right)\Bigg/\ln\left(\frac{\dot{\varepsilon}_1\big|_{\varepsilon_1}}{\dot{\varepsilon}_2\big|_{\varepsilon_1}}\right) \qquad \text{(II.15)}$$

Where m is the strain rate exponent, $\sigma\big|_{\varepsilon_1,\,\dot{\varepsilon}_1}$ is the stress at ε_1 and $\dot{\varepsilon}_1$, $\sigma\big|_{\varepsilon_1,\,\dot{\varepsilon}_2}$ is the stress at ε_1 and $\dot{\varepsilon}_2$, $\dot{\varepsilon}_1\big|_{\varepsilon_1}$ is $\dot{\varepsilon}_1$ at ε_1, and $\dot{\varepsilon}_2\big|_{\varepsilon_1}$ is $\dot{\varepsilon}_2$ at ε_1.

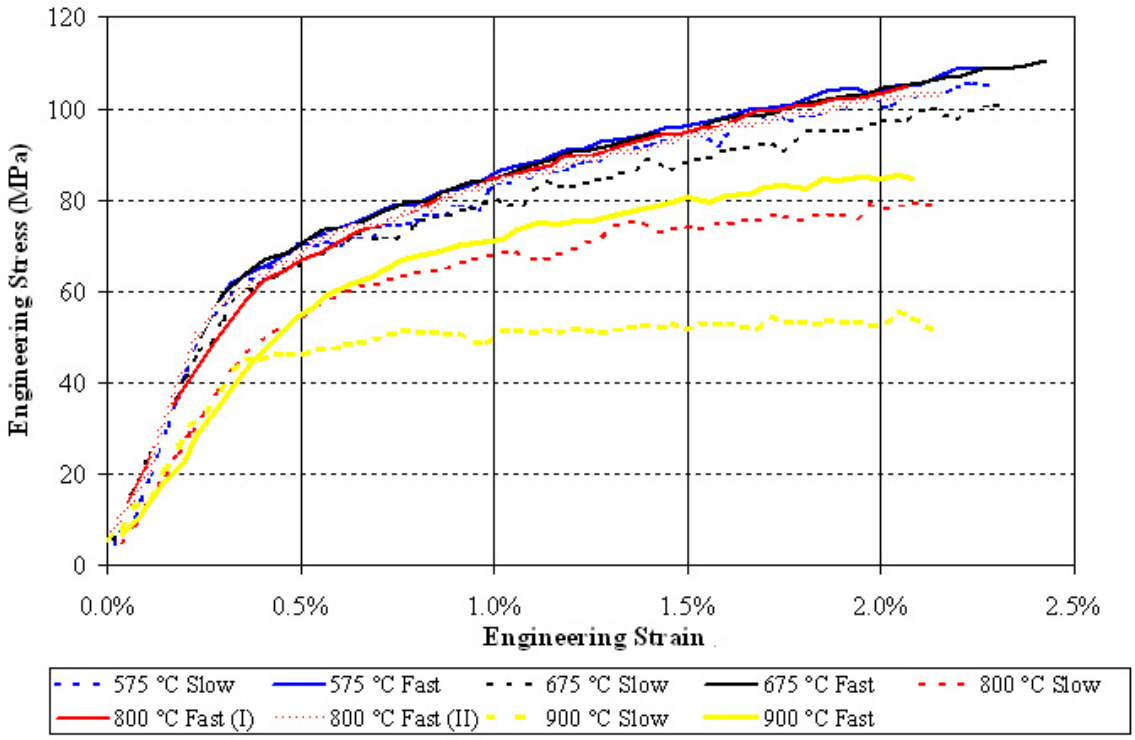

Figure II.29: High temperature uniaxial tension tests performed at 10^{-4} s^{-1} (slow), and 10^{-2} s^{-1} (fast). Tests were performed on Fe39Ni8Cr dog-bone samples with an initial porosity of ~15.5%.

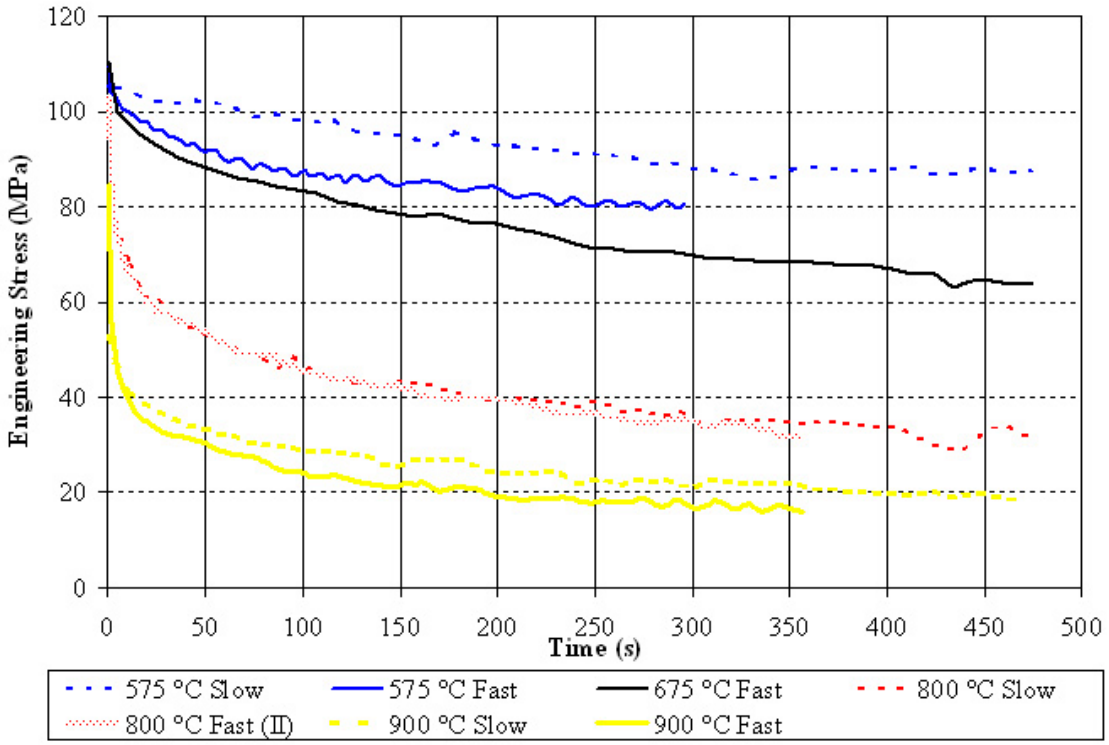

Figure II.30: High temperature relaxation tests performed at the terminal strain of the uniaxial tension experiments shown in Figure II.29. Fast and slow refer to the strain rate of the uniaxial tension experiment prior to the relaxation test, as defined in Figure II.29. Tests were performed on Fe39Ni8Cr dog-bone samples with an initial porosity of ~15.5%.

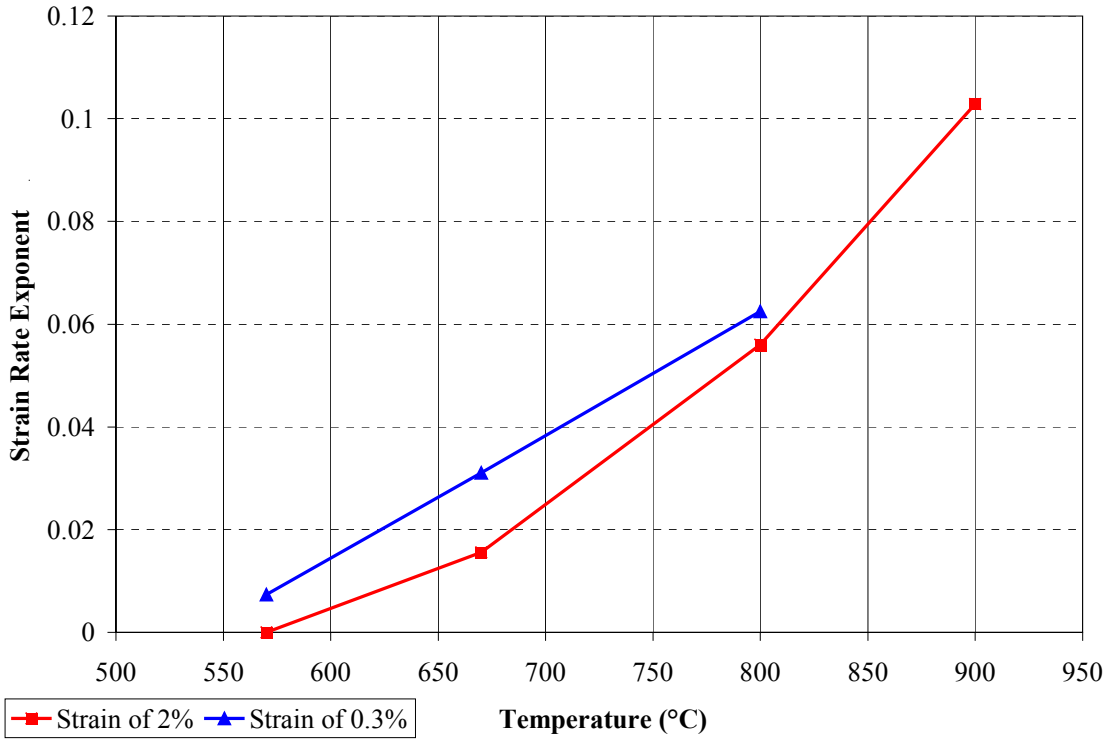

Figure II.31: Strain rate exponent at 0.3% and 2% engineering strain.

Extensometers were not used during any experiment, because of the geometry of the sample, and the difficulty in getting access to the high temperature samples. Therefore, the strain in the gauge length was estimated using the displacement values of the actuator from stroke control. The problem with such a technique is that it does not accurately give the engineering strain in the gauge length at very low strain levels. Hence, the elastic modulus from the tension measurements is artificially low. However, as discussed later, the elastic modulus for similar samples was accurately determined from ultrasonic wave speed techniques. Figure II.29 was then corrected to reflect the proper modulus by subtracting off a constant strain from the entire curve so that the elastic portion of the curve would exhibit the proper modulus, as shown in Figure II.32.

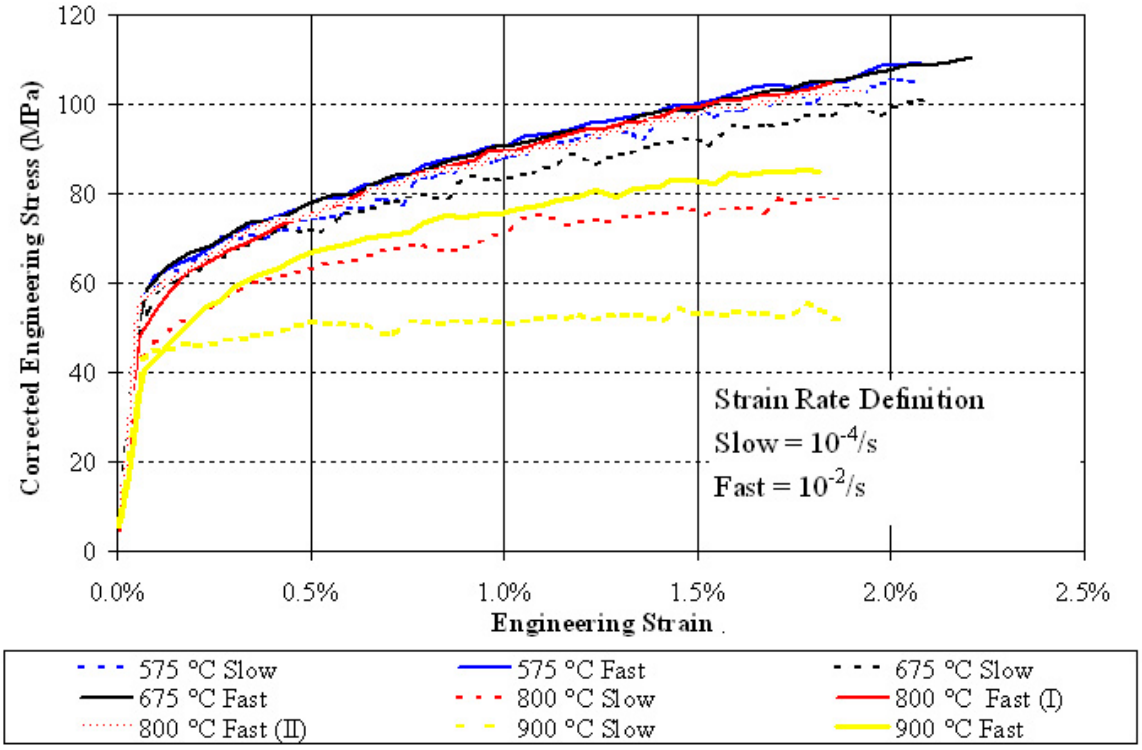

Figure II.32: Modified stress-strain curve obtained from the data in Figure 29 and a more appropriate modulus determined from ultrasonic techniques.

In addition to the uniaxial tension tests that were performed on densified Fe39Ni8Cr samples, several uniaxial compression tests were performed on the Fe39Ni8Cr system prior to the onset of sintering. Specifically, the tests were performed to give insight into the compressive rupture strength of the material, and give an approximate elastic modulus. All compression tests were performed on Fe39Ni8Cr compacts that were approximately 4.2mm thick. Compression tests were performed on the green compact, the compact after binder burnout (heated to 350 °C in a helium environment for 1.5 hours), and the compact prior to sintering but after reduction had occured (heated to 550 °C in 387 sccm Ar + 4% H_2 for 10 hours). The samples tested in the green state were 6mm long, 6mm wide and 4.2mm thick (gauge length). All the

samples that were heated were approximately 11mm wide, by 11mm long, and 4.1mm thick (gauge length) when tested. Figure II.33 shows the resulting stress-strain curves for the three different sets of experiments. Several of the experiments were repeated to ensure consistency. The stress plateau in each case was taken as the failure strength of the material. Figure II.34 shows a similar stress strain diagram for cyclic loading of the compacts. From Figure II.34 it was determined that the compacts are reasonably elastic. The elastic modulus was determined to be 0.44 GPa for the green compact, and 0.036 GPa for both the binder burnout and reduced samples.

Unpublished modulus of rupture experiments performed by K. Hurysz (Hurysz 2003) showed that the tensile rupture strength of the green compact was independent of particle size or composition, but instead a function of the fraction of binder mixed into the water during processing as shown in Table II.2. The green compacts used for this project contain 20% binder in the water. It is important to note the gross asymmetry between the 200 KPa tensile rupture strength and the 67 MPa compressive rupture strength.

Table II.2: Unpublished MOR data on ~3mm diameter cylinders in the green state with different volume fractions of binder (Hurysz 2003).

Binder Fraction in Water	20%	25%	30%
MOR	200 KPa	280 KPa	350 KPa

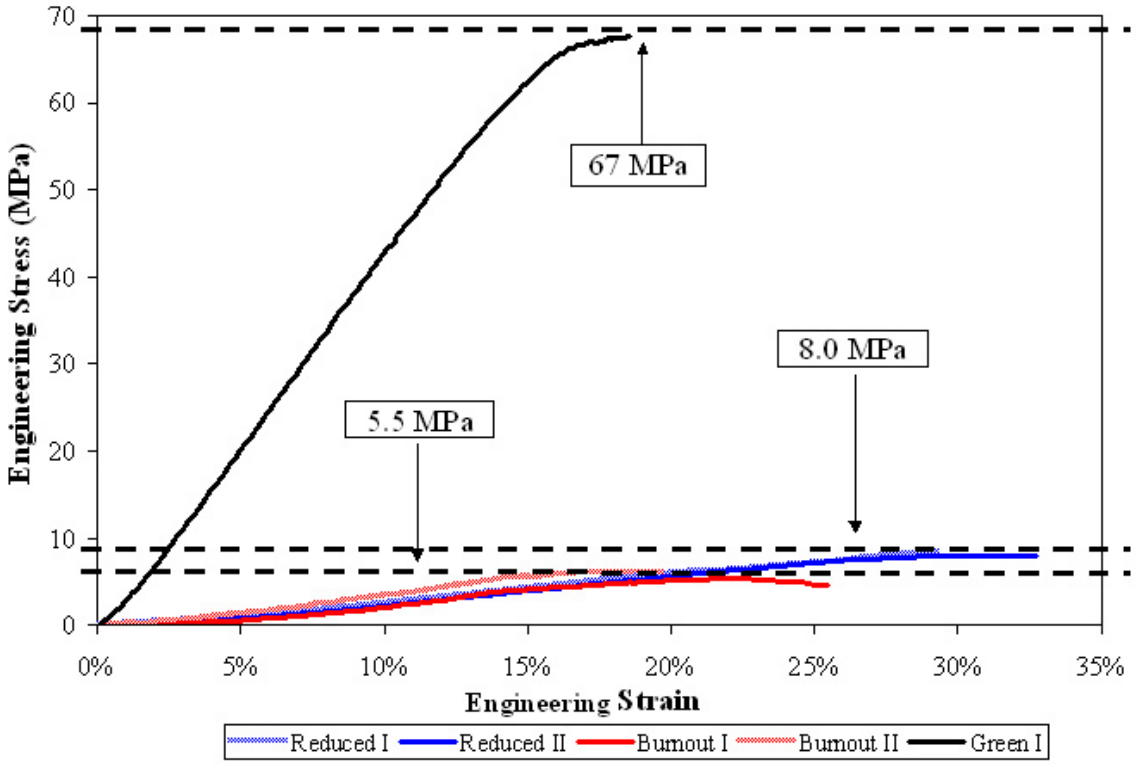

Figure II.33: Stress-strain diagram derived from compression experiments on Fe39Ni8Cr prior to sintering. Three types of samples were tested, the green compact, the compact after binder burnout, and the compact before sintering but after reduction.

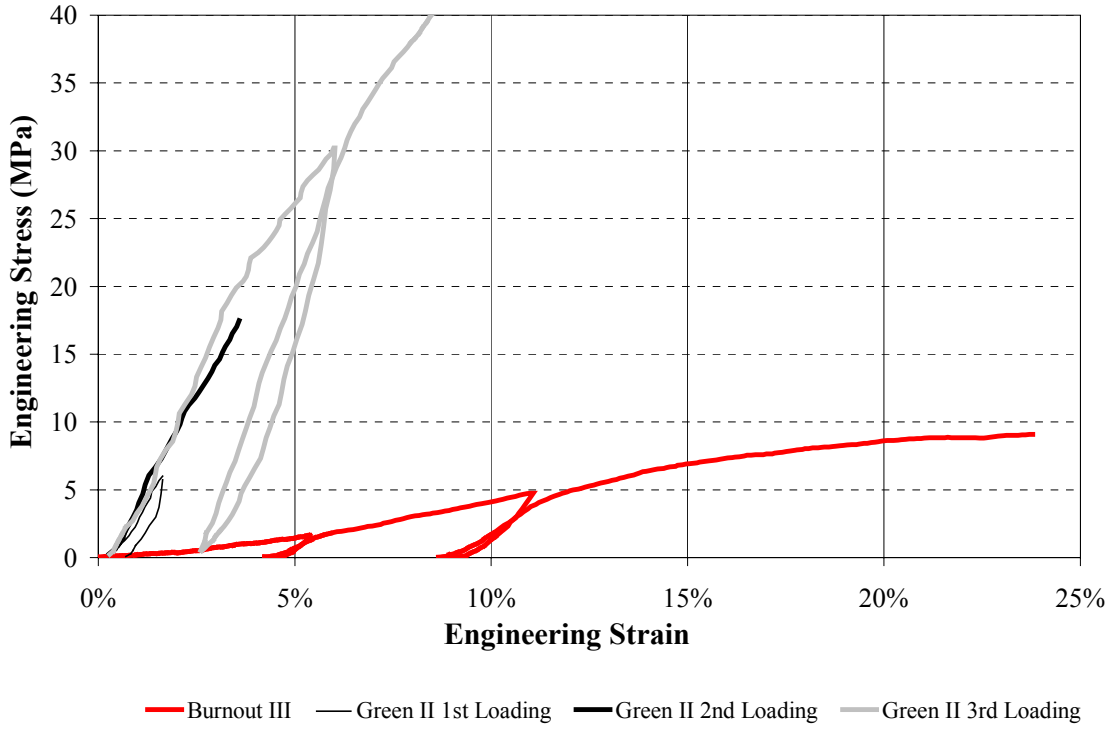

Figure II.34: Cyclic compression tests on two different types of samples to determine level of elasticity of compacts at different stages.

The elastic modulus of the Fe39Ni8Cr system was determined using an ultra sonic technique where the transverse and longitudinal wave speeds through the material was measured using a NCA1000 from Second Wave Systems. The two wave speeds are then related to the elastic modulus and Poisson's ratio of the material according to Meyers and Bhardwaj (Bhardwaj 1986; Meyers 1994).

$$E = \frac{\mu(3\lambda + 2\mu)}{\lambda + \mu}, \quad \nu = \frac{\lambda}{2(\lambda + \mu)}, \quad \mu = \left(\frac{2h}{t_{trans}}\right)^2 \rho$$
$$\lambda = \left(\frac{2h}{t_{long}}\right)^2 \rho - 2\left[\left(\frac{2h}{t_{trans}}\right)^2 \rho\right] \qquad \text{(II.16)}$$

Here, E and ν are the elastic modulus and the Poisson's ratio, respectively, of the sample being tested, λ and μ are the Lame′ constants, ρ is the actual density of the sample being tested, h is the thickness of the sample, t_{long} is transit time for the ultrasonic pulse to travel longitudinally through the sample, and t_{trans} is the transit time for the ultrasonic pulse to travel transversely through the sample. The elastic constants were tested on two Fe39Ni8Cr strip specimens that had a total porosity of 12.4 %, and had been polished to thicknesses of 2.65mm and 2.84mm, respectively. The average elastic modulus and Poisson's ratio was determined to be 105 GPa and 0.25 respectively. Correcting the modulus for porosity effects resulted in a theoretical fully densified modulus of 159 GPa using a porosity correction factor proposed by Atkinson and Selcuk. The reported modulus for fully densified Super Invar (63Fe36Ni) was 148 GPa. The difference between the literature value and the estimated value can be attributed to the difference in microstructure, error in Atkinson and Selcuk porosity correction equation, and inaccuracies in the experiment.

Rockwell B (HRB) hardness tests were performed with a digital Future Tech FR-1E machine on a 2.65 mm thick 12.4% porous Fe39Ni8Cr specimen. A total of 10 tests were performed with an average calibrated HRB of 32.1 with a standard deviation of 2.0 HRB. The reported hardness of fully densified Super Invar (63Fe36Ni) was 90 HRB.

II.5 Characterization of Reduction and Sintering Measurements

All the experiments were based on having accurate values of temperature and flow rate. All temperature measurements were performed with 12" long 0.040" diameter sheathed type T thermocouples (TC) from Omega Engineering. The output of the TC was sampled by a computer and averaged to give an average precision of +/- 0.25 C. The mass flow controller that was used was calibrated using a standard volumetric technique for each of the different gas species used in the experiments.

The temperature profile within the furnace was of characterized by inserting two thermocouples into the center of the stainless steel tube in the furnace, and then slowly pulling one TC out. One of the thermocouples was used to control the inductive heater and maintain the furnace at a 'constant' temperature. The other thermocouple was used to traverse the tube to determine the temperature distribution within the furnace. Initially the two thermocouples were located longitudinally and axially in the center of the stainless steel tube. The inductive heater was set to maintain a constant 1200 °C temperature based off of the control TC. The temperature indicated on the traversing TC was then recorded, and the TC was slid axially out of the tube in 0.25" increments, recording the temperature along the way. A total of four different experiments were performed as shown in Figure II.35. The first experiment involved sliding a new TC out along the center axis of the tube with a constant gas flow rate of 387 sccm Ar + 4% H_2. The second experiment involved sliding a new TC out along the wall with a constant gas flow rate of 387 sccm Ar + 4% H_2. The third experiment involved moving a new TC along the center axis of the tube with a constant gas flow rate of 250 sccm Ar + 4% H_2.

The final experiment involved sliding a TC with 200+ hours run time out along the center axis of the tube with a constant gas flow rate of 387 sccm Ar + 4% H_2.

The first important observation that can be made from Figure II.35 is that all the measured temperatures were below the programmed 1200 °C because of the chosen PID parameters set in the controller. Therefore, the indicated sample temperatures in all the experiments were taken from the thermocouple reading. A second important observation is that the temperature varies substantially over the length of the heated tube. For this reason, the smallest possible sample was used to perform the desired experiment. Typically, for the sintering and reduction studies, only 10 mm long samples were used, and the control TC was placed directly to the side of the specimen to ensure an accurate temperature reading. A third important observation is that the temperature in the tube does not vary much with gas flow rate. When the flow rate was cut in half, the temperature in the center of the tube did not increase significantly. Fourth, it was determined that the maximum temperature gradient across the cross-section (from tube wall to the center of the cross-section) of the tube did not exceed 3 °C when within 0.25" of the longitudinal center of the tube. Finally, it was observed that the age of the TC had a very dramatic affect on the accuracy of the TC. When a TC that had been used in the furnace for over 200+ hours, it indicated temperatures that were over 8%, or approximately 100 C lower then the two new TC's indicated at the same position with the heater controlled by the same new TC. Therefore, only new, or relatively new TC were used for important experiments. Furthermore, each experiment batch was performed on the same TC, and checked with a second TC when thought necessary. Taking all the above into account, it was estimated that the average reported temperature is probably

within approximately +/-10 °C of the actual temperature, and repeatable to within +/- 5 °C.

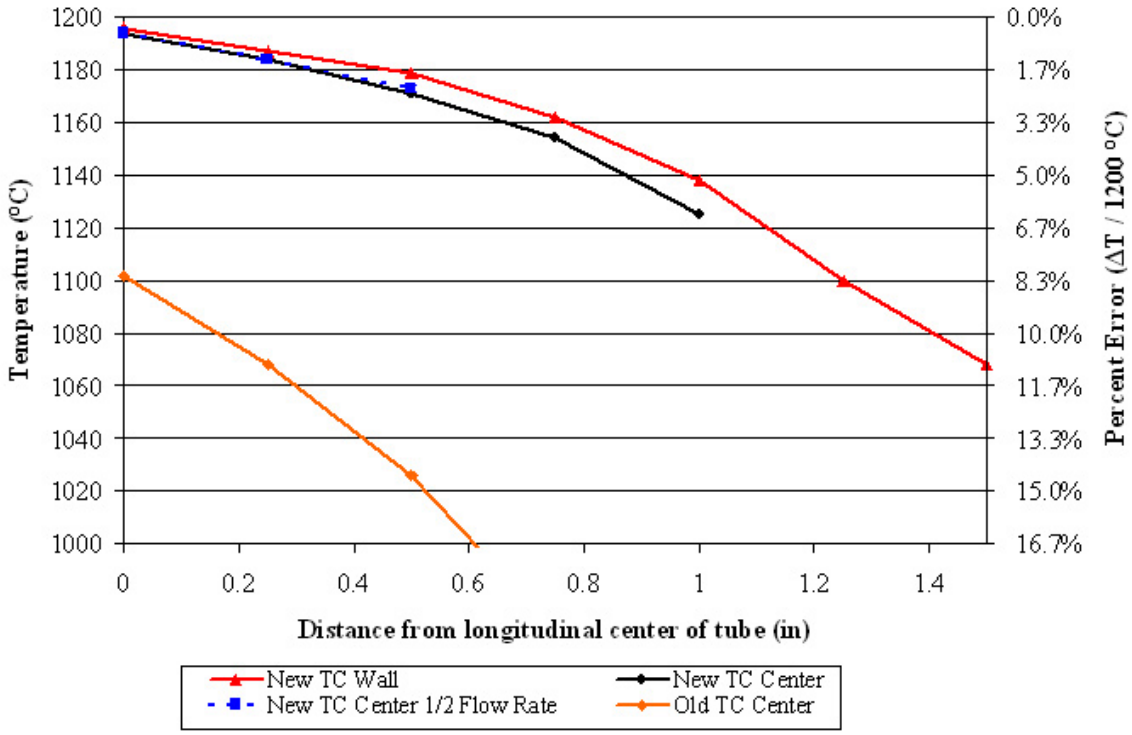

Figure II.35: Measured temperature profile in heated stainless steel tube down the length of the tube starting from the center. The position of the TC within the cross-section was changed as well as the flow rate and age of the TC.

The specifications for the Keyence LS-7030 dilatometer are shown in Figure II.36. The two most important specifications are the +/- 2µm accuracy, and the 2,400 measurements/second sampling rate when the transmitting and receiving heads are 214 mm apart. However, the actual accuracy of the dilatometer in its current configuration is less then indicated in Figure II.36, because of the 510 mm distance between the two heads, the glass furnace the light is shinning through, and the practical problems

associated with loading samples into the furnace straight. The practical accuracy of the dilatometer in its current setup was determined to be +/- 12 μm at room temperature based off of its output dimension from a cylinder of known diameter. The repeatability of the measurements was determined to be +/- 0.5 μm. Wider samples were used, and dimensional data was normalized to the initial length whenever possible to minimize the contribution of error from the dilatometer. By doing this, the contribution of error to the measured model parameters from the dilatometer was considered insignificant compared to uncertainties in temperature because the average sample was 10mm wide and underwent shrinkage to approximately 20% of its initial length.

The only major problem that was encountered using the dilatometer was its tendency to switch which edges it was tracking on samples that had a depth comparable to their width. Specifically on square samples that were aligned so their front face was almost but not quite normal to the incident light beam from the dilatometer, the dilatometer would switch from tracking the two front edges, to tracking a front edge and a back edge intermittently. Obviously this would result in large unrealistic dimensional changes in the experiment over the course of the run. Therefore all tested specimens were ground into wedges as shown in Figure II.37, to prevent the dilatometer from ever detecting the back edges (unless the sample was loaded such that it was rotated substantially off axis). During the grinding process, it was imperative to keep the two front edges parallel to each other so the dilatometer would measure the same overall dimension width as the sample shrunk.

Model	LS-7030
Measuring range	0.3 to 30mm
Minimum detectable object	0.3mm
T-to-R distance	160±40mm
Light source	GaN green LED
CCD scanning range	Approx. 33 mm
Measuring accuracy (*1)	±2μm
Repeating accuracy (*2)	±0.15μm
Sampling times (*3)	2,400 times/s
Enclosure rating (*4)	IP64
Ambient temperature	0 to +50˚C (32 to 122˚F), No freezing
Relative humidity	35% to 85% RH, No condensation
Weight	Transmitter: Approx. 420 g Emitter: Approx. 470 g Base: Approx. 430 g

*1: The measuring accuracy is checked with a 10-mm-diameter round bar moved within a measuring area of 10 x 20 mm.
*2: The repeating accuracy is checked with 10-mm-diameter round bar located in the center of the measuring area to check the outer diameter of the round bar with 512 averaging times and ±2σ set.
*3: The number of sampling times per second will be 1,200 when the mutual interference prevention function is used.
*4: The Enclosure rating is not applicable to the cable connectors.

Figure II.36: Tabulated specifications for the Keyence model LS-7030 micrometer. Table taken from Chapter 9 of the instruction manual (Keyence 2001).

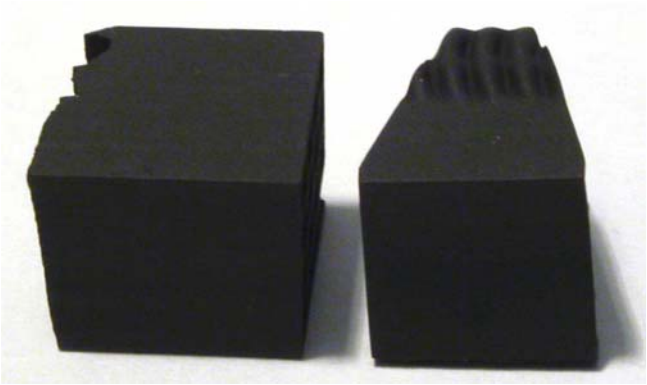

Figure II.37: Initially specimens were cut into 10mm wide square samples (left); however, interference from the trailing edges led to erroneous measurements, so the samples were ground into wedge shapes (right).

The temperature profile used to characterize the sintering of the electrolyte was standardized for reproducibility. The samples were heated to 360 °C at a 10 °C/min ramp rate, then held for 1 hour to allow for the binder to completely burn out, then ramped at 10 °C/min to 700 °C, then heated at approximately 200 °C/min to the desired hold temperature. The extremely rapid heating of the furnace was done to minimize the transient temperature affects on the sintering behavior of the monitored sample.

During sintering studies on the electrolyte, it was found that the binder could not completely burn out of the structure in dry environments. Specifically, if the sintering experiment were performed in a dry helium environment, then the final structure would be black with carbon that had diffused to the surface at high temperatures as shown in Figure II.38. The residual carbon left after incomplete binder burn retarded the sintering process and resulted in an artificial incubation period prior to the onset of sintering as shown in Figure II.39. To ensure complete binder-burnout for the electrolyte, a water bubbler was added upstream of the incoming airflow from 20 °C to 700 °C. As shown in Figure II.38, the addition of the water bubbler completely removed the residual carbon in the system and resulted in more the traditional sintering curves as shown in Chapter III. Complete binder burnout was not a problem for the metallic system, because enough water vapor was generated during reduction to sufficiently remove the binder.

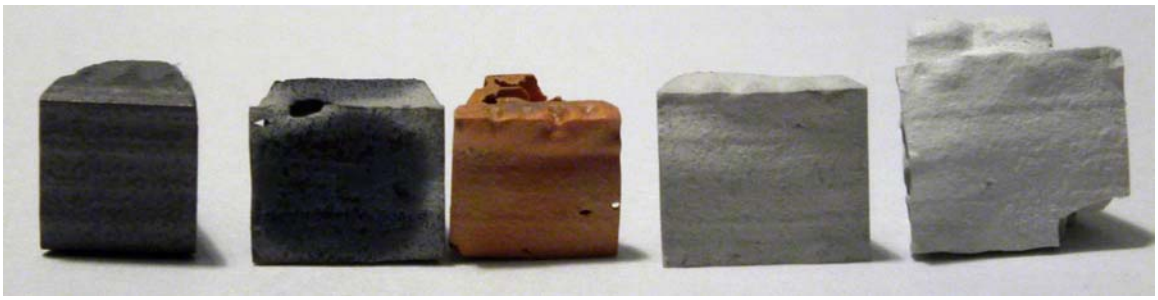

Figure II.38: Affects of water bubbler removing binder from electrolyte during firing. From left to right, YSZ without water bubbler, YSZ with water bubbler from 20 °C to 350 °C, ScSz with water bubbler from 20 °C to 700 °C, YSZ with water bubbler from 20 °C to 700 °C, YSZ with water bubbler from 20 °C to 700 °C.

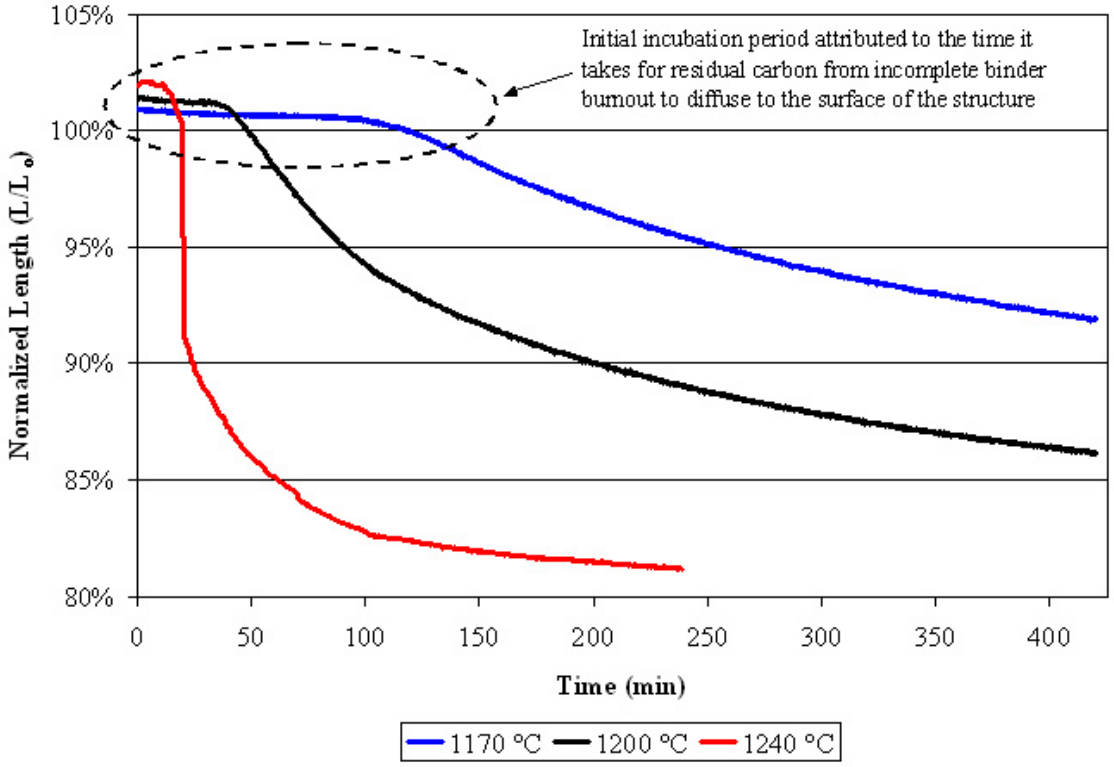

Figure II.39: The isothermal sintering behavior of the electrolyte was adversely affected by incomplete binder burnout when no moisture was present during the firing process.

The RH-62C-MV hygrometer from Omega engineering was a capacitive film type hygrometer that output 10mV per percent relative humidity from 0.0 to 100% relative humidity. The basic accuracy of the unit was reported as +/-2.5 % relative humidity. The hygrometer was plumed into the exhaust line from the furnace approximately 18 inches from the end of the furnace. With a flow rate of 387 sccm, the hygrometer was determined to lag behind the conditions in the furnace by 8 to10 minutes.

All experimental runs requiring the hygrometer were pre-flushed at room temperature for a minimum of 30 minutes with 387 sccm of dry air to equilibrate the moisture in the furnace. The runs were then held at 220 °C for 30 minutes to allow the remaining moisture in the system to reach a steady state level. Figure II.40 shows the how the humidity in the furnace decreases at room temperature under a constant gas flow after specimen insertion. Figure II.41 shows the background humidity level in the furnace during a slow (0.85 °C/min) temperature ramp after a 1 hour preflush with Ar + 4% H_2. The background humidity level is below 2% from 375 °C to 945 °C. The increase in humidity over 800 °C, is only observed when the hydrogen gas is present, and is most pronounced after insulation in the furnace is replaced. If enough high temperature long duration runs are performed back to back, the high temperature (800+ °C) humidity background decreases to almost zero. Because reduction primarily takes place between 350 °C and 800 °C, the measured humidity background was largely neglected. The increased signal noise in the hygrometer, denoted by the thicker line over 1200 °C, was caused by electrical interference from the high frequency induction heater. Specifically, the induction heater operates at high frequencies that can potentially generate electrical noise during fast ramp rates and at high temperatures. Careful routing

of wires and slower ramp rates minimize the added background. Figure II.42 shows the added noise induced by the induction heater on the hygrometer, dilatometer, and TC readout. On a side note, Helium was used as the carrier gas in the experiment shown in Figure II.42 as opposed to an Argon-Hydrogen mixture, which resulted in a much lower relative humidity background.

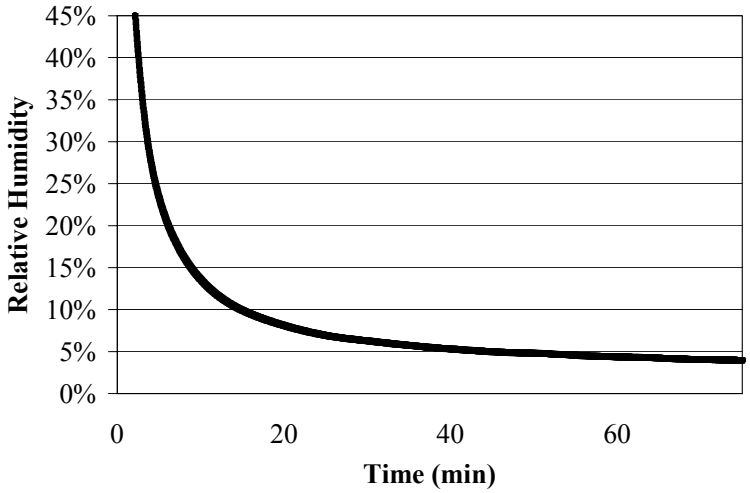

Figure II.40: Relative humidity in furnaces at room temperature after being opened up to room air with 387 sccm of Helium flushing through it.

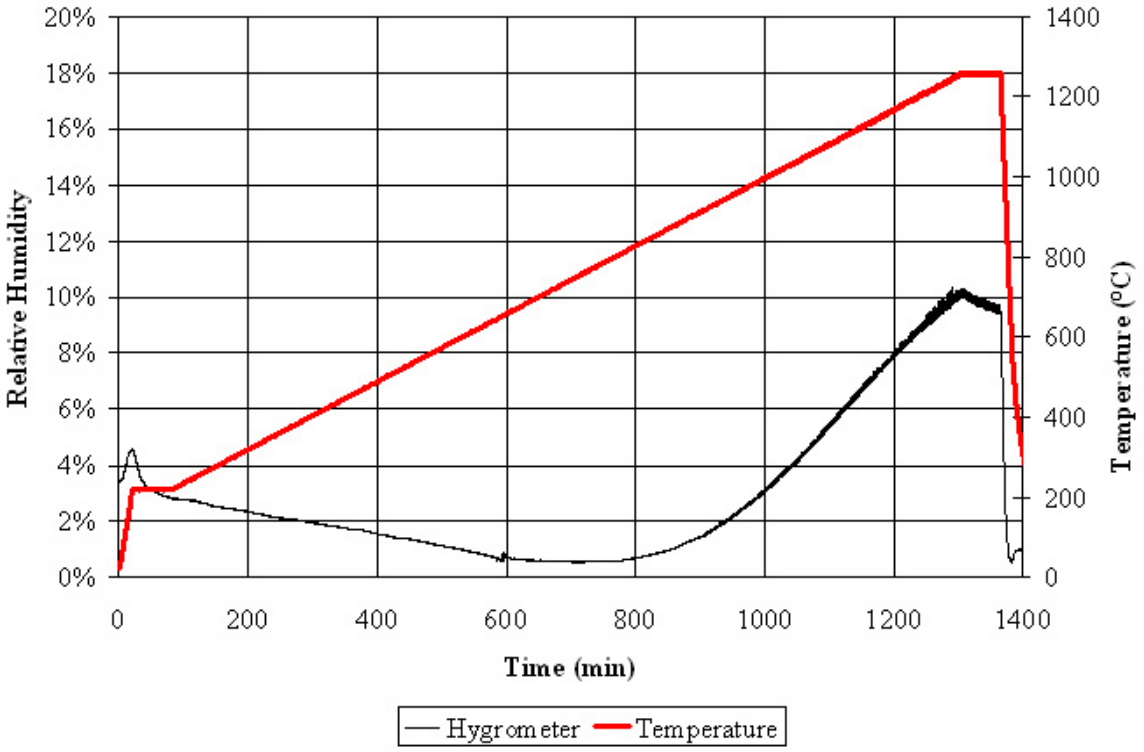

Figure II.41: Background humidity level in empty furnace with 387 sccm Ar + 4% H_2 after 1 hour pre-flush.

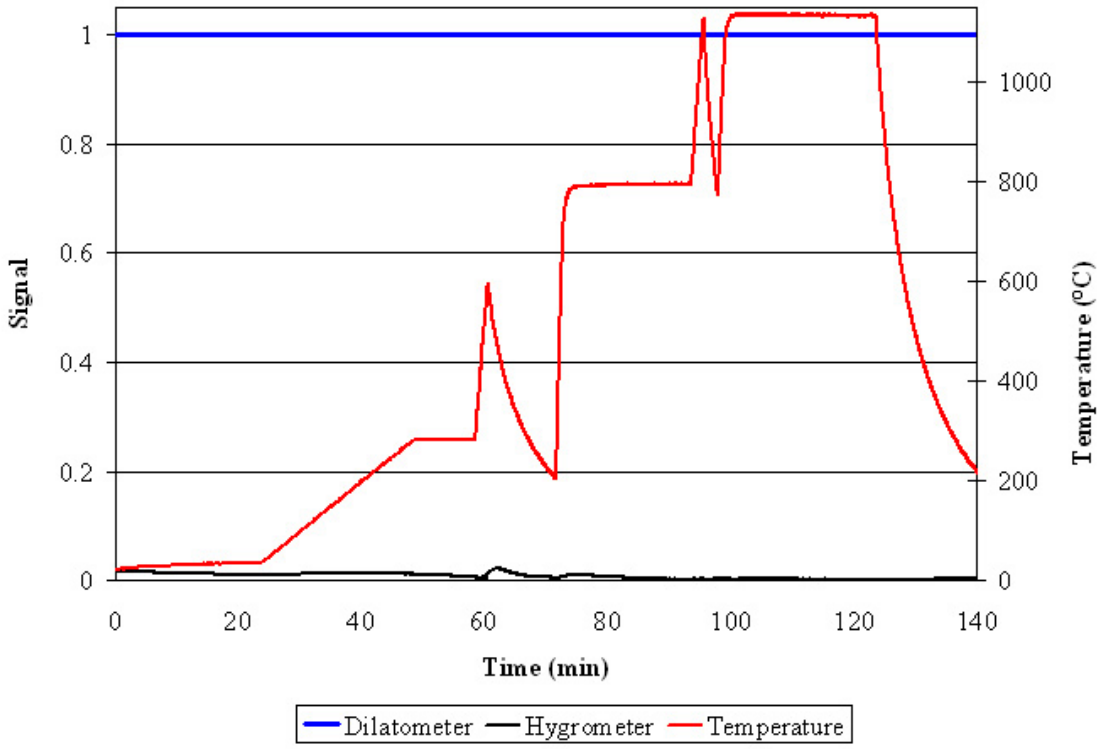

Figure II.42: Rapid heating and cooling of furnace in an attempt to quantify amount of noise induced on transducers. Flow rate of 387 sccm Helium.

Figure II.43 illustrates the validity of using the hygrometer to detect reduction. Two different nickel oxide honeycomb samples were placed in the furnace and heated from room temperature to 800 °C in 387 sccm Ar + 4% H_2 at a slow ramp rate. The measured water peak occurred at 358 °C both times, indicating the reduction temperature of nickel oxide, which was very similar to the 367 °C value reported by Mori et al. (Hiroshi Mori 2003). The difference in magnitude of the peak was caused by two different mass samples. Furthermore, it was found that firing NiO specimens in a helium environment did not result in any humidity peaks. Therefore, it was concluded that the hygrometer was an adequate tool for characterizing the reduction processes.

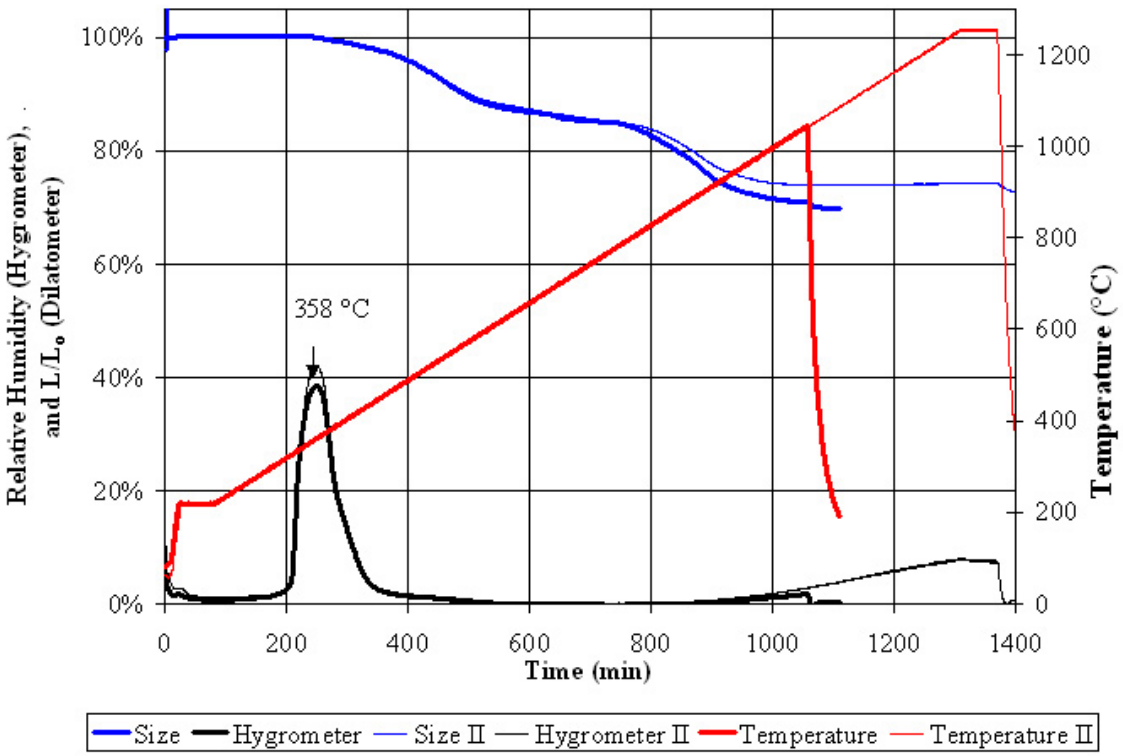

Figure II.43: Dilatometer and hygrometer output for two different NiO honeycomb structures undergoing reduction in 387 sccm Ar + 4%H_2.

CHAPTER III

THE MODEL

III.1 Fundamentals of the Model

The objective of the following model is to represent the material behavior of the electrolyte and metal interconnect over a range of realistic process conditions. The more accurate the materials and processes are represented, the more accurate the predicted internal stress evolution will be, which will allow for a more optimum process to be determined. Therefore the model needs to accurately represent mechanisms such as constrained sintering, reduction shrinkage, and thermal expansion that give rise to internal stresses, as well as relaxation mechanisms such as viscous or viscoplastic flow at high temperatures. The temperature and porosity-dependent elastic relation (McDowell 1992) was chosen as the basis for the model.

$$\{\sigma\} = \left[C(T,\varphi)\right]\{\varepsilon^e\} \tag{III.1}$$

Here $\{\sigma\}$ is the vector of stress components, [C] is the matrix of temperature (T) and porosity (φ) dependent elastic constants, and $\{\varepsilon^e\}$ is the vector of elastic strain tensor components. Unfortunately, the elastic strain cannot be directly evaluated during the manufacturing process. Therefore, without additional information, the stress cannot be determined as written either. However, information on the inelastic and thermoelastic

strain rates, such as the sintering strain rate, is known from experiments and the literature. An advantage of the hypo-elastic formulation is that strain rates can be added as

$$\dot{\varepsilon}_{ij} = \dot{\varepsilon}_{ij}^{e} + \dot{\varepsilon}_{ij}^{in} + \dot{\varepsilon}_{ij}^{th} \quad , \tag{III.2}$$

where $\dot{\varepsilon}_{ij}^{in}$ is the inelastic strain rate, $\dot{\varepsilon}_{ij}^{th}$ is the thermal expansion strain rate, and $\dot{\varepsilon}_{ij}$ is the total strain rate. The inelastic strain can be split into several terms, each term representing a different inelastic mechanism, i.e.,

$$\begin{aligned} \dot{\varepsilon}_{ij}^{e} &= \dot{\varepsilon}_{ij} - \left(\dot{\varepsilon}_{ij}^{viscous} + \dot{\varepsilon}_{ij}^{sintering}\right) - \dot{\varepsilon}_{ij}^{th} \\ \dot{\varepsilon}_{ij}^{e} &= \dot{\varepsilon}_{ij} - \left(\dot{\varepsilon}_{ij}^{vp} + \dot{\varepsilon}_{ij}^{sintering} + \dot{\varepsilon}_{ij}^{reduction}\right) - \dot{\varepsilon}_{ij}^{th} \quad , \end{aligned} \tag{III.3}$$

where $\dot{\varepsilon}_{ij}^{viscous}$ is the viscous strain rate in the electrolyte, $\dot{\varepsilon}_{ij}^{sintering}$ is the sintering strain rate, $\dot{\varepsilon}_{ij}^{vp}$ is the viscoplastic strain rate in the metal interconnect, and $\dot{\varepsilon}_{ij}^{reduction}$ is the strain rate from reduction. The elastic relationship in Equation (III.1) can be differentiated to obtain the hypo-elastic relation

$$\frac{d\{\sigma\}}{dt} = \frac{\partial[C]}{\partial\varphi}\frac{\partial\varphi}{\partial t}\{\varepsilon^{e}\} + \frac{\partial[C]}{\partial T}\frac{\partial T}{\partial t}\{\varepsilon^{e}\} + [C]\frac{d\{\varepsilon^{e}\}}{dt} \quad . \tag{III.4}$$

As isotropy is assumed for all underlying constitutive relations, the substantial derivative of $\{\sigma\}$ can be generalized on the left-hand side using the using the Jammann derivative

(Malvern 1969), if Equation (III.4) is applied to finite strains involving material rotation relations to a fixed coordinate frame.

III.2 Assumptions and Differences Between Electrolyte and Metal Interconnect Models

Before presenting detailed constitutive models for the electrolyte and metal interconnect materials, several simplifying assumptions will be addressed. Three major assumptions were made about the mechanisms that took place during the manufacturing process, and many simplifying assumptions were made about the behavior of each considered mechanism. The neglected mechanisms will be discussed in this section, while the simplifications of material behavior will be explained in each of the model sections separately. The three mechanisms that were neglected were: binder burnout, phase changes, and sliding of the electrolyte relative to the metal interconnect at the joint.

The effect of binder-burnout on the manufacturing process was neglected because of the degree of complexity associated with it compared to the observed affect it had on the manufactured structures. The binder-burnout process is primarily dependent on the temperature of the SOFC stack during the early stages of manufacturing. However, the binder burnout process itself seems to have little to no affect on the manufacturability of the specimen. Specifically, when increasing the temperature ramp rate from 0.75 °C/min to 30 °C/min on two identical monolithic compacts, which effectively increased the rate of binder-burnout, no difference in the quality of the final manufactured specimen could be observed. Furthermore, the binder-burnout process occurs at the lowest temperature,

~270 °C, and is complete before any other mechanism begins. Therefore, so long as the end state of binder-burnout is reasonably constant, it should have no effect on the other mechanisms. The consistency of the sintering and reduction behavior of the compact, independent of the manner in which the binder was removed, demonstrated this to be true. Therefore the binder-burnout process was neglected.

The expansion or contraction of either of the materials because of phase changes was neglected, because it was assumed that the process conditions would not be varied enough to cause a phase change to occur. Figures III.1 and III.2 show the phase diagrams for the given material systems. As evident from Figure III.2 and III.12, the Fe39Ni8Cr system remains in the FCC structure up to 1300 ºC. However, during heat up, the chromium does tend to oxidize around 800 ºC, and this effect is neglected. More detailed information on the oxidation and reduction of chromium in the iron system can be found in J. Nadler's dissertation (Nadler 2003). Although the YSZ and ScSz phase diagrams indicate the current system could undergo a phase change from cubic to tetragonal near 500 ºC, the kinetics for the phase change are too slow at 500 ºC to promote such a change (Nguyen 1995). Therefore both the ScSz and Fe39Ni8Cr systems are accurately assumed to remain in their initial phase.

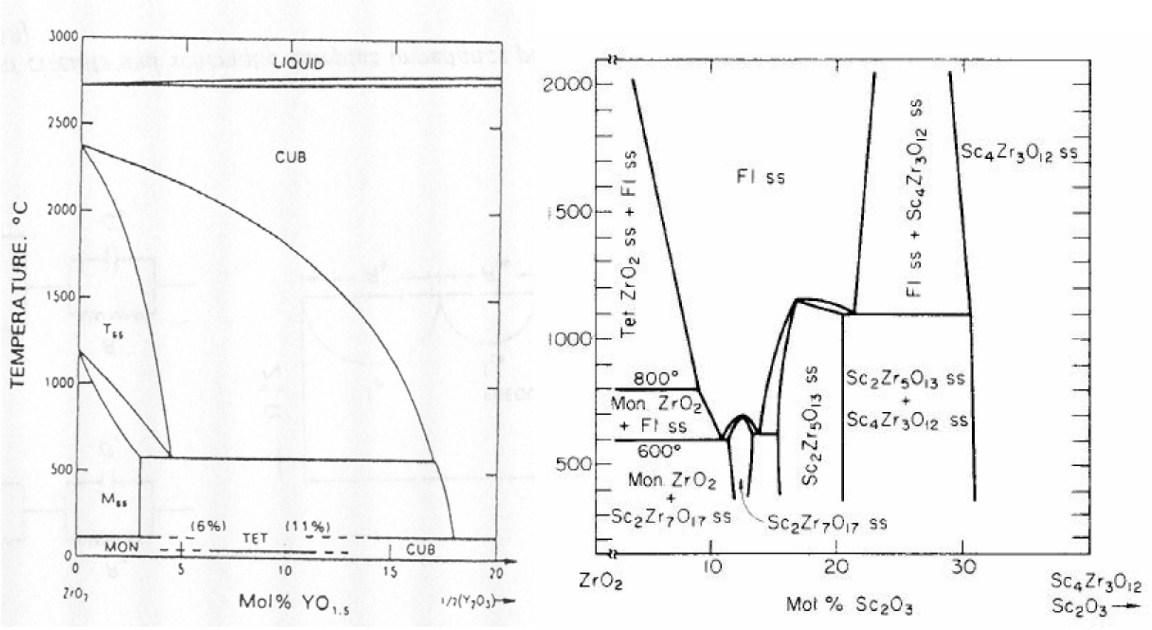

Figure III.1: Phase diagram for Yittria Stabilized Zirconia (left) and Scandia Stabilized Zirconia (Right).

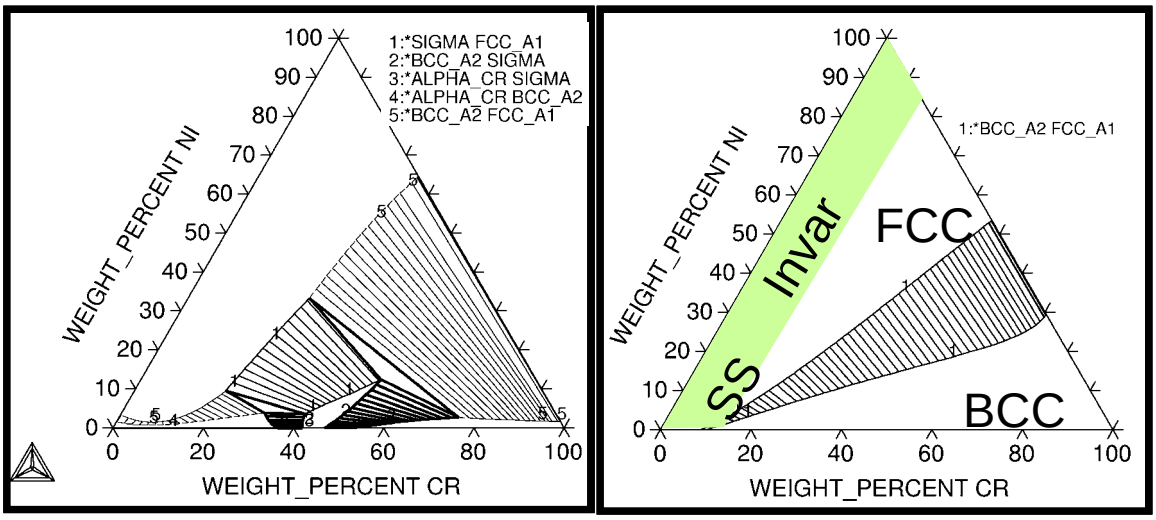

Figure III.2. Ternary diagram for Iron, Nickel, Chrome system at two different temperatures.

The model neglects the possibility of interfacial slip at the boundary where the electrolyte joins the metal interconnect, because no substantial amount of interfacial slip

was ever observed. The nature of interfacial slip is such that if it occurred during firing, it should be evident in the manufactured structure because either the electrolyte or the metal interconnect would be longer than the other. Furthermore, because sintering, reduction, and thermal expansion all involve percent shrinkages of the length of the specimen, it would be expected that if interfacial slip was occurring it would be more obvious on longer specimens. However, the electrolyte and metal interconnect are the same length in virtually all of the specimens, independent of length or firing conditions. This indicates that interfacial slip is not a substantial relaxation mechanism, and can be neglected.

Besides understanding the assumptions, it is important to understand some of the fundamental differences between the electrolyte and metal interconnect models. The ceramic electrolyte model is substantially less complex than the metal interconnect model. This can be attributed to inherent differences in behavior between the two different compacts. First of all, the shrinkage of the ceramic during manufacturing can be entirely attributed to sintering and thermal expansion. In other words, the electrolyte does not get reduced during the firing process. Secondly, with the exception of the binder-burnout, which is neglected anyway, the mass of the ceramic compact does not change during the firing process. Therefore, the evolution of porosity in the ceramic can be directly determined from the dimensional change of the ceramic. Once again, this is not true in the metal interconnect because there is a mass loss associated with reduction. Finally, the relaxation mechanisms for ceramics are much simpler then metals. Specifically, the brittle behavior of ceramics at moderate to low temperatures, $T<T_{glass}$, allow them to be treated as perfectly elastic bodies. At higher temperatures, the ceramic

starts to flow approximately in a linear viscous manner. Implementing a simple linear viscous model is reasonably straightforward. The yielding behavior of metals, however, is less straightforward because of dislocation motion and non-linear viscous, path dependent response. Therefore, a more complicated viscoplastic model is needed to explain the flow behavior of the metal interconnect.

III.3 The Electrolyte Model

The strain rate decomposition for the 12% Scandia 1.5% Ceria Stabilized Zirconia (ScSz) electrolyte is shown below. Each of the three terms accounts for a different inelastic or thermoelastic deformation mechanism, and is discussed in greater detail in the subsections to follow.

$$\dot{\varepsilon}_{ij}^{in+th} = \left(\dot{\varepsilon}_{ij}^{viscus} + \dot{\varepsilon}_{ij}^{sintering}\right) + \dot{\varepsilon}_{ij}^{th} \qquad \text{(III.5)}$$

III.3.1 Thermal Expansion

The thermal expansion coefficient is assumed to vary with temperature i.e.,

$$\dot{\varepsilon}_{ij}^{th} = \left(\alpha + \left(T - T_o\right)\frac{\partial \alpha}{\partial T}\right)\delta_{ij}\dot{T} \quad , \qquad \text{(III.6)}$$

where $\alpha \equiv \frac{1}{L_o}\left(\frac{L-L_o}{T-T_o}\right)$ for small strains, L is length, L_o is initial length, T is temperature, T_o is the reference temperature, and δ_{ij} is Kronecker's Delta $\equiv \begin{bmatrix} 1 & 0 & 0 \\ 0 & 1 & 0 \\ 0 & 0 & 1 \end{bmatrix}$. The thermal expansion of ScSz and YSZ were measured by B.Church (Church 2004) to be

$$\alpha = \left(-2.131\times10^{-18}\right)T^4 + \left(6.497\times10^{-15}\right)T^3 + \\ + \left(-7.439\times10^{-12}\right)T^2 + \left(5.389\times10^{-9}\right)T + 8.036\times10^{-6} \quad \left[\frac{m_{expansion}}{m_{length}\,°C}\right] \quad . \qquad \text{(III.7)}$$

The thermal expansion coefficient α was almost constant over the entire range of interest, so the higher order partial differential term was neglected for this model. The thermal expansion coefficient was measured and found to agree well with values reported for the same material in the literature (Y. Du 2003), and is shown in Figure III.3.

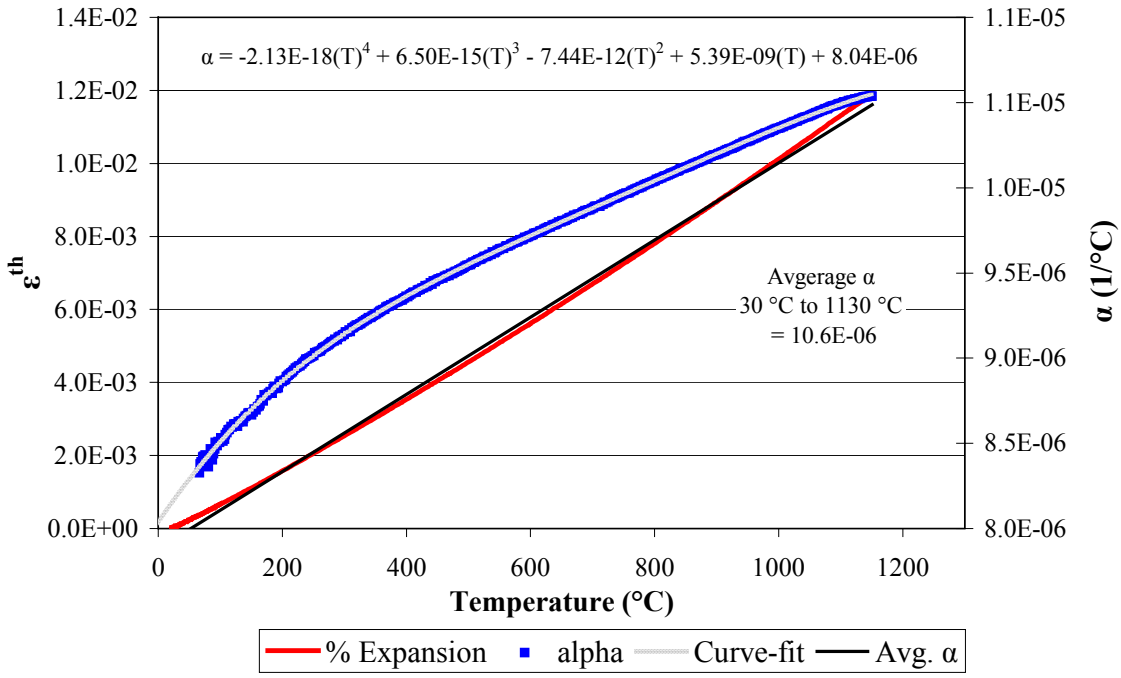

Figure III.3: Measured thermal expansion of YSZ is almost constant from room temperature to 1150 °C (Church 2004).

III.3.2 Sintering

The strain rate term that accounts for sintering is based on two models, one suggested by Hsueh (C. H. Hsueh 1986), and one suggested by Bordia (R. K. Bordia 1988a). Hsueh's model gives a formulation for the densification of an unconstrained powder compact, while Bordia's model relates the densification of an unconstrained compact to a constrained compact. During sintering, the mass of the structure remains constant and only the volume changes; hence the densification rate $\dot{\rho}$ can be related to the strain rate $\dot{\varepsilon}_{ij}^{sintering}$, i.e.,

$$\dot{\varepsilon}_{ij}^{sintering} = -\frac{\dot{\rho}}{3\rho}\delta_{ij}, \quad \dot{\varepsilon}_{kk}^{sintering} = -\frac{\dot{\rho}}{\rho} = \frac{\dot{V}}{V} \quad , \tag{III.8}$$

where $\dot{\rho}$ is the densification rate, ρ is the density, δ_{ij} is Kronecker's Delta, $\dot{V}$ is the rate of volume change, and V is the volume. The derivation of Hsueh's unconstrained densification rate is presented in the Appendix. In short, the derivation is a micro mechanical approach that takes particle curvature, surface tension and the resulting sintering potential, and grain growth into account. The final formulation of densification, which includes an empirical grain growth law, is given by (C. H. Hsueh 1986)

$$\rho_{stress\_free} = \rho_f + \rho_f\left(\rho_0 \big/ \rho_f - 1\right)\left(1 + \frac{t}{\tau(T)}\right)^{-\beta(T)} \quad , \tag{III.9}$$

where t is the time elapsed since the onset of sintering, $\beta(T)$ is a temperature dependent fitting parameter, $\tau = \tau_0 \exp\left(\frac{Q}{RT}\right)$, where τ is a coupled measure of grain growth kinetics and grain size, τ_o is a fitting parameter, Q is the activation energy for grain growth ~90 kcal/mol for ScSz, R is 0.001987 cal/(mol K), ρ_o is the initial density in green state ~2.3g/cc, ρ_f is the theoretical solid density ~6g/cc. Bordia (R. K. Bordia 1988a) then proposed a relationship between unconstrained, or free, densification rate and constrained densification rate as

$$\dot{\rho}_{stressed} = \dot{\rho}_{stress\_free}\left(1 - \frac{\sigma_m}{\Sigma}\right) \quad , \tag{III.10}$$

where, $\dot{\rho}_{stressed}$ is the constrained or unconstrained time derivative of density, $\dot{\rho}_{stress\_free}$ is the time derivative of Equation (III.9), σ_m is the hydrostatic stress or $(\sigma_{11} + \sigma_{22} + \sigma_{33})/3$, Σ is the net stress free driving force for sintering (sintering potential) defined as $\Sigma = 3K_p\dot{\varepsilon}^{sintering}_{stress\_free}$, K_p is the porous bulk viscosity of the compact (see section III.3.3), and $\dot{\varepsilon}^{sintering}_{stress\_free}$ is the stress free sintering strain given as $-\frac{\dot{\rho}_{stress\_free}}{3\rho_{stress\_free}}$. Additional models for the evolution of the sintering potential (Σ) with densification can be found in work done by L. Chandra et al. (L. Chandra 1997). The unconstrained densification rate was arrived at by differentiating Equation (III.9).

$$\dot{\rho}_{stress\_free} = (\rho_f - \rho_0)\left(1 + \frac{t}{\tau}\right)^{-\beta}\left[d\beta \ln\left(1 + \frac{t}{\tau}\right) + \beta\left(\frac{1}{\tau} - \frac{t\,d\tau}{\tau^2}\right)\Big/\left(1 + \frac{t}{\tau}\right)\right] \qquad \text{(III.11)}$$

Where $d\beta$ is short for $\frac{d\beta(T)}{dT}\frac{dT}{dt}$, and $d\tau$ is short for $\frac{d\tau(T)}{dT}\frac{dT}{dt}$, and both β and τ are temperature dependent fitting parameters. Equation (III.11) was then rewritten implicitly in terms of density for improved integration stability, by solving Equation (III.9) for time, and substituting it back into Equation (III.11). The implicit unconstrained densification rate is given by

$$\dot{\rho}_{stress\_free} = (\rho_f - \rho)\left\{d\beta\frac{dT}{dt}\ln\left(\frac{(\rho_f - \rho_0)^{\frac{1}{\beta}}}{(\rho_f - \rho)^{\frac{1}{\beta}}}\right) + \frac{\beta}{\tau}\left[\frac{(\rho_f - \rho_0)^{-\frac{1}{\beta}}}{(\rho_f - \rho)^{-\frac{1}{\beta}}} - (d\tau) + \frac{(\rho_f - \rho_0)^{-\frac{1}{\beta}}}{(\rho_f - \rho)^{-\frac{1}{\beta}}}(d\tau)\right]\right\}$$

(III.12)

where $d\beta$ is short for $\frac{d\beta(T)}{dT}\frac{dT}{dt}$, and $d\tau$ is short for $\frac{d\tau(T)}{dT}\frac{dT}{dt}$, and both β and τ are temperature dependent fitting parameters. For temperature independent parameters (β and τ), the above equations reduce to the form (C. H. Hsueh 1986).

$$\dot{\rho}_{stress\_free} = \frac{\beta}{\tau}\left[\frac{(\rho_f - \rho)^{\left(1+\frac{1}{\beta}\right)}}{(\rho_f - \rho_0)^{\frac{1}{\beta}}}\right] . \qquad \text{(III.13)}$$

The β and τ parameters were determined by fitting Equation (III.13) to the measured dimensional shrinkage of a sintering compact at a constant temperature. Values of β and τ were chosen that minimized the least squares error between Equation (III.13) and the measured densification rate. Figure III.4 shows the measured isothermal densification at different temperatures plotted against the densification predicted by Equation (III.13) using values of β and τ that gave the least squares error. The resulting values of β and τ at different temperatures can be seen in Figure III.5. Equation (III.14) is a curve fit to the experimental β and τ data, and gives values of β and τ at various temperatures. As indicated in Figure III.5, the parameters cannot be assumed to be constant below ~1250 °C.

$$\beta = 0.144 + 0.06\arctan\left(\frac{T\text{-}1133}{25}\right), \quad \frac{d\beta}{dT} = \frac{0.0024}{1+\left(\frac{T-1133}{25}\right)^2}$$
$$\tau = 2\times10^{-13}e^{\left(\frac{90}{0.001987(T+273)}\right)}, \quad \frac{d\tau}{dT} = -2\times10^{-13}e^{\left(\frac{90}{0.00199(T+273)}\right)}\left(\frac{90}{0.00199(T+273)^2}\right) \qquad \text{(III.14)}$$

Where T is the temperature in Celsius, β is dimensionless, and τ has units of minutes.

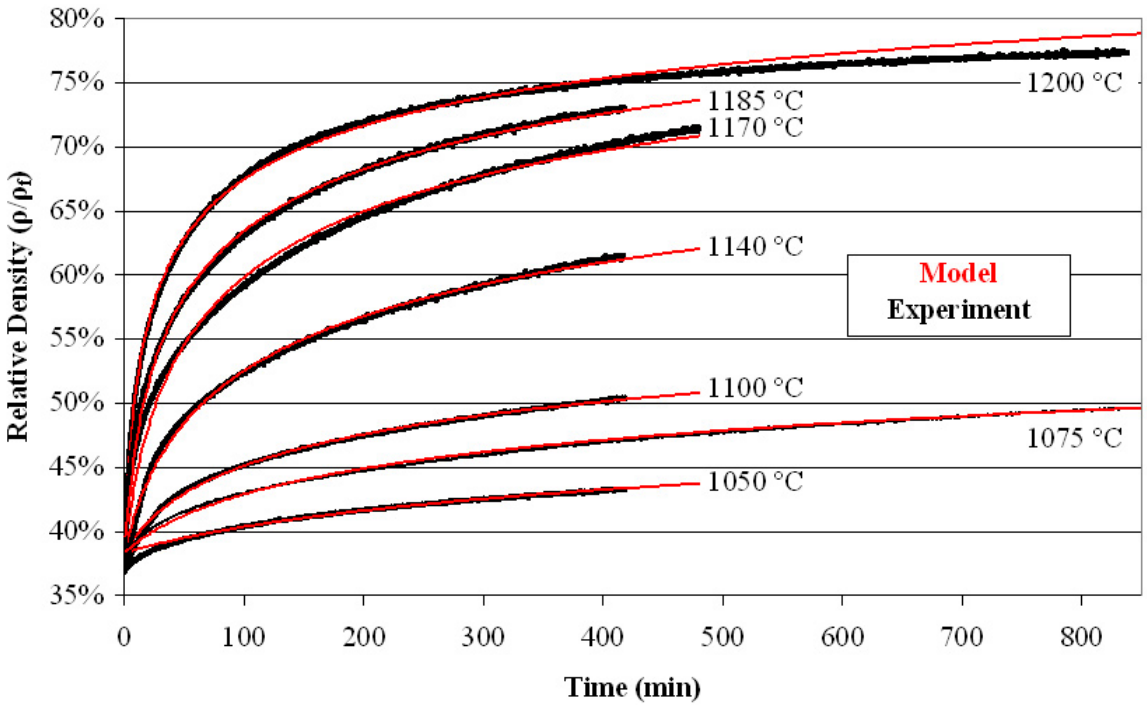

Figure III.4: Measured isothermal densification of ScSz compared to model prediction after performing a least squares fit on model parameters. Experiments performed on honeycomb samples in 387 sccm Ar + 4% H_2.

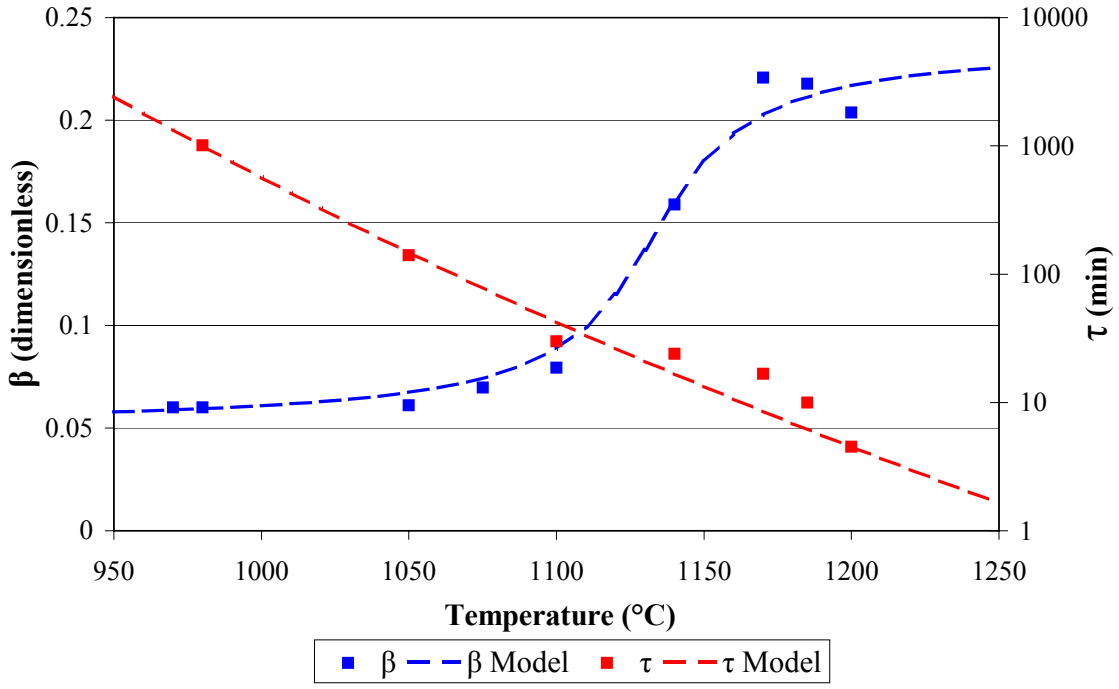

Figure III.5: Temperature dependence of β and τ parameters from experimental results.

The accuracy of the free sintering model was evaluated by integrating the stress-free densification rate equation for a given temperature history, and then comparing the results to the measured stress free densification rate for the same temperature history. To ensure a fair comparison, the temperature history was chosen such that it was completely independent of any measurements that were used to fit parameters. Figure III.6 and III.7 show the comparison for two different temperature ramping schedules. The model is in much better agreement with the experiments for the more realistic temperature profile shown in Figure III.6. The reason for the greater discrepancy between the model and experiment for the extremely slow temperature ramp rate shown in Figure III.7 is that there is greater uncertainty in measurements of the low temperature parameters. Specifically, the small dimensional changes that occurred at lower temperatures resulted

in greater error in the dilatometer measurements, and therefore more error in the β and τ parameters.

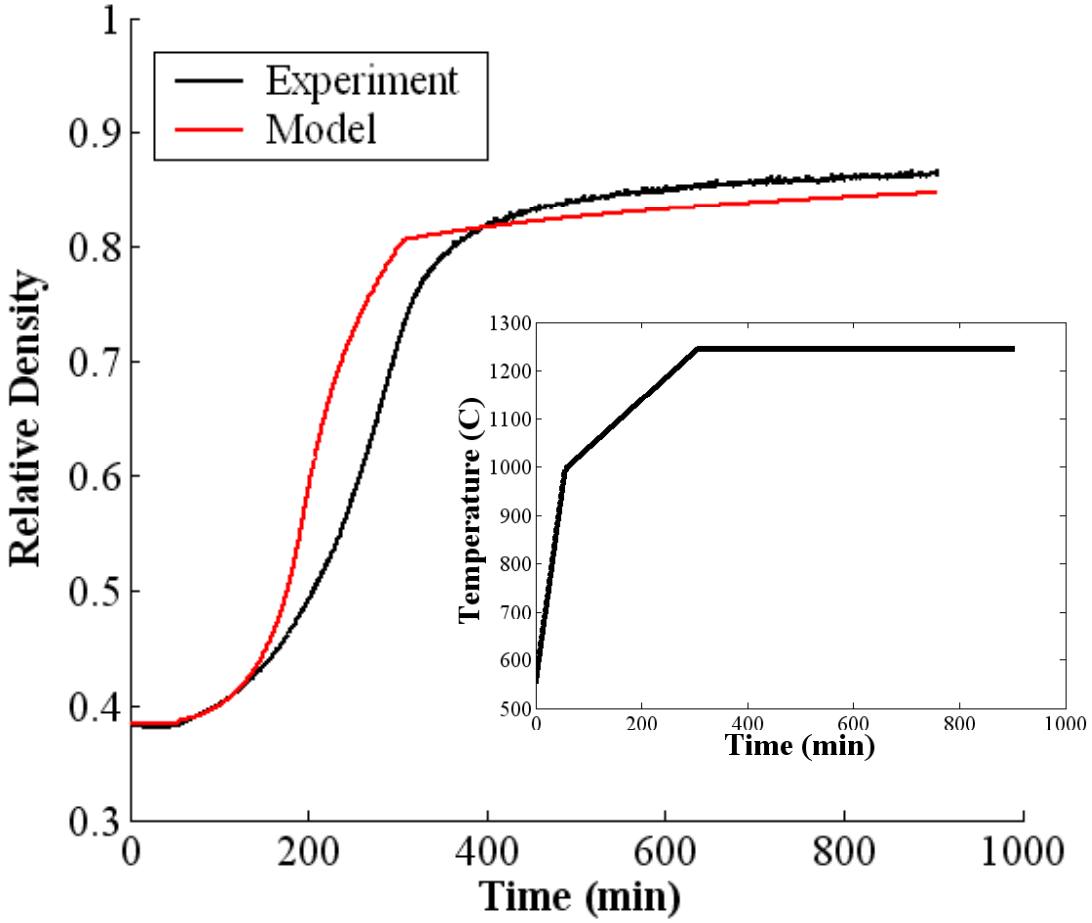

Figure III.6: Comparison of predicted stress free densification and measured stress free densification using a 'realistic' temperature profile on honeycomb sample in 387 sccm Ar + 4%H_2.

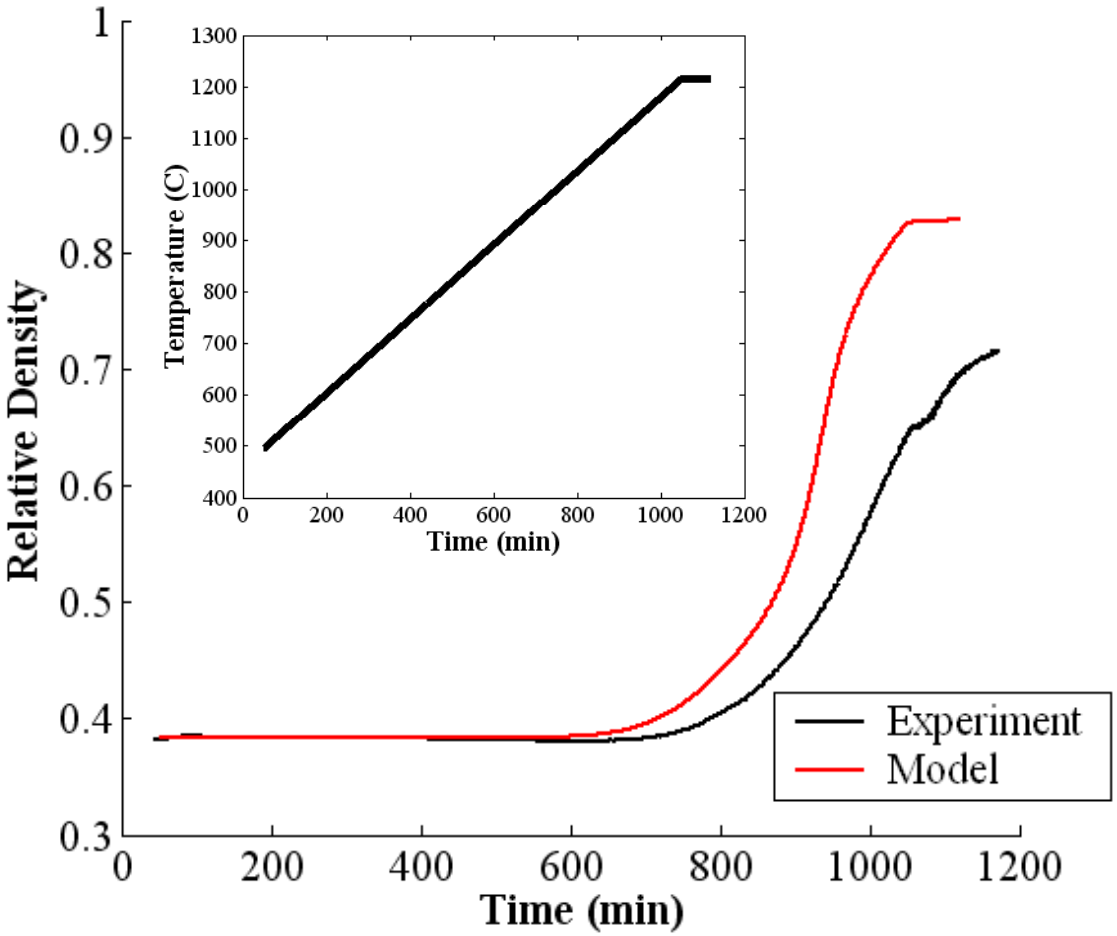

Figure III.7: Comparison of predicted stress free densification and measured stress free densification using an unusually slow temperature profile, which exacerbates the error in measured low temperature parameters. Experiments performed on honeycomb sample in 387 sccm Ar + 4%H_2.

III.3.3 Viscous Behavior

The strain rate term that accounts for the viscous relaxation of the material at high temperatures was adopted from Bordia and Scherer (R. K. Bordia 1988a). Bordia and Scherer developed constitutive models for the shear and bulk viscosity of a viscous material assuming linear viscous behavior, i.e.,

$$\dot{\varepsilon}_{ij}^{v} = \frac{s_{ij}}{2G_p} + \frac{\sigma_m}{K_p}\delta_{ij} \quad , \tag{III.15}$$

where, S_{ij} is the deviatoric stress defined as $\sigma_{ij} - 1/3\sigma_{kk}\delta_{ij}$, σ_{ij} is the stress tensor, δ_{ij} is the Kronecker's Delta, σ_m is the hydrostatic stress defined as $(\sigma_{11} + \sigma_{22} + \sigma_{33})/3$, G_p is the shear viscosity of the porous body, and K_p is bulk viscosity of the porous body. The shear and bulk viscosities can then be expressed as shown in Equation (III.16) for any porous isotropic viscous material that is linear in the sense required by Equation (III.15).

$$K_p = \frac{E_p}{3\left(1 - 2\nu_p\right)}, \quad G_p = \frac{E_p}{2\left(1 + \nu_p\right)}, \quad \nu_p = \frac{3K_p - 2G_p}{2\left(3K_p + G_p\right)} \tag{III.16}$$

Where E_p is the uniaxial viscosity of the porous body, and ν_p is the Poisson's ratio of the porous body. The difficulty in using Sherer's model is in obtaining the uniaxial viscosity of the porous medium. The uniaxial viscosity is strongly dependent on temperature and porosity level, as well as processing aspects of the material. The uniaxial viscosity can be directly measured (K. R. Venkatachari 1986; P. Z. Cai 1997b), it can be estimated from complex models based on the micromechanics of the situation (A. Jagota 1990), or it can be obtained with macroscopic models with knowledge of the viscosity of the solid material (P. Z. Cai 1997a).

The problem with directly measuring the uniaxial viscosity is that it depends on microstructure, morphology, and prior sintering history. Therefore, a large body of experiments would need to be performed over a variety of loading conditions,

temperature ramp rates, etc to create a comprehensive empirical model. Currently, there is not enough experimental data to develop such a model.

The problem with using microscale constitutive equation to model the macroscopic uniaxial viscosity is that the equations need to capture the important mechanisms without too many simplifying assumptions. Because none of the current microscopic models use any inputs from the macroscopic material behavior, the models can deviate substantially from the actual value when used under a variety of different conditions. More simply put, the microscale models rely on the accuracy of their equations to predict viscous behavior, instead of macroscopic observations that are more valid. Finally, specialized equipment is often needed to measure the required input parameters for the microscale models.

The following macroscopic model was proposed by Scherer and Bordia (R. K. Bordia 1988b) in a comprehensive review of viscosity models

$$\nu_p \approx \frac{1}{2}\left(\frac{\bar{\rho}}{3 - 2\bar{\rho}}\right)^{\frac{1}{2}}, \quad E_p \approx \frac{3\eta\bar{\rho}}{3 - 2\bar{\rho}} \quad , \tag{III.17}$$

where, η is the shear viscosity of solid material, E_p is the uniaxial viscosity of porous material, and $\bar{\rho}$ is the relative density of the material defined as current density divided by final density. The advantage of Equation (III.17) is that it relates uniaxial viscosity to the fully dense material shear viscosity and accounts for the affects of changes in material microstructure by using the relative density as an input parameter. Once again, the problem with using Equation (III.17) is that little information exists on the linear

viscosity of Zirconia-based ceramics. Furthermore, strictly speaking, fully densified Zirconia does not obey a linear viscous law, as shown by Sudhir (B. Sudhir 2001) as well as Evans (P.E. Evans 1970). However, for the purpose of this work the linear viscous relation in Equation (III.15) is used. A model by Sacks and Tseng (M. D. Sacks 1984) was employed to account for the variation of solid shear viscosity with temperature, i.e.,

$$\eta = \eta_0 \exp\left(\frac{Q}{RT}\right) , \qquad \text{(III.18)}$$

where η_o is a fitting parameter determined to be $9x10^{-4}$ Pa-s, Q is an activation energy taken to be 100 kcal/mol for YSZ, R is the gas constant ($1.987x10^{-3}$ kcal/(mol K)), and T is the temperature in Kelvin. The activation energy was assumed to be the same as reported by Evans (P.E. Evans 1970) for steady state creep of YSZ. The η_o parameter was determined by fitting equation (III.17) and (III.18) to the uniaxial viscosity measurements made by Cai et al. (P. Z. Cai 1997b) in a constant ramp rate experiment as shown in Figure III.8. Specifically, Equations (III.17) and (III.18) require temperature and relative density as inputs to get uniaxial viscosity out. Figure III.9 and III.10 were used from Cai to get the temperature and relative density at which the plotted uniaxial viscosity was measured. The η_o parameter was then modified until the data and model were in good agreement. The modeled uniaxial viscosity curve is an even better fit to the 70% Zirconia, 30% Al_2O_3 data, which are not shown.

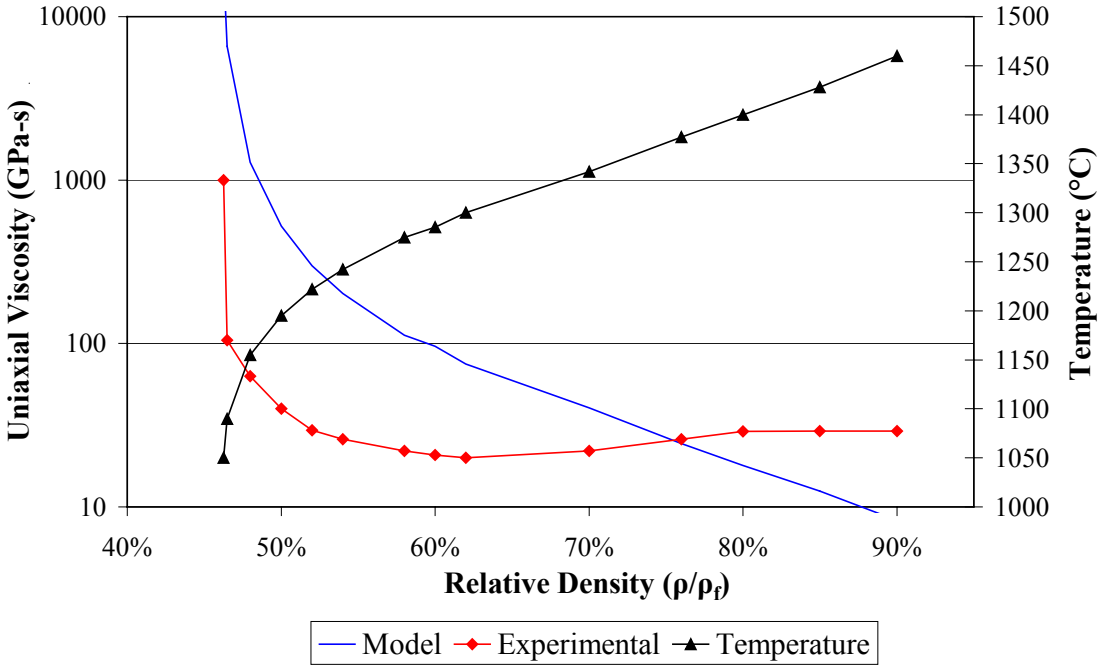

Figure III.8: Experimentally measured uniaxial viscosity versus, uniaxial viscosity predicted by the model.

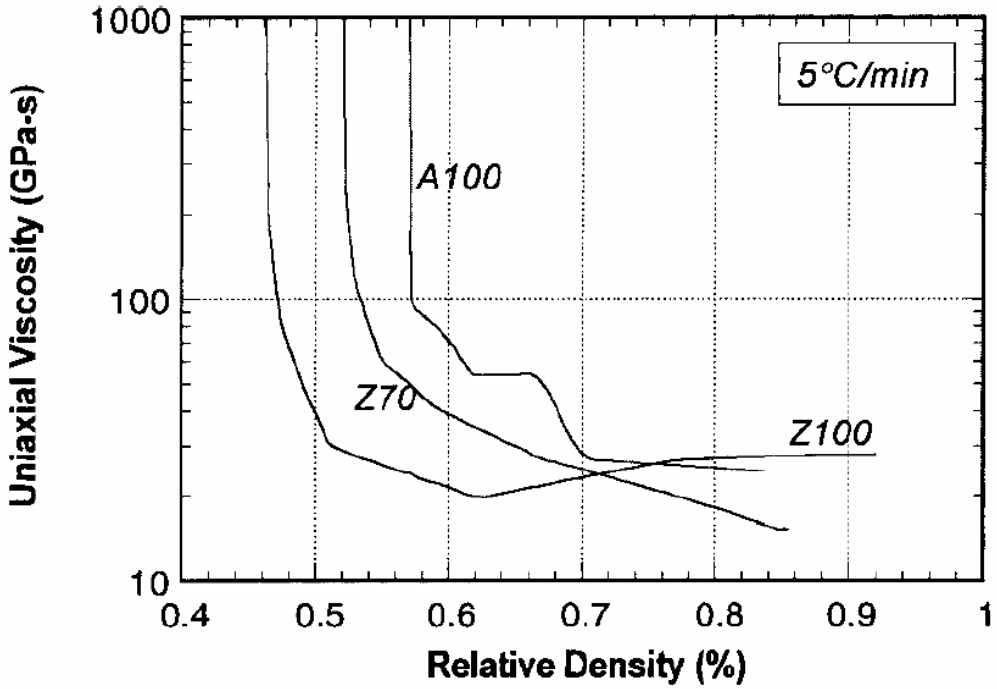

Figure III.9: Figure from Cai (P. Z. Cai 1997b), experimentally measured uniaxial viscosity of three different materials.

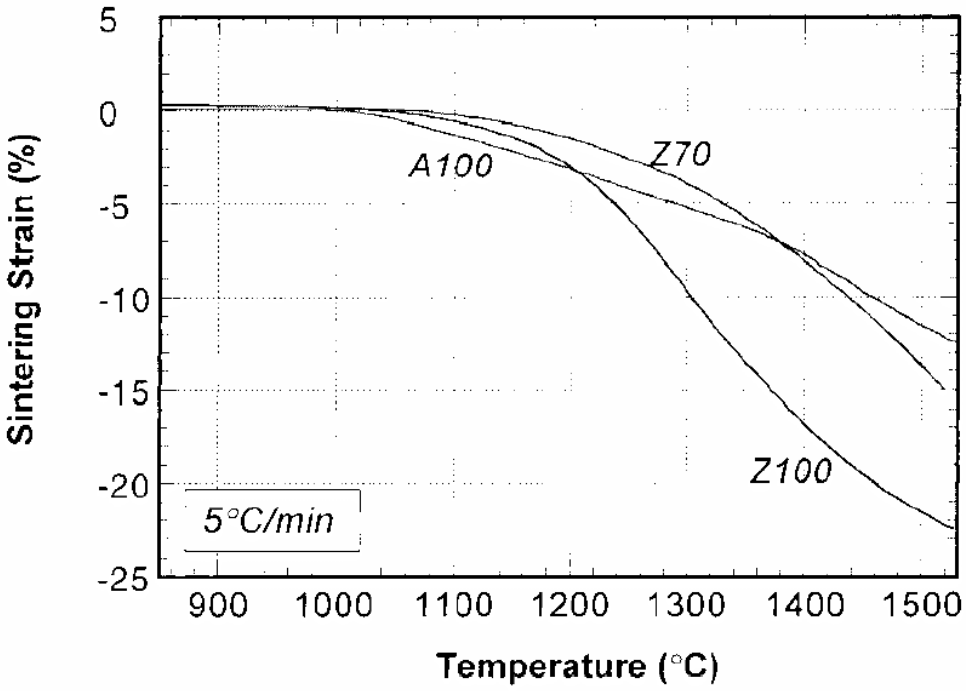

Figure III.10: Figure from Cai (P. Z. Cai 1997b), showing relationship between temperature and density.

In summary, the electrolyte is assumed to follow the linear viscous model in Equation (III.15) with porosity dependent bulk and shear viscosities given in Equation (III.16). The uniaxial viscosity which is necessary to determine the shear and bulk viscosities was determined using Equation (III.17) in conjunction with the solid shear viscosity of YSZ. The solid shear viscosity was derived by equating Equation (III.17) with Equation (III.18) and experimental data from Cai (P. Z. Cai 1997b), and Evans (P.E. Evans 1970).

III.3.4 Elastic Constants and Fracture Strengths

The model requires knowledge of the elastic constants contained within the [C] matrix in addition to the inelastic strain rate terms. The ceramic was assumed to be elastically isotropic, resulting in the matrix of coefficients

$$[C] = \frac{E(1-\nu)}{(1+\nu)(1-2\nu)}\begin{bmatrix} 1 & \frac{\nu}{(1-\nu)} & \frac{\nu}{(1-\nu)} & 0 & 0 & 0 \\ \frac{\nu}{(1-\nu)} & 1 & \frac{\nu}{(1-\nu)} & 0 & 0 & 0 \\ \frac{\nu}{(1-\nu)} & \frac{\nu}{(1-\nu)} & 1 & 0 & 0 & 0 \\ 0 & 0 & 0 & \frac{1-2\nu}{2(1-\nu)} & 0 & 0 \\ 0 & 0 & 0 & 0 & \frac{1-2\nu}{2(1-\nu)} & 0 \\ 0 & 0 & 0 & 0 & 0 & \frac{1-2\nu}{2(1-\nu)} \end{bmatrix}, \quad \text{(III.19)}$$

where E is Young's modulus, and ν is Poisson's ratio. Two different sets of elastic constants are used in the model, one prior to the onset of sintering, and one during and after sintering occurs. The elastic modulus was measured for a similar structure in the green state and after binder burnout, but before sintering. However, because only the elastic modulus was measured, the Poisson's ratio was assumed to be the same as the solid material. Equation (III.20) outlines the properties for the material before the onset of sintering. Note that the temperature and porosity dependent modulus were not directly measured. Instead they are linear interpolations between the two different modulus measurements that were made, and the onset of the porosity knockdown equation after

sintering has begun as given by Equation. The experiments that gave the elastic moduli are described in Chapter II.

$$\begin{cases} E = 0.44\ \text{GPa},\ 0 < T < 270 \\ E(T) = -0.00505T + 1.8035\text{GPa},\ 270 \le T \le 350 \\ E = 0.036\ \text{GPa},\ 350 < T < 950 \\ E(\bar{\rho}) = 205.888\bar{\rho} - 78.887\ \text{GPa},\ 0.3833 < \bar{\rho} \le 0.5,\ T > 950 \end{cases} \qquad \text{(III.20)}$$

$$\nu = 0.308,\ \ G(T,\bar{\rho}) \equiv \frac{E(T,\bar{\rho})}{2(1+\nu)},\ \ \bar{\rho} \equiv \frac{\rho}{\rho_f} = \text{relative density}$$

The material being modeled for the densified (after the onset of sintering) electrolyte is supposed to be representative of 12% Scandia stabilized Zirconia. However, due to the lack of information on Scandia-stabilized Zirconia, and the mechanical similarities between Scandia and 8% Yittria stabilized Zirconia, data for Yittria stabilized Zirconia were used when they were not available for Scandia stabilized Zirconia. The elastic constants for 8% YSZ were taken from Atkinson and Selcuk (A. Atkinson 2000), and corrected for temperature by linearly interpolating between the properties they measured at 20 °C and 800 °C, i.e.,

$$\begin{aligned} E_0(T) &= -0.04231T + 190.85\ \text{[GPa]}, \\ G_0(T) &= -0.016466T + 72.96\ \text{[GPa]} \\ \nu_0(T) &= \left(6.41\times10^{-6}\right)T + 0.3079\ \ ,T = \text{Temperature}\ (°C)\ . \end{aligned} \qquad \text{(III.21)}$$

The temperature corrected constants were then corrected for porosity by a model proposed by Atkinson and Selcuk (A. Atkinson 2000).

$$E = E_o \frac{(1 - \varphi)^2}{(1 + (2 - 3\nu_o)\varphi)}, \quad \nu = \nu_o \frac{4\nu_o + 3\varphi - 7\nu_o\varphi}{1 + 2\varphi - 3\nu_o\varphi} \tag{III.22}$$

Where E_o, ν_o are the temperature dependent elastic constants given in Equation (III.21), G is defined as $E/(2(1+\nu))$, and φ is the porosity. The model is quadratic with porosity, which is considered to be considerably more accurate at high porosity levels than alternative linear approximations. Figure III.11 shows the dependence of the Young's modulus with porosity at room temperature.

The room temperature modulus of rupture (MOR) of 8% YSZ was measured to be 123 MPa at 15% porosity on average (J. L. Clark In Press). The MOR of can be roughly estimated at other porosity levels using Equation (III.23) (Bocchini 1986), which is a knockdown equation for yield strength. The temperature affects on MOR can be seen in Table III.1 from work done by Y. Du et al (Y. Du 2003). Notice the MOR does not change substantially over 600 °C, and is approximately 75% of the MOR at room temperature.

$$\sigma = \sigma_o \exp(-4.3\varphi) \tag{III.23}$$

Where σ is the yield strength at the current porosity level, σ_o is the yield strength at zero porosity, and φ is the level of porosity in the sample.

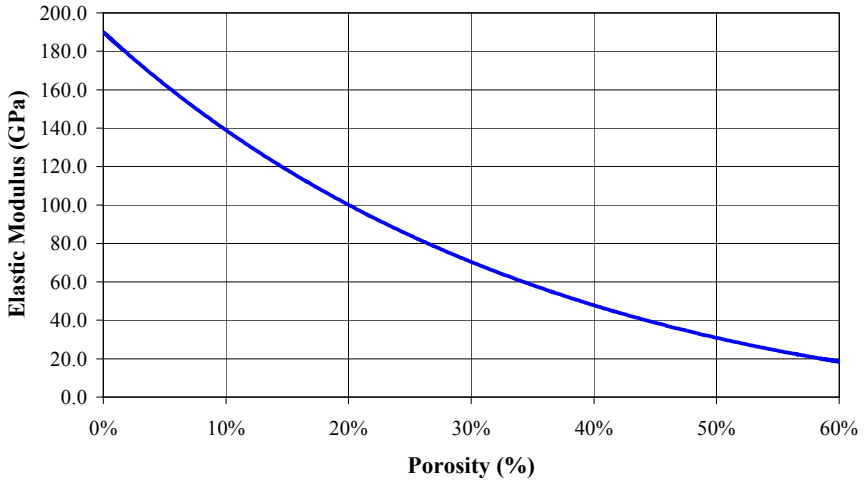

Figure III.11: Evolution of Young's modulus with porosity for 8% YSZ at room temperature, based on Atkinson and Selcuk model.

Table III.1: Reported MOR at various temperatures for 8% YSZ with less then 3% porosity (Y. Du 2003).

RT	600 °C	800 °C	1000 °C
325 MPa	230 MPa	237 MPa	245 MPa

III.4 The Metal Interconnect Model

The strain rate decomposition for the 53Fe39Ni8Cr system is shown below. Each of the terms accounts for a different mechanism, and are discussed in greater detail in the subsections to follow. The reduction term is present because the 53Fe39Ni8Cr powder compact starts as a mixture of magnetite, nickel oxide, and chromium powders that are reduced during the firing process to yield the final metal composition.

$$\dot{\varepsilon}_{ij}^{in+th} = \left(\dot{\varepsilon}_{ij}^{vp} + \dot{\varepsilon}_{ij}^{sintering} + \dot{\varepsilon}_{ij}^{reduction}\right) + \dot{\varepsilon}_{ij}^{th} \qquad \text{(III.24)}$$

III.4.1 Thermal Expansion

The strain rate term that accounts for thermal expansion is identical in form to the one used in the electrolyte model, i.e.,

$$\dot{\varepsilon}_{ij}^{th} = \left(\alpha + \left(T - T_o\right)\frac{\partial \alpha}{\partial T}\right)\delta_{ij}\dot{T} \quad , \qquad \text{(III.25)}$$

Where $\alpha \equiv \frac{1}{L_o}\left(\frac{L - L_o}{T - T_o}\right)$ for small strains, L is length, L_o is initial length, T is temperature, T_o is the reference temperature chosen to be 20 °C, and δ_{ij} is Kronecker's Delta. The thermal expansion of Fe39Ni8Cr was measured by B. Church (Church 2004), and is shown in Figure III.12.

$$\alpha(T)\left[\frac{m_{expansion}}{m_{length}\,°C}\right] = \begin{cases} \left(4.532\times10^{-9}\right)T + 6.405\times10^{-6}, & \text{for } 20 < T \le 193.95\ °C \\ \left(-1.706\times10^{-17}\right)T^4 + \left(5.755\times10^{-14}\right)T^3 - \\ \quad \left(7.843\times10^{-11}\right)T^2 + \left(5.395\times10^{-8}\right)T - 6.251\times10^{-7} \\ \text{for } T > 193.95\ °C \end{cases} \quad \text{(III.26)}$$

The thermal expansion of the metal interconnect exhibits two distinctly different behaviors, which is typical of Invar-like alloys. Therefore, the thermal expansion coefficient α was written as a piecewise function with two separate functions of temperature to account for this. Once again, an acceptable level of accuracy was obtained using only the α(T) term, and therefore the differential term was neglected.

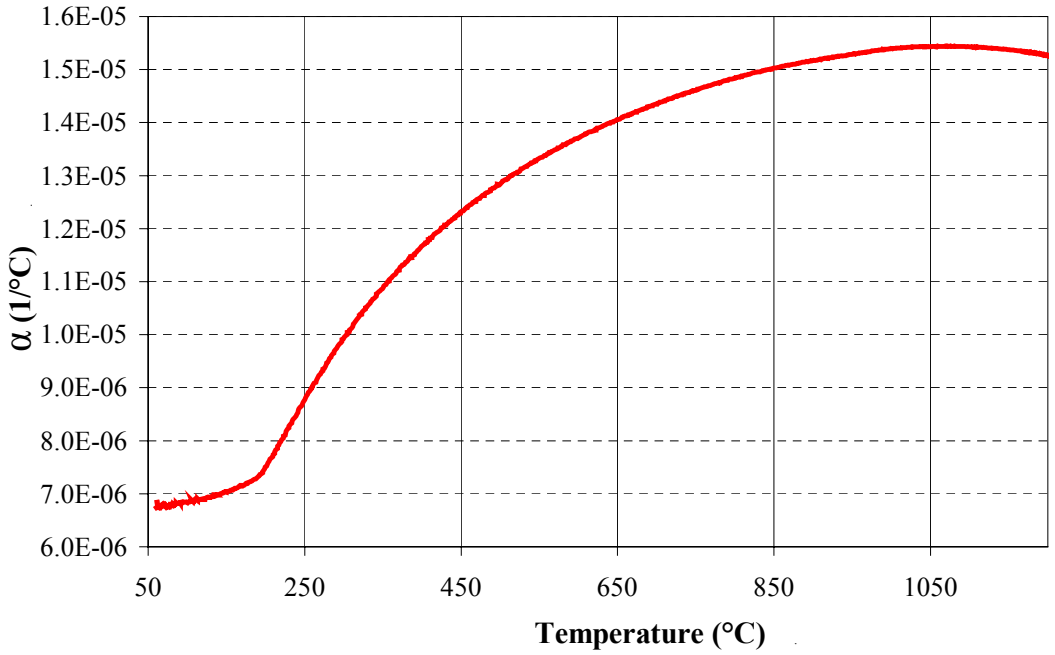

Figure III.12: Measured thermal expansion coefficient from RT to 1200 °C for the Fe39Ni8Cr system (Church 2004).

III.4.2 Reduction

The importance of the reduction model is two-fold. First, the reduction process has an associated shrinkage with it, and therefore must be represented as a stress-riser with an inelastic strain rate term. Secondly, the reduction model contains equations for the evolution of density and the mass percent of oxide reduced, both of which are very important quantities for other mechanisms modeled in the material. For the sake of clarity, only the strain-rate term will be presented in this section, and the evolution of mass loss will be covered in the next section. However, before the equations can be listed, the assumptions must first be stated.

The major assumption is that reduction is assumed to be fully decoupled from sintering, but sintering is NOT decoupled from reduction. It is assumed that reduction is complete by the time sintering densifies the structure to the point that oxygen diffusion out of the structure is substantially limited. Experimental observations suggest that this assumption is valid, and it substantially simplifies the model. A second major assumption is that the macroscopic shrinkage associated with reduction (from crystallographic rearrangement and oxygen vacancy consolidation) behaves in a similar manner to the macroscopic shrinkage of a sintering compact (from solid state diffusion). Therefore, the constitutive equations used to describe reduction were based around or derived from the sintering equations.

The inelastic strain rate term associated with reduction is strictly an empirical one for which the isotropic volumetric shrinkage is ascertained from curve fits to experimental data over the temperature range of 400 °C to 700 °C. Specifically, the optical dilatometer was used to directly measure the strain of the specimen during

reduction at a constant flow rate and several different temperatures. The measured strain data was then fit to

$$\varepsilon_{ij}^{\text{reduction, stress free}} = \left.\frac{L}{L_0}\right|_{\text{stress free}} = \frac{L_f}{L_0}\left[\left(\frac{\left(1+\frac{t}{\tau_r}\right)^{\beta_r}}{\left(1+\frac{t}{\tau_r}\right)^{\beta_r}+\left(\frac{L_f}{L_o}\right)^3-1}\right)^{1/3}\right]\delta_{ij}\ , \qquad \text{(III.27)}$$

where $\varepsilon_{ij}^{\text{reduction, stress free}}$ is the reduction strain tensor for an unconstrained system, L is the length, L_0 is the initial length at time zero, L_f is the minimum length that can be obtained solely from reduction shrinkage and is assumed to be $0.92L_0$, t is the time elapsed since the start of reduction, β_r is a temperature dependent fitting, τ_r is a temperature dependent fitting parameter, and δ_{ij} is Kronecker's Delta. Equation (III.27) was derived by rearranging the mechanism based sintering model shown in Equation (III.9). Specifically, the mass dependence of Equation (III.9) was removed by substituting in mass/volume for density and canceling out the mass terms, because the equation was developed for sintering, a constant mass process. The end result, Equation (III.27), can capture shrinkage behaviors that are analogous to those in sintering, but independent of the rate of mass loss. The β_r and τ_r parameters at different temperatures were determined by a least squares method between isothermal experimental data and Equation (III.27). Figure III.13 shows the correlation of the model shown in Equation (III.27) with the isothermal experimental data used to fit the β_r and τ_r parameters. Figure III.14 shows the evolution of the parameters β_r and τ_r with temperature. Equation (III.28) is a curve fit to

the experimental data shown in Figure III.14, and gives values of β_r and τ_r at various temperatures. The final shrinkage that a specimen could undergo from reduction was estimated from Figure III.13. Specifically, it was estimated that for all practical purposes a specimen could not shrink to less then 92% of its original length from reduction, because after 10 hours at 700 °C with the mass loss from reduction being complete for at least 5 of those hours, the reducing specimens only shrank to ~93.2% of their initial length.

$$\beta_r = -0.21 + 0.06\tan\left(0.0075T + 99.81\right),\ \frac{d\beta_r}{dT} = 0.00045\left(1+\left[\tan\left(0.0075T + 99.81\right)\right]^2\right)$$
$$\tau_r = 1171.2e^{(-0.00545T)},\ \frac{d\tau_r}{dT} = -6.383e^{(-0.00545T)},\qquad \text{for } 350 \le T \le 700 \tag{III.28}$$

Where T is temperature in Celcius, β_r is dimensionless, τ_r is in minutes.

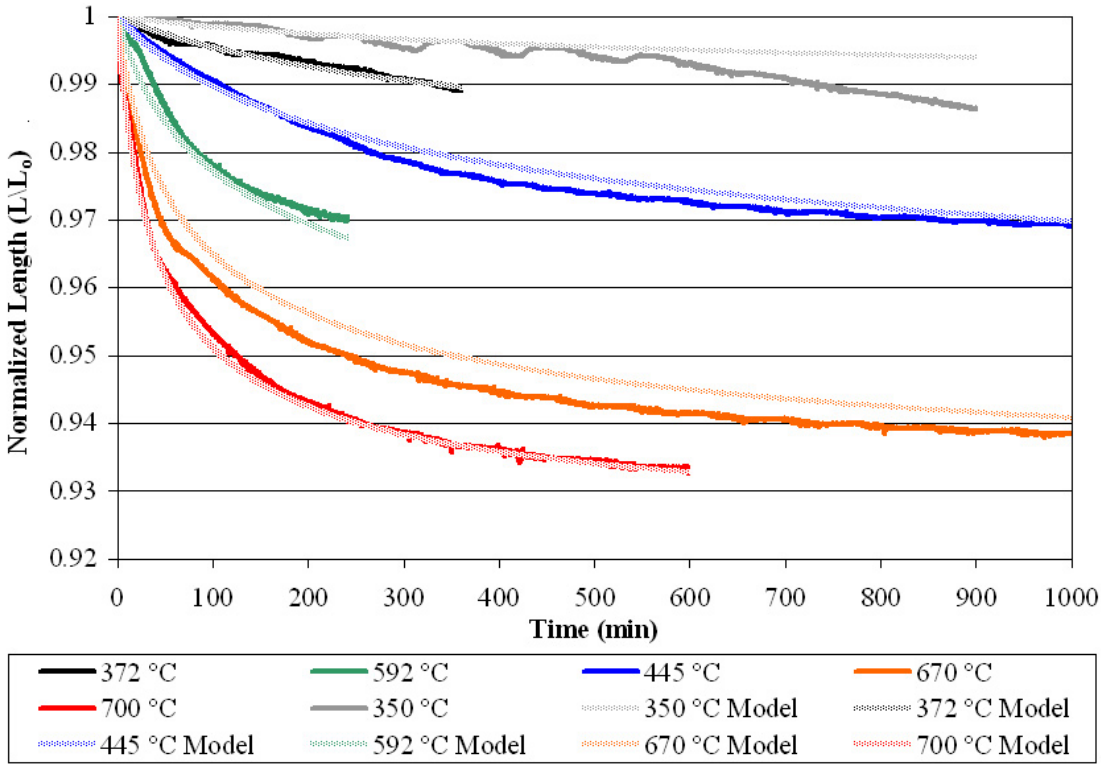

Figure III.13: Linear shrinkage of reducing honeycomb specimen at various temperatures, and the predicted shrinkage after fitting the model parameters to the data with a constant flow of 387 sccm Ar + 4% H_2.

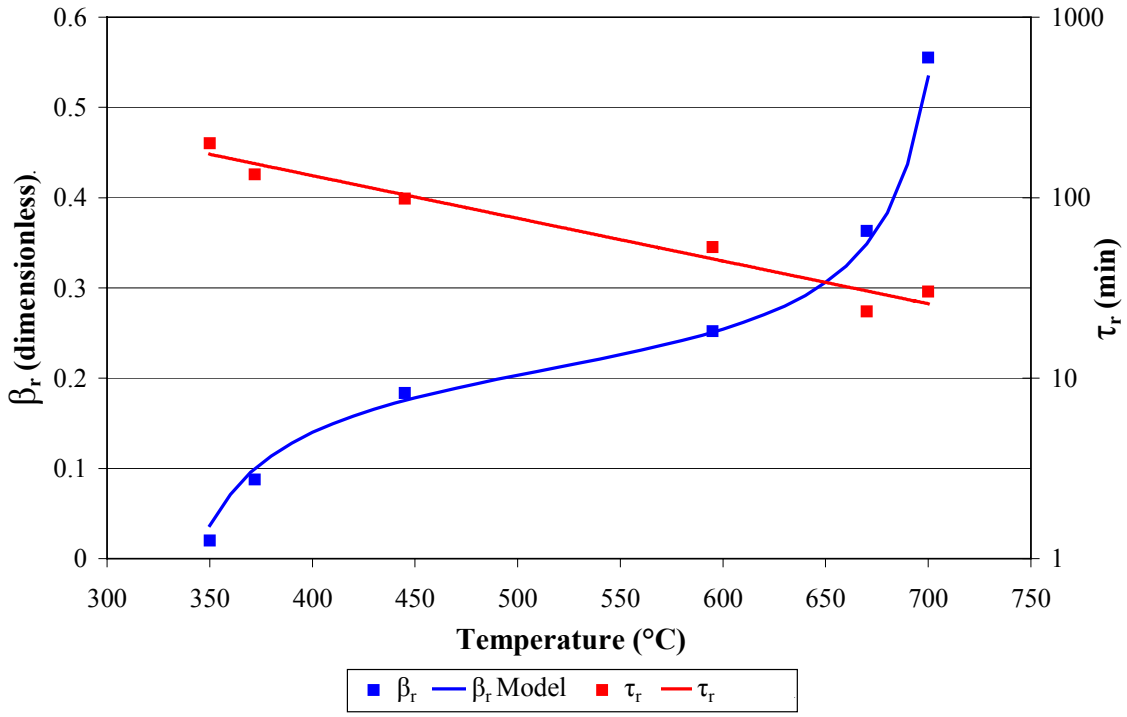

Figure III.14: Temperature dependence of β_r and τ_r parameters from experimental results.

The stress-free reduction strain rate was determined by differentiating Equation (III.27), i.e.,

$$\dot{\varepsilon}_{ij}^{\text{reduction, stress free}} = \frac{a \times k}{3\tau_r}\left(\frac{\tau_r + t}{\tau_r}\right)^{\beta_r} \frac{\left(d\beta_r\left(\ln\left(\frac{\tau_r + t}{\tau_r}\right)\tau_r^2 + \ln\left(\frac{\tau_r + t}{\tau_r}\right)\tau_r t\right) + \beta_r\tau_r - \beta_r t d\tau_r\right)}{\left(\left(\frac{\tau_r + t}{\tau_r}\right)^{\beta_r} \Big/ \left[\left(\frac{\tau_r + t}{\tau_r}\right)^{\beta_r} + k\right]\right)^{\frac{2}{3}} \left(\left(\frac{\tau_r + t}{\tau_r}\right)^{\beta_r} + k\right)^2 (\tau_r + t)} \delta_{ij} \quad \text{(III.29)}$$

where k is defined to be $\left(\frac{L_f}{L_0}\right)^3 - 1$, a is defined to be $\frac{L_f}{L_0}$, $d\beta_r$ is short for $\frac{d\beta_r}{dT}\frac{dT}{dt}$, $d\tau_r$ is short for $\frac{d\tau_r}{dT}\frac{dT}{dt}$, t is the elapsed time since the start of sintering, and T is the temperature in Celsius. Similar to the sintering compact, it is assumed that the strain rate from reduction depends on the stress in the specimen. Specifically, because of the similarities between reduction shrinkage and sintering, the rate of shrinkage of a reducing body is assumed to be driven by a force similar to the sintering potential. Should the stress in the specimen build up in a manner opposing the shrinkage, it is assumed that the rate of shrinkage would decrease. Therefore, the stress-free strain rate is modified to account for stress according to

$$\dot{\varepsilon}_{ij}^{\text{reduction}} = \dot{\varepsilon}_{ij}^{\text{reduction, stress free}}\left(1 - \frac{\sigma_m}{\Sigma_r}\right), \qquad \text{(III.30)}$$

where $\dot{\varepsilon}_{ij}^{\text{reduction}}$ is the reduction strain rate, $\dot{\varepsilon}_{ij}^{\text{reduction, stress free}}$ is the unconstrained reduction strain rate given in Equation (III.29), σ_m is the hydrostatic stress defined as $(\sigma_{11} + \sigma_{22} + \sigma_{33})/3$, Σ_r is the net stress-free driving force for reduction, or 'reduction potential', and is assume to be ~1MPa. Because no information on the reduction potential could be found in the literature, a typical value for the sintering potential of most sintering ceramics was assumed.

III.4.3 Sintering

The sintering of the metal compact is assumed to be almost identical to that of the ceramic compact, with the exception that the initial density needs to be continually updated to account for the effects of reduction that can occur during sintering. Specifically, Equations (III.8), (III.10), and (III.12) are assumed to hold with the only difference between the sintering of the electrolyte and metal interconnect being the temperature dependent parameters and the way the initial density is defined, i.e.,

$$\dot{\rho}_{stress\_free} = (\rho_f - \rho) \left\{ d\beta_m \frac{dT}{dt} \ln \left(\frac{(\rho_f - \rho_0')^{\frac{1}{\beta_m}}}{(\rho_f - \rho)^{\frac{1}{\beta_m}}} \right) + \frac{\beta_m}{\tau_m} \left[\frac{(\rho_f - \rho_0')^{-\frac{1}{\beta_m}}}{(\rho_f - \rho)^{-\frac{1}{\beta_m}}} - (d\tau_m) + \frac{(\rho_f - \rho_0')^{-\frac{1}{\beta_m}}}{(\rho_f - \rho)^{-\frac{1}{\beta_m}}} (d\tau_m) \right] \right\} \quad \text{(III.31)}$$

where $d\beta_m$ is short for $\frac{d\beta_m(T)}{dT}\frac{dT}{dt}$, and $d\tau_m$ is short for $\frac{d\tau_m(T)}{dT}\frac{dT}{dt}$, both β_m and τ_m are Fe39Ni8Cr specific temperature dependent fitting parameters, t is the elapsed time since the start of sintering, ρ is the density, ρ_f is the theoretical solid density which is ~8.22g/cc, and ρ_0' is approximate equivalent initial density of the sintering compact as given in section III.4.5. The β_m and τ_m parameters were fit to measurements of the isothermal dimensional change of the sintering compact after reduction had completed. Dimensional shrinkage measurements were taken after reduction was fully completed to establish a consistent starting state for the characterization of sintering. Both the β_m and τ_m parameters could not be fit to the isothermal experiments through a least squares fit for all runs, because the fitting process destroyed any trends in the β_m and τ_m parameters with temperature. Specifically, the isothermal experiments did not completely decouple the

sintering and reduction shrinkage, which resulted in variations in the measured shrinkage at each temperature. These variations resulted in β_m and τ_m parameters with such a large uncertainty that no temperature dependent trend could be determined. Therefore, the β_m and τ_m parameters were only fit to the experimental data by the least squares method for the two experiments that exhibited the most experimental reproducibility, which was the 1260 °C and 1050 °C runs. With the values of β_m and τ_m at two temperatures, and the measured temperature dependence observed for the electrolyte given in Equation (III.14), trends were assumed and a least squares technique was used to determine β_m after selecting τ_m to be consistent with the trend. The τ_m parameter was selected such that it was a 'reasonable' compromise between the value given by a straight least squares fit and the ideal value indicated by the assumed trend. Figure III.15 shows the proximity of the model to the experimental results. Figure III.16 shows the values of β_m and τ_m at different temperatures, along with a function fit through the parameters. Equation (III.32) gives the temperature dependent curve-fits to the determined parameters.

$$\beta_m = 0.107 + 0.075\arctan\left(\frac{(T - 1080)}{66.66}\right), \quad \frac{d\beta_m}{dT} = \frac{0.001125}{1 + \left(\frac{T - 1080}{66.66}\right)^2} \qquad \text{(III.32)}$$

$$\tau_m = 36540e^{(-0.0084T)}, \quad \frac{d\tau_m}{dT} = -307e^{(-0.0084T)}, \quad \text{for } 750 < T < 1260$$

Where T is the temperature in Celsius, β_m is dimensionless, and τ_m is in minutes.

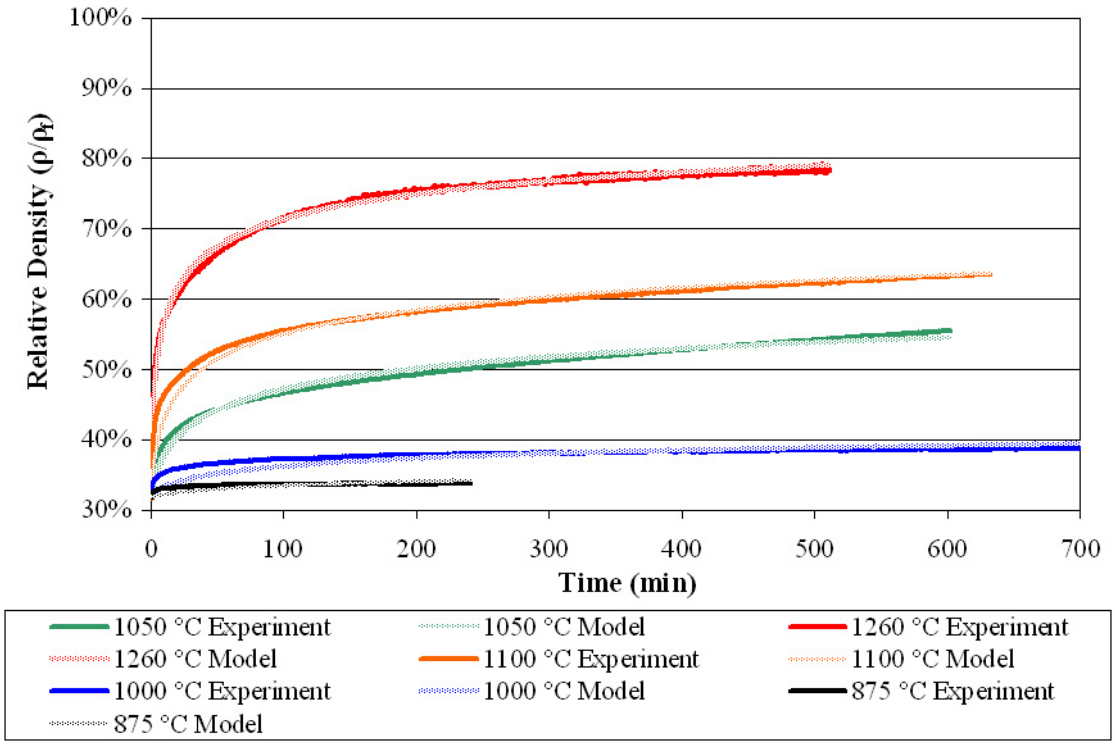

Figure III.15: Measured isothermal densification from sintering of Fe39Ni8Cr compared to model prediction after performing a least squares fit on model parameters. Experiments performed on honeycomb samples in 387 sccm Ar + 4% H_2.

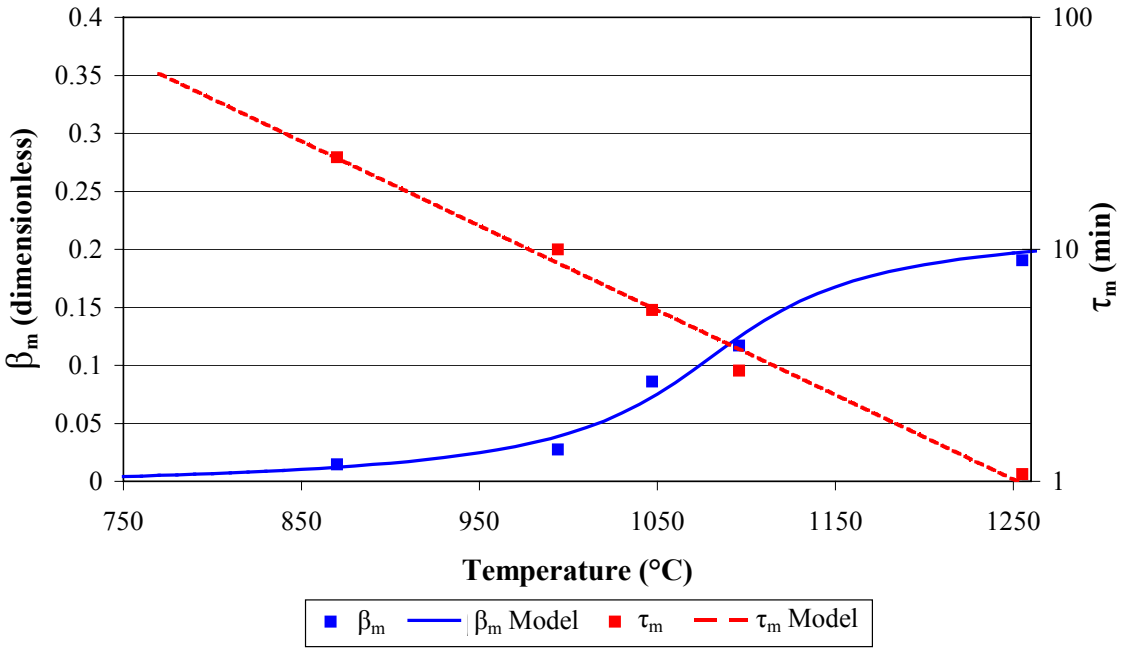

Figure III.16: Temperature dependence of β_m and τ_m parameters from experimental results.

III.4.4 Accuracy and Improvements to Sintering and Reduction Models

The accuracy of the free sintering behavior of the metal interconnect model cannot be compared to experimental results without also including the effects of reduction in the model. In other words, no experiment can be performed that represents the sintering behavior of the reduced metal interconnect without first reducing the metal oxide to metallic form. Therefore, the accuracy of the combined sintering reduction model can be assessed by comparison to experimental results. Figure III.17 compares the predicted total shrinkage of the reducing and sintering sample to the experimentally measured total shrinkage for two different temperature ramp rates and constant flow rate and H_2 concentration. The constant ramp rate temperature history used is independent of any of the isothermal measurements used to fit model parameters.

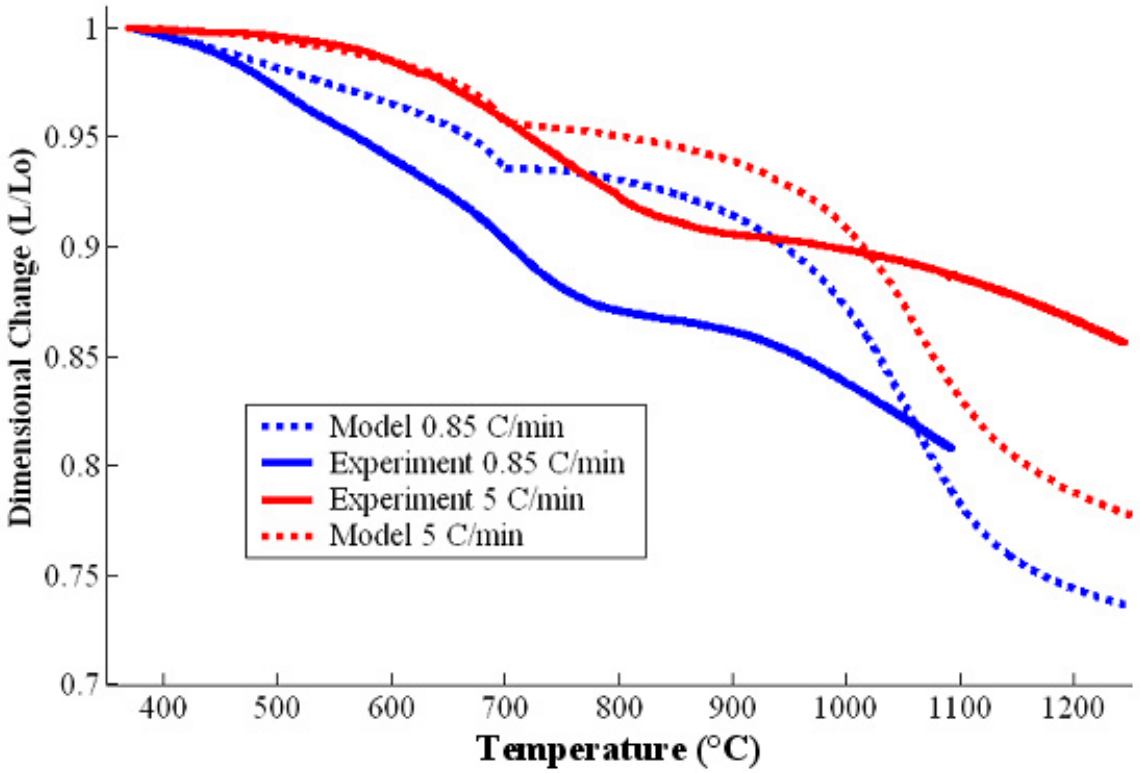

Figure III.17: Comparison of predicted and observed shrinkage of the Fe39Ni8Cr system when heated from 370 °C to 1270 °C at two different temperature ramp rates. The measurements were performed on a honeycomb Fe39Ni8Cr in 387 sccm Ar + 4% H_2.

As shown in Figure III.17, the model captures the trends of the material well, however, the overall accuracy of the model is not as good as that of the sintering model developed in Section III.3.2, and shown in Figure III.6. Three additional sources of error were identified for the sintering reduction model: the error associated with the method used to characterize the sintering parameters, the error associated with the method used to characterize the reduction parameters, and the model's neglect for the affects of the oxidation and reduction of the chrome in the system at elevated temperatures.

First of all, the method used to characterize the sintering curve involved taking dimensional measurements on the specimen only after the reduction shrinkage had come

to completion. This resulted in model parameters that predicted an artificially fast sintering rate because the remaining structure only contained close-packed metal particles after all the oxide particles had reduced. If the sintering behavior had been characterized during the reduction process, the measured sintering rate would have been much slower because oxide powders interspersed in-between the metal powders would have impeded the sintering process, and the predicted sintering behavior would have been much slower. Unfortunately, the sintering behavior cannot easily be characterized at arbitrary points during reduction. However, the cited β_m and τ_m parameters do exhibit the proper trend for the parameters and act as an upper bound for the sintering rate. Therefore, it is possible to augment the reported β_m and τ_m equations with a multiplier that slows the predicted sintering behavior. Equation (III.33) shows one possible modification to the existing model parameters, where the rate of sintering dependents on the extent of reduction that has occurred. Specifically, the τ_m parameter is multiplied by a scalar that drops to 1 as the structure becomes fully reduced. The value of the constant was chosen such that it minimized the error between the total predicted shrinkage and total measured shrinkage from several different constant ramp rate experiments.

$$\frac{\tau_m}{\tau_{m0}} = 1 + 20\left(1 - \eta\right) \qquad \text{(III.33)}$$

Where τ_m is the modified sintering parameter, $\tau_{m,0}$ is the sintering parameter as predicted by Equation (III.32), η is the reduction state variable as given in Equation (III.39) and varies from 0 to 1 as the structure proceeds from unreduced to fully reduced.

A secondary source of error in the model is the determination of the reduction shrinkage parameters. Specifically, the reduction shrinkage of the metal could not be accurately observed over 700 °C because it could not be separated from the shrinkage associated with sintering of the metal particles. Therefore, the reduction shrinkage behavior of the structure for all temperatures over 700 °C is based on the experimentally measured reduction shrinkage at 700 °C, which was the last temperature that reduction shrinkage could easily be separated from sintering. Obviously this induces substantial error if the temperature ramp rate is rapid enough that most of the reduction occurs at higher temperatures. One possible solution is to extrapolate the measured β_r and τ_r behavior to high temperatures, by assuming the parameters exhibit similar trends (i.e., τ decays exponentially, and the rate of change of β with temperature approaches zero at high temperatures) to the β and τ parameters shown in Figures III.5 and III.16 that were measured at high temperatures. Since the τ_r parameter already varies in an exponentially decaying fashion, its value at higher temperatures should simply be extrapolated to higher temperatures. The β_r parameter should presumably level out like it does in both other sintering models. Therefore the arctangent model, given in Equation (III.34), was used to extrapolate the β_r parameter to higher temperatures with the same initial value and similar slope to the one determined at 700 °C by Equation (III.28). The remaining constants in the arctangent model were then adjusted until the reduction behavior of the model accurately followed the observed reduction behavior in constant temperature ramp rate experiments.

$$\beta_r = 0.534 + 0.1\arctan\left(\frac{(T - 700)}{12.5}\right), \quad \frac{d\beta_r}{dT} = \frac{0.008}{1 + \left(\frac{T - 700}{12.5}\right)^2} \qquad \text{(III.34)}$$

$$\tau_r = 1171.2e^{(-0.00545T)}, \quad \frac{d\tau_r}{dT} = -6.383e^{(-0.00545T)}, \quad T > 700$$

Where T is temperature in Celsius, β_r is dimensionless, and τ_r is in minutes. Figure III.18 shows how the modified β_r and τ_r parameters vary with temperature. Note that the β_r and τ_r parameters given in Equation (III.28) were not affected below 700 °C.

A third source of error in the model could be attributed to the models neglect of the affects of chrome oxidizing and reducing in the system. Specifically, the Fe39Ni8Cr system starts out with pure chromium, but at high temperatures (~800 °C) and in the presence of water vapor (from the reduction of Fe_3O_4) the chrome tends to oxidize, slowing the sintering process. The applied constitutive equations neglect this effect, and the experimental parameters were recorded with little concern about the high temperature formation of chrome oxide particles in the specimen. Therefore, this could help explain some of the inaccuracies between the model and experimentally observed shrinkages.

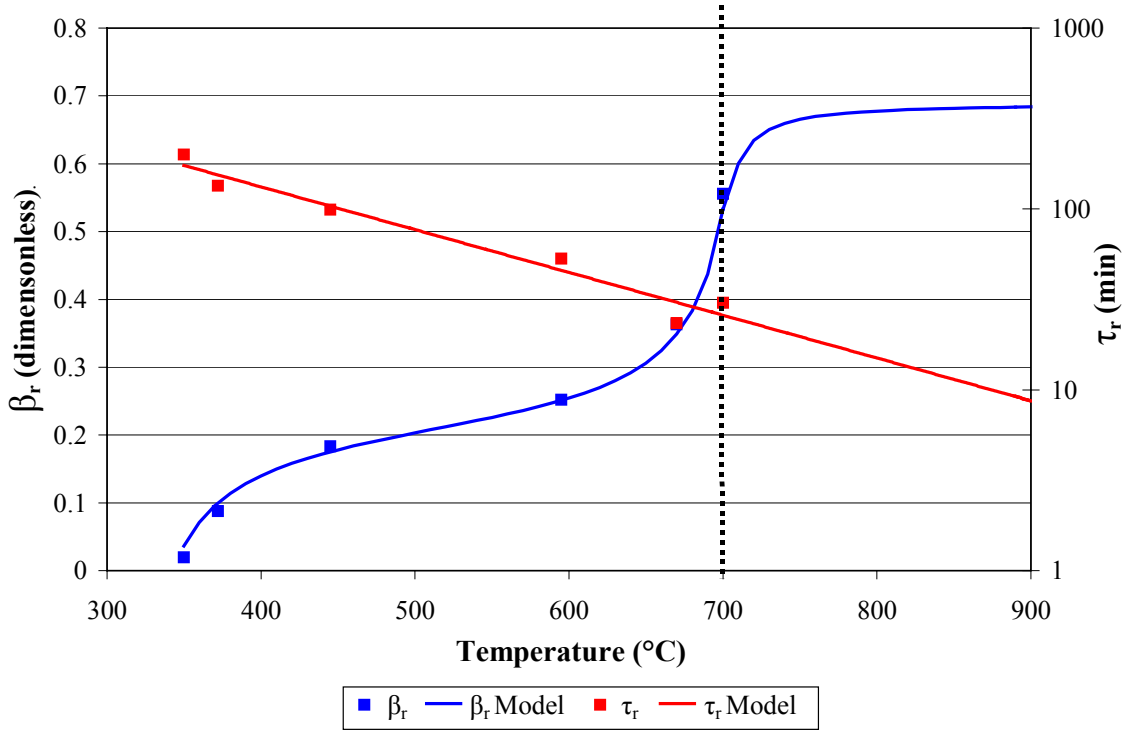

Figure III.18: Extrapolated time dependence of β_r and τ_r parameters from experimental results.

The improved accuracy of the revised model using corrected temperature dependent parameters is demonstrated in Figure III.19 and III.20. Figure III.19 shows the model prediction against the same experimental results as shown in Figure III.17. Figure III.20 shows the accuracy of the modified model when applied to an independent experiment that had a 'realistic' process temperature history.

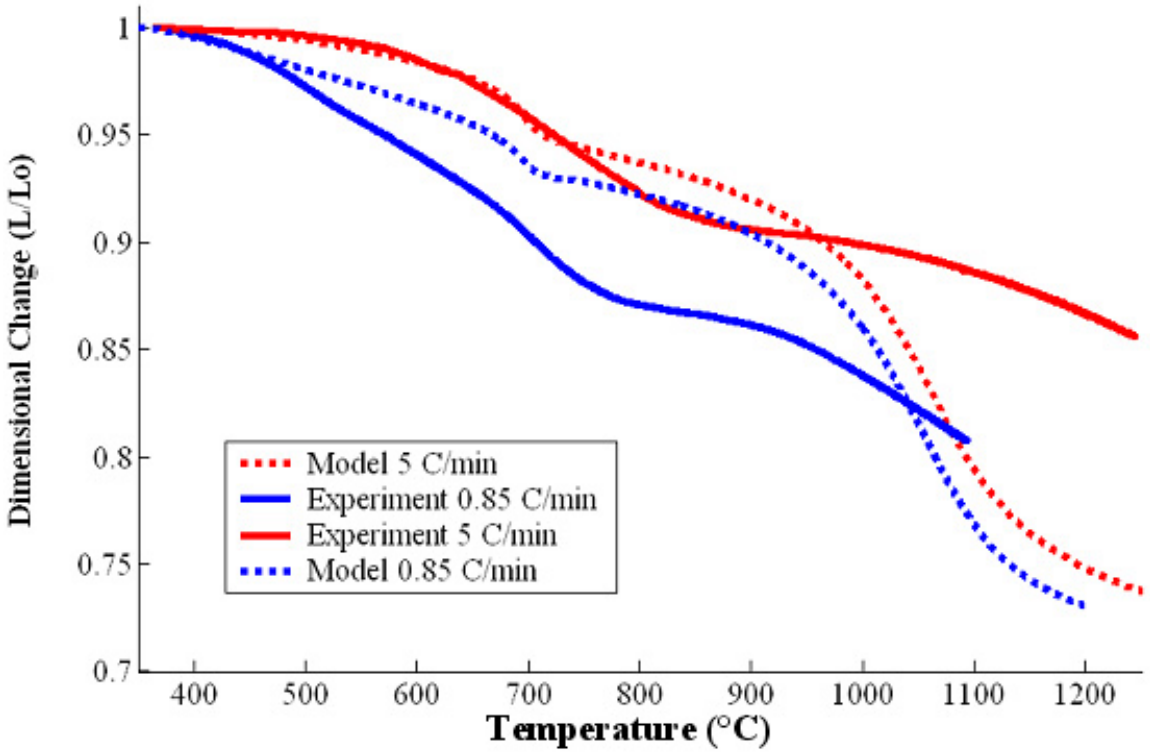

Figure III.19: Comparison of modified model to experimentally measured shrinkages of the Fe39Ni8Cr system when heated from 370 °C to 1270 °C at two different temperature ramp rates. The measurements were performed on a honeycomb Fe39Ni8Cr in 387 sccm Ar + 4% H_2.

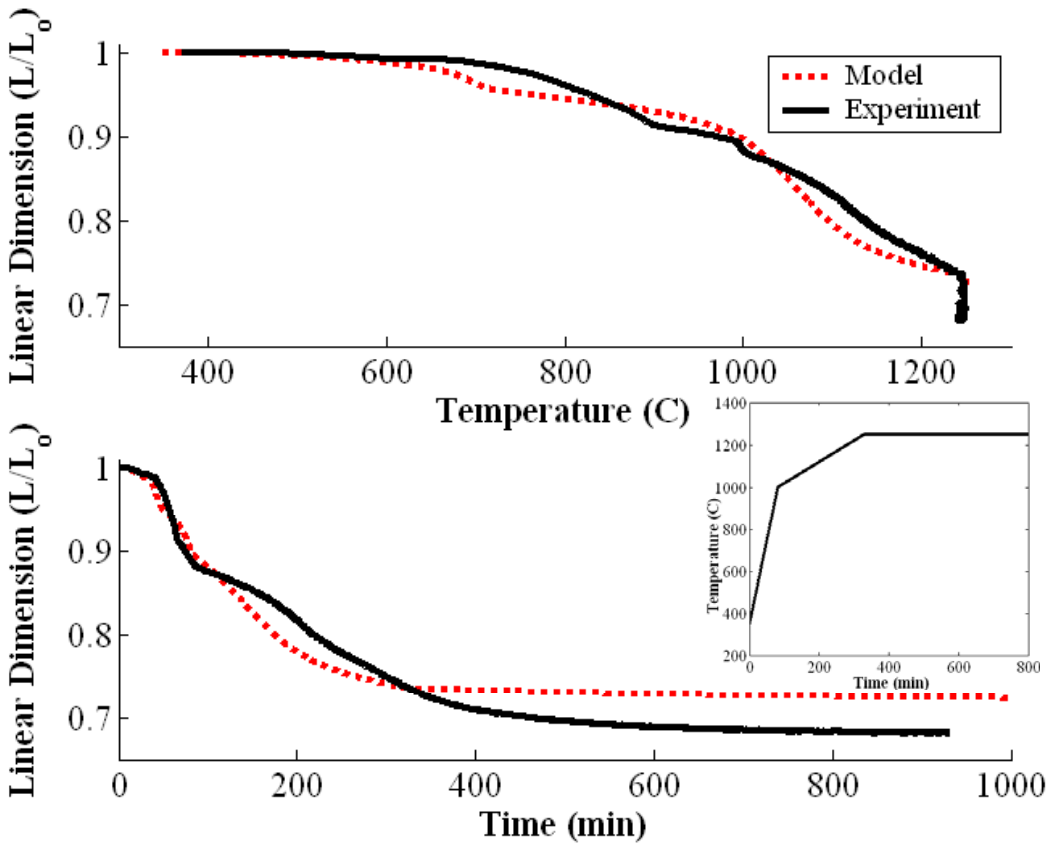

Figure III.20: Comparison of modified model to an observed shrinkage (independent of any parameter fitting) undergone by the Fe39Ni8Cr system when being heated from 370 °C to 1270 °C for a 'realistic' temperature history. The measurements were performed on a honeycomb Fe39Ni8Cr in 387 sccm Ar + 4% H_2.

III.4.5 Evolution of Mass and Density

The density of the specimen changes during both reduction and sintering. During the reduction process, both the mass and volume change. However, during the sintering process, the mass remains constant and only the volume changes. The dimensional change of the specimen during reduction and sintering is covered in sections 3.4.2 and 3.4.3 respectively, but the mass loss during reduction is addressed in this section.

The rate of mass loss during the firing process has an effect on the rate of reduction shrinkage; however, it is implicit in the reduction model for the H_2 gas

concentration and flow rate that the empirical model was fit. The shrinkage behavior of the metal oxide compact was measured while oxygen was leaving the specimen. However, the reduction strain-rate model was only measured at 1 flow rate, and 1 gas concentration, so it is valid only for those same conditions. In other words, the reduction strain-rate model does not need to take the mass loss from reduction into account for the given flow rate and concentration, but it cannot be used to predict the strain rate for other H_2 flow rates because it does not take the rate of mass loss from reduction explicitly into account.

The rate of mass loss during the firing process affects the sintering process if reduction occurs simultaneously with sintering. As mentioned before, reduction can occur while sintering is taking place, so long as the structure is open enough to allow oxygen to diffuse out of the structure. The mass removed from the structure during sintering affects the structure's current density. The sintering process inherently depends on the current density of the structure. Therefore, the initial density of the sintering specimen needs to be continually adjusted to account for density changes due to the reduction process. Equation (III.35) shows how the initial sintering density varies with reduction. Note that the volume shrinkage L/L_o term was given in the reduction section above.

$$\rho_0' = \left(\rho_{ox,bi}\right)\left(\frac{\frac{m}{m_0}}{\left(\frac{L_{red}}{L_0}\right)^3}\right) = \frac{\left(m_0 - m_{oxred}\right)}{L_{red}^3} \qquad \text{(III.35)}$$

Where ρ_0' is the equivalent initial density of the sintering compact, $\rho_{ox,bi}$ is the density of the green compact including binder and is ~3.4 g/cc, m is the mass, m_0 is the initial mass in the green state, L_{red} is the length including reduction shrinkage, but neglecting thermal expansion and sintering shrinkages, L_0 is the initial length in the green state, and m_{oxred} is the mass of oxygen that has left the structure from reduction.

The rate of mass loss from the specimen during reduction depends on the temperature of the specimen, because magnetite, and nickel oxide reduce at different temperatures and at different rates. In other words, the activation energy and corresponding rate-limiting steps in the reduction process differ for the two oxide powders that comprise the composition of interest. Specifically, NiO reduces at a lower temperature, and the rate-limiting step seems to be solely a function of temperature. The reduction of Fe_3O_4 on the other hand takes place at higher temperatures and is limited by the partial pressure of hydrogen gas to water vapor.

The mass loss from the specimen is non-dimensionalized by the initial mass of the specimen as shown in Equation (III.36), which expresses the mass loss equation in terms of the initial mass, the level of reduction in the compact, and the initial mass fraction of nickel oxide and magnetite powders.

$$\frac{m}{m_0} = \frac{m_0 - m_{oxred}}{m_0} \tag{III.36}$$

Where m is the mass, m_0 is initial mass in the green state, and m_{oxred} can be recast as

$$m_{oxred} = m_o \left(X_{Ni}\eta_{Ni} + X_{Fe}\eta_{Fe} \right) \ , \qquad \text{(III.37)}$$

where X_{Ni} is the initial mass of oxygen associated with NiO in the green state, η_{Ni} is a normalized reduction parameter that gives the level of reduction of NiO from unreduced 0 to fully reduced 1, X_{Fe} is the initial mass of oxygen associated with Fe_3O_4 in the green state, and η_{Ni} is a normalized reduction parameter that gives the level of reduction of Fe_3O_4 from unreduced 0 to fully reduced 1. Substituting Equation (III.37) into Equation (III.36) and rearranging yields

$$\frac{m}{m_0} = \left(1 - \left[X_{Ni}\eta_{Ni} + X_{Fe}\eta_{Fe} \right]\right) \ . \qquad \text{(III.38)}$$

The initial mass fractions of nickel oxide and magnetite are shown in Equation (III.39) for the Fe39Ni8Cr system. The mass fraction that should be used depends on if the measured initial mass included the weight of the binder in the compact, or just the oxide powders.

For 53Fe39Ni8Cr with NO binder added
$X_{Ni} = 0.0811, \quad X_{Fe} = 0.1547, \quad \eta = 0.344\eta_{Ni} + 0.656\eta_{Fe}$

For 53Fe39Ni8Cr with 10.8% binder and water added
$X_{Ni} = 0.0724, \quad X_{Fe} = 0.1380, \quad \eta = 0.344\eta_{Ni} + 0.656\eta_{Fe}$ (III.39)

Where η is a normalized reduction parameter that gives the total level of reduction of the system from unreduced 0 to fully reduced 1. Studies of the reduction behavior of nickel

oxide were performed using the hygrometer as outlined in Chapter II. The experimentally derived reduction rate model for the nickel oxide in the compact is given by

$$\eta_{NiO} = \int_0^t \dot{\eta}_{NiO}\, dt,\ \eta_{NiO}(0) = 0,\ 0 \le \eta_{NiO} \le 1$$

$$\frac{d\eta}{dt} = \frac{d\left[CC(T)\right]}{dT}\frac{dT}{dt} + \frac{d\left[DD(T)\right]}{dT}\frac{dT}{dt}\arctan\left(\frac{\left(t - AA(T)\right)}{BB(T)}\right) +$$

$$+ DD(T)\left(\frac{1 - \frac{d\left[AA(T)\right]}{dT}\frac{dT}{dt} - \frac{\left(t - AA(T)\right)}{BB(T)^2}\frac{d\left[BB(T)\right]}{dT}\frac{dT}{dt}}{1 + \frac{\left(t - AA(T)\right)^2}{\left(BB(T)\right)^2}}\right)$$

$$\frac{d\left[AA(T)\right]}{dT} = -0.00156T + 0.387,\ \frac{d\left[BB(T)\right]}{dT} = -0.00163T + 0.5947$$

$$\frac{d\left[CC(T)\right]}{dT} = \left(8.174\times10^{-6}\right)T - 0.00317,$$

$$\frac{d\left[DD(T)\right]}{dT} = \left(-6.825\times10^{-8}\right)T^2 + \left(4.698\times10^{-5}\right)T - 0.00811\ ,$$

(III.40)

where T is temperature in Celsius and t is elapsed time since the start of NiO reduction. Similar reduction studies were performed to characterize the reduction of Fe_3O_4 in the compact as shown in Chapter II. The experimentally determined rate of mass loss from Fe_3O_4 during reduction can be expressed as

$$\eta_{Fe} = \frac{\int_0^t \dot{m}_{Fe}\, dt}{X_{Fe} m_0},\ \eta_{Fe}(0) = 0,\ 0 \le \eta_{Fe} \le 1$$

$$\dot{m}_{Oxygen} = \begin{cases} \dfrac{P_{H_2O} Q_{total}}{RT} c, & \text{for } 0 < m_{mass\ lost} < 0.85 M^* \\ \dfrac{1}{5} \dfrac{P_{H_2O} Q_{total}}{RT} c, & \text{for } 0.85 \le m_{mass\ lost} < M^* \\ 0, & \text{for } m_{mass\ lost} \ge M^* \end{cases}, \qquad \text{(III.41)}$$

where P_{H_2O} is the partial pressure of water vapor and is equal to $P_{total} X_{H_2} f(T)$, f(T) is the equilibrium partial pressure of reducing water vapor at a given temperature in Celsius and is given as $(3.23 \times 10^{-4})T - 0.0893$, X_{H_2} is the volumetric percent of H_2 in the carrier gas, Q is the total volumetric flow rate in m^3/min, R is the universal gas constant 8.3145 J/mol-K, c is the molar mass of oxygen, and T is constant at 283 K.

III.4.6 Viscoplastic Model

The constitutive equation that governs the viscoplastic deformation of the body was taken from a model developed by Marin and McDowell (McDowell 1992; E. B. Marin 1996; E. B. Marin 1998). The following model gives a fully associative unified viscoplastic strain rate relation for porous metals, based on an extension of the BCJ constitutive model (Bammann 1990; D. J. Bammann 1993) and a void growth relation due to Cocks (Cocks 1989). Furthermore, it is assumed that the reduced metal only

behaves as a metallic when reduction is complete, i.e., $\dot{\varepsilon}_{ij}^{vp} = 0$ for $\eta < 1$. The viscoplastic strain rate is split into deviatoric and dilational (volumetric) parts, respectively, i.e.,

$$\dot{\varepsilon}_{ij}^{p} = \dot{\varepsilon}_{ij}^{p}\Big|_{d} + \dot{\varepsilon}_{ij}^{p}\Big|_{v} = g\, n_{ij}^{s} + \tilde{\beta}\, g\, e_{ij} \quad \text{for } \eta = 1 \ , \tag{III.42}$$

where $n_{ij}^{s} = \dfrac{s_{ij}}{\sqrt{s_{kl}s_{kl}}}$, $\tilde{\beta} = \sqrt{2}\dfrac{h_2}{h_1}\dfrac{I_1}{\sqrt{3J_2^o}}$, $e_{ij} = \delta_{ij}/\sqrt{3}$, and g is the kinetics factor for viscoplastic flow given by

$$g = \sqrt{\frac{3}{2}}\Theta(T)\sinh\left(\frac{\Phi - h_3\left(R + Y(T)\right)}{h_3\, V(T)}\right) \ . \tag{III.43}$$

Here, $\Phi = \sqrt{3h_1J_2^o + h_2I_1^2}$ is the driving force term based on the applied stress, $\varphi = 1 - \dfrac{\rho}{\rho_f}$ is the porosity as before, $I_1 = \sigma_{kk}$ is the first dilatational invariant, $J_2^o = \dfrac{1}{2}s_{mn}s_{mn}$ is the second deviatoric invariant, $\Theta(T)$, $Y\left(T\right)$, and $V(T)$ are material specific constants. The back stress is neglected and the porosity dependent h_i factors are given from the Cocks model as

$$h_1 = 1 + \frac{2}{3}\varphi, \quad h_2 = \frac{1}{2}\left(\frac{1}{n+1}\right)\frac{\varphi}{1+\varphi}, \quad h_3 = \left(1 - \varphi\right)^{\frac{1}{n+1}} \ , \tag{III.44}$$

where n is the strain rate sensitivity exponent approximately equal to 0.04. In this model, the scalar measure of effective plastic strain rate is given by

$$\dot{\bar{\varepsilon}}^{p} = \sqrt{\frac{2}{3h_1}}\frac{h_3}{1-\varphi}\sqrt{\dot{\varepsilon}^{p}_{kl}\dot{\varepsilon}^{p}_{kl} + \frac{h_1}{6h_2}\left(1-\frac{2h_2}{h_1}\right)\left(\dot{\varepsilon}^{p}_{ii}\right)^2} \quad . \tag{III.45}$$

Only isotropic hardening is assumed for simplicity, with the evolution equation for the yield strength given by the hardening/dynamic recovery form

$$\dot{R} = \left(B(T) - K_d(T)\,R^2\right)\dot{\bar{\varepsilon}}^{p} \quad , \tag{III.46}$$

where B(T) and $K_d(T)$ are material specific constants, and the initial condition is R(0)=0 following the reduction process. Static thermal recovery necessary to model steady state creep deformation is omitted here, although short-term relaxation is fully addressed. Finally, the rate of change of porosity is given by

$$\dot{\varphi}_v = (1-\varphi)\,\dot{\varepsilon}^{p}_{kk} = \sqrt{3}\,(1-\varphi)\frac{\tilde{\beta}}{\sqrt{1+\tilde{\beta}^2}}\sqrt{\dot{\varepsilon}^{p}_{kl}\dot{\varepsilon}^{p}_{kl}} = \sqrt{6}\,(1-\varphi)\frac{h_2}{h_1}\frac{I_1}{\sqrt{3J_2^o}}\sqrt{\dot{\varepsilon}^{p}_{kl}\big|_d\;\dot{\varepsilon}^{p}_{kl}\big|_d} \quad , \tag{III.47}$$

where $\dot{\varphi}_v$ is the time rate of change of porosity due to void growth, and φ is the total level of porosity in the system including the affects of sintering and reduction. The material specific constants can be fit to the experimental data in Chapter II once the

viscoplastic model has been numerically implemented. It is envisioned that the constants will have the form

$$V(T) = C_1 \exp\left(-\frac{C_2}{T}\right), \quad Y(T) = C_3 \exp\left(-\frac{C_4}{T}\right)$$
$$B(T) = C_5 \exp\left(-\frac{C_6}{T}\right), \quad K_d(T) = C_7 \exp\left(-\frac{C_8}{T}\right) \qquad \text{(III.48)}$$
$$\Theta(T) = C_9 \exp\left(-\frac{C_{10}}{T}\right) .$$

III.4.7 Elastic Constants

The isotropic hypo-elastic model requires knowledge of the elastic constants contained within the C matrix in addition to the inelastic strain rate terms. The Fe39Ni8Cr system was assumed to be isotropic, resulting in the matrix of coefficients

$$[C] = \frac{E(1-\nu)}{(1+\nu)(1-2\nu)} \begin{bmatrix} 1 & \frac{\nu}{(1-\nu)} & \frac{\nu}{(1-\nu)} & 0 & 0 & 0 \\ \frac{\nu}{(1-\nu)} & 1 & \frac{\nu}{(1-\nu)} & 0 & 0 & 0 \\ \frac{\nu}{(1-\nu)} & \frac{\nu}{(1-\nu)} & 1 & 0 & 0 & 0 \\ 0 & 0 & 0 & \frac{1-2\nu}{2(1-\nu)} & 0 & 0 \\ 0 & 0 & 0 & 0 & \frac{1-2\nu}{2(1-\nu)} & 0 \\ 0 & 0 & 0 & 0 & 0 & \frac{1-2\nu}{2(1-\nu)} \end{bmatrix} , \qquad \text{(III.49)}$$

where E is Young's modulus, and ν is Poisson's ratio. Two different sets of elastic constants are used in the model, one prior to the onset of sintering, and one during and after sintering occurs. The elastic modulus was measured for a similar structure in the green state and after binder burnout, but before sintering. However, because only the elastic modulus was measured, the Poisson's ratio was assumed to be the same as the solid material. Equation (III.50) outlines the properties for the material before the onset of sintering. Note that the temperature and porosity dependent modulus were not directly measured. Instead they are linear interpolations between the two different modulus measurements that were made, and the onset of the porosity knockdown equation after sintering has begun as given by Equation. The experiments that gave the elastic moduli are described in Chapter II.

$$\begin{cases} E = 0.44 \text{ GPa}, \ 0 < T < 270 \\ E(T) = -0.00505T + 1.8035\text{GPa}, \ 270 \le T \le 350 \\ E = 0.036 \text{ GPa}, \ 350 < T < 750 \\ E(\bar{\rho}) = 160.97\bar{\rho} - 66.54 \ \ 0.414 < \bar{\rho} \le 0.6, \ \ T > 750 \end{cases} \qquad \text{(III.50)}$$

$$\nu = 0.25, \ \ G(T,\bar{\rho}) \equiv \frac{E(T,\bar{\rho})}{2(1+\nu)}, \ \ \bar{\rho} \equiv \frac{\rho}{\rho_f} = \text{relative density}$$

Where T is the temperature in Celsius. The temperature dependence of the elastic modulus was estimated by linearly interpolating between the measured (see Chapter II) modulus at room temperature and 900 °C, and applying the determined slope to the room temperature modulus corrected for porosity using Equation (III.22), i.e.,

$$E_0(T) = -0.04077T + 159.8 \text{ [GPa]} \ , \qquad \text{(III.51)}$$

where T is the temperature in Celsius. The effects of porosity on the elastic constants were then accounted for by using Atkinson and Selcuk model shown in Equation (III.22) and represented in Figure III.21.

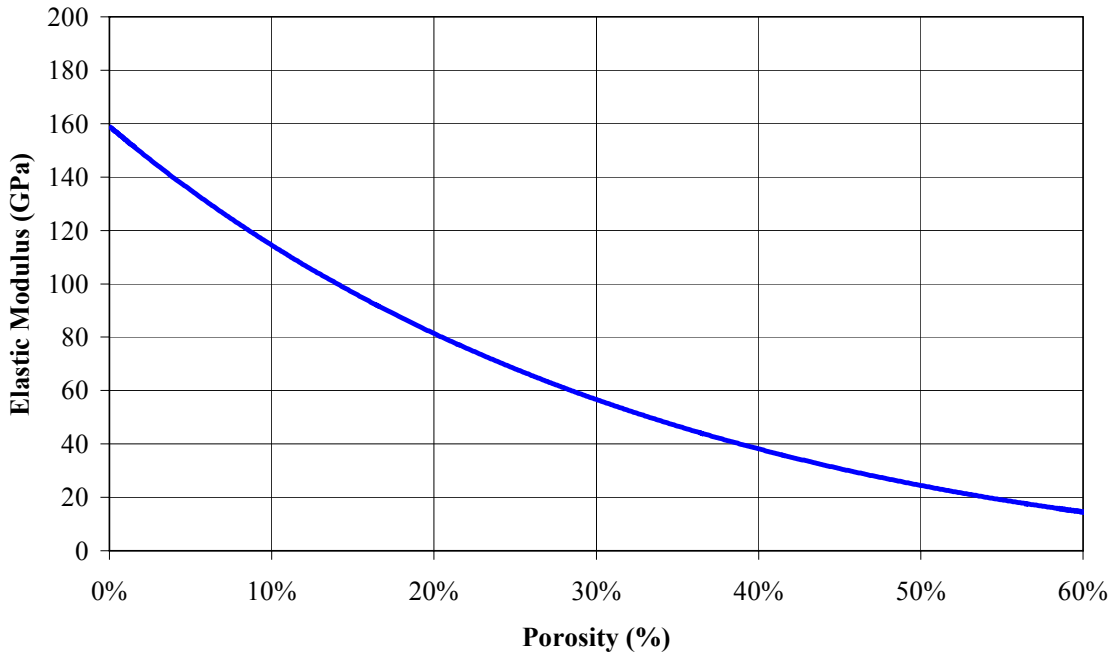

Figure III.21: Evolution of Young's modulus with porosity for Fe39Ni8Cr at room temperature, based on Atkinson and Selcuk model.

CHAPTER IV

FUTURE WORK AND CONCLUSIONS

IV.1 Summary of Developed Model

The multi-physics constitutive model developed in Chapter III is comprised of a series of strain rate equations that predict the behavior of the ScSz and Fe39Ni8Cr hybrid SOFC stack during manufacturing. A total of 11 different material behaviors and responses were identified and characterized as follows: electrolyte sintering, electrolyte thermal expansion, electrolyte viscous relaxation, electrolyte elastic response, interconnect sintering, interconnect reduction shrinkage, interconnect thermal expansion, interconnect viscous plastic flow, interconnect elastic response, interconnect NiO reduction, and interconnect Fe_3O_4 reduction. In contrast to the 11 behaviors that were characterized, 3 behaviors: binder burnout, interfacial slip at the constrained joint, and the high temperature affects of the oxidation and reduction of chrome and other high temperature phase change affects, were all left uncharacterized. A brief summary of the origin of each term in the model will be described approximately in order of the most to the least accurate term.

The thermal expansion of both materials was directly measured and therefore assumed to have the least error associated with it. Likewise, the reduction shrinkage model for the metal interconnect was strictly an empirical model based off of experiments performed on the Fe39Ni8Cr system. The model was shown to have good accuracy for a variety of different temperature profiles between 350 °C and 700 °C, the

temperature range experiments were preformed over, assuming a constant 387 sccm flow rate composed of 96% Argon and 4% H_2. The model is suitable for temperatures over 700 °C, and flow conditions that are near the above mentioned conditions, but the accuracy steadily decreases as the conditions move further away from the experimentally characterized region.

The sintering shrinkages of both materials were characterized by fitting experimental data to a mechanism-based model found in the literature. The predicted unconstrained shrinkage behavior of monolithic honeycomb structures heated with various schedules was found to be in good agreement with experimental results. However, the accuracy of the developed model could not be tested for constrained system because no stress dependent numerical integration scheme was developed. Furthermore, the sintering model associated with the metal interconnect was characterized after reduction had completed and therefore predicts an excessively fast shrinkage (due to the more dense material structure after reduction shrinkage had occurred).

The reduction of Fe_3O_4 was characterized by developing a mechanism-based model that was correlated to experimental results for the given system. The developed model should be accurate for any flow rate, H_2 concentration, or temperature; however, experiments were never performed at other H_2 concentrations or flow rates to validate this. Furthermore, the reduction rate after the first 85% of metal was reduced was approximated with a straight line instead of a more suitable decaying function. Finally, the effects of sintering on reduction were never considered, because no samples were ever heated to a point where sintering impeded the reduction process, but this is not always the case. The reduction of NiO was characterized using a strictly empirical

model, and should be very accurate for the flow rate (387 sccm), H_2 concentration (Argon + 4% H_2), and temperature range (350 °C to 700 °C) that it was measured over.

The viscous plastic flow of Fe39Ni8Cr can be characterized by fitting the chosen porous plasticity model to high temperature uniaxial tension and relaxation tests. The accuracy of the model was not be checked because the given equations were never integrated, however, the number of experiments should provide an accurate representation of the visco-plastic relaxation of the metal interconnect. The linear viscous relaxation of the ScSz was represented using models developed in the literature. The material parameters needed for the model were taken from literature values of pure Zirconia and 8% YSZ. Therefore, the viscous relaxation behavior of the material is not based on experimental data from our ScSz composition and is therefore less representative of its behavior.

The predicted evolution of the elastic constants with temperature and porosity was determined by linearly interpolating between known values and using a model developed in the literature to correct for porosity effects. The elastic constants were measured for both the Fe39Ni8Cr system at its ending porosity level, and the generic compact before and after binder-burnout. The elastic constants for the ScSz were estimated from values in the literature. The transition of material properties at the onset of sintering were approximated using a linear interpolation between the measured properties after binder burnout, and the predicted behavior of the solid material corrected for porosity after choosing a porosity level at which the materials were considered dense enough to behave in accordance with the porosity knockdown equations. Figure IV.1 gives an approximate

layout of the evolution of the fracture strength of YSZ and Fe39Ni8Cr during the manufacturing process.

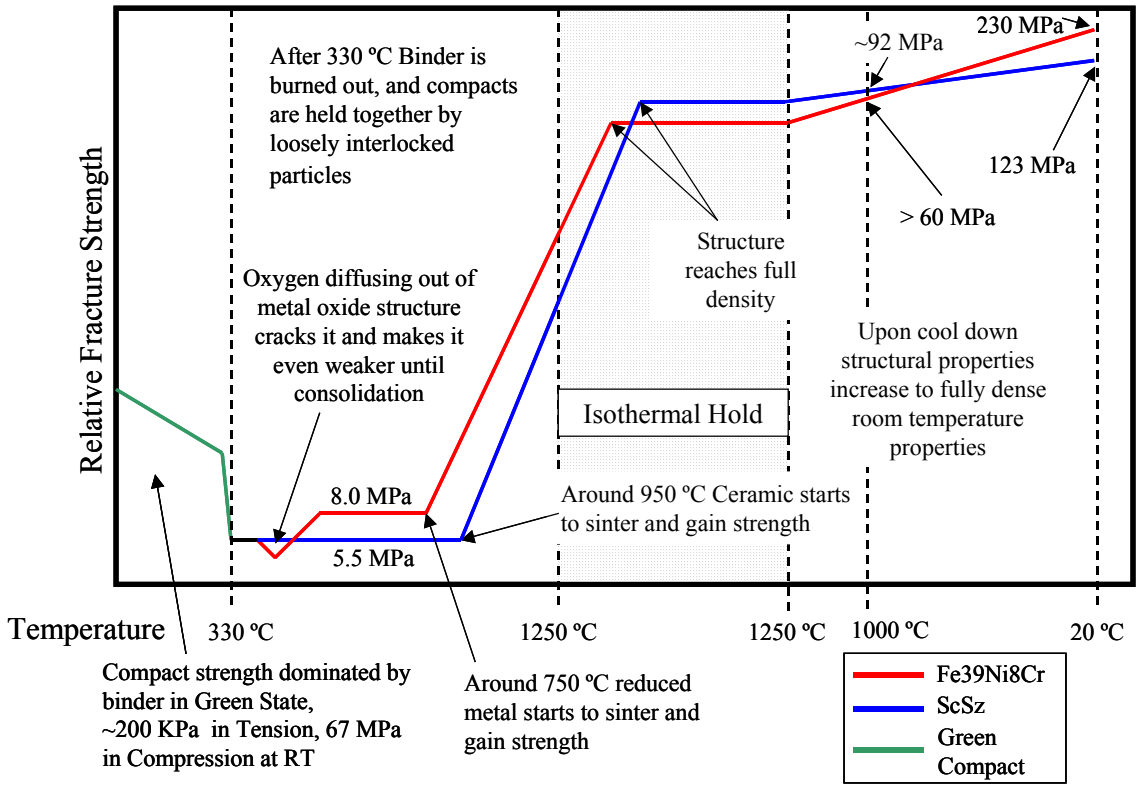

Figure IV.1: Approximate evolution of fracture strength of 15% porous Fe39Ni8Cr and 15% porous YSZ during the manufacturing process. Fracture strengths not to scale.

IV.2 Implementation of Model

The developed equations in Chapter III are a series of strain rate equations that require numerical integration over both the internal state variables and the tri-axial state of strain within the material system. The numerical solution to the system requires numerical tracking of several state variables, namely, the relative density (ρ/ρ_f), the

total reduction parameter (η), the magnetite reduction parameter $\left(\eta_{Fe}\right)$, the nickel oxide reduction parameter $\left(\eta_{Fe}\right)$, and the flow stress in the viscoplastic model (R). Additionally several initial conditions need to be specified, such as, total volumetric flow rate of gas (Q_{total}), volume fraction of Hydrogen in carrier gas $\left(X_{H_2}\right)$, and initial mass of the green compact (M^*). The integration code must also have information about the temperature, time, strain, current stress level, and all the associated time derivatives. It is envisioned that an Abaqus user material (umat) could be written to calculate the evolution the state variables, and solve for the stress level in the system through an iterative two-level Newton Raphson (NR) technique that estimate the current density in the system before going on to calculate the stress in the system. The two-level NR approach is needed to account for the coupling between densification rate and stress level in the system that is exhibited in Equation (III.10). A generalized midpoint integration scheme (E. B. Marin 1996) could be used as a compromise between performance and stability.

IV.3 Validation and Extension of Model

The developed model could not be fully validated because integration of the stress terms was never carried out. Therefore, the predicted affects of a tri-axial state of stress on material were never observed. However upon successful integration of the completed model, several validations can be made. First, the predicted deformation in the hybrid system can be compared to the experimentally observed deformation shown in Figure IV.2. Second, the predicted rate and degree of material shrinkage in the constrained

hybrid system can be compared to the experimental results shown in Figures IV.3, IV.4, and IV.5. Specifically, the chosen reduction potentials should be able to be verified by comparing the time and magnitude of shrinkage in Figure IV.5 with the predicted model shrinkage. Likewise, the sintering potential Σ could be verified by comparison of Figures IV.3 and IV.4 to the predicted model results. Finally, the elastic constants of the system can be indirectly checked by comparing the predicted deformation of the constrained system to the actual deformation as shown in Figure IV.2. After the above checks and possible corrections have been made to the model, then all components of the model will have been adequately checked, and the model will be ready for its desired uses.

An interesting observation was that the bulk of the deformation in the hybrid structure that is shown in Figure IV.2 was observed to occur on heat up prior to 700 °C for slowly heated specimens (~1 °C/min). Therefore the dilatometer output for slowly heated specimens can contain artifacts because the sample being measured no longer posses square edges. One such artifact can be seen in Figure IV.4 at ~1065 °C.

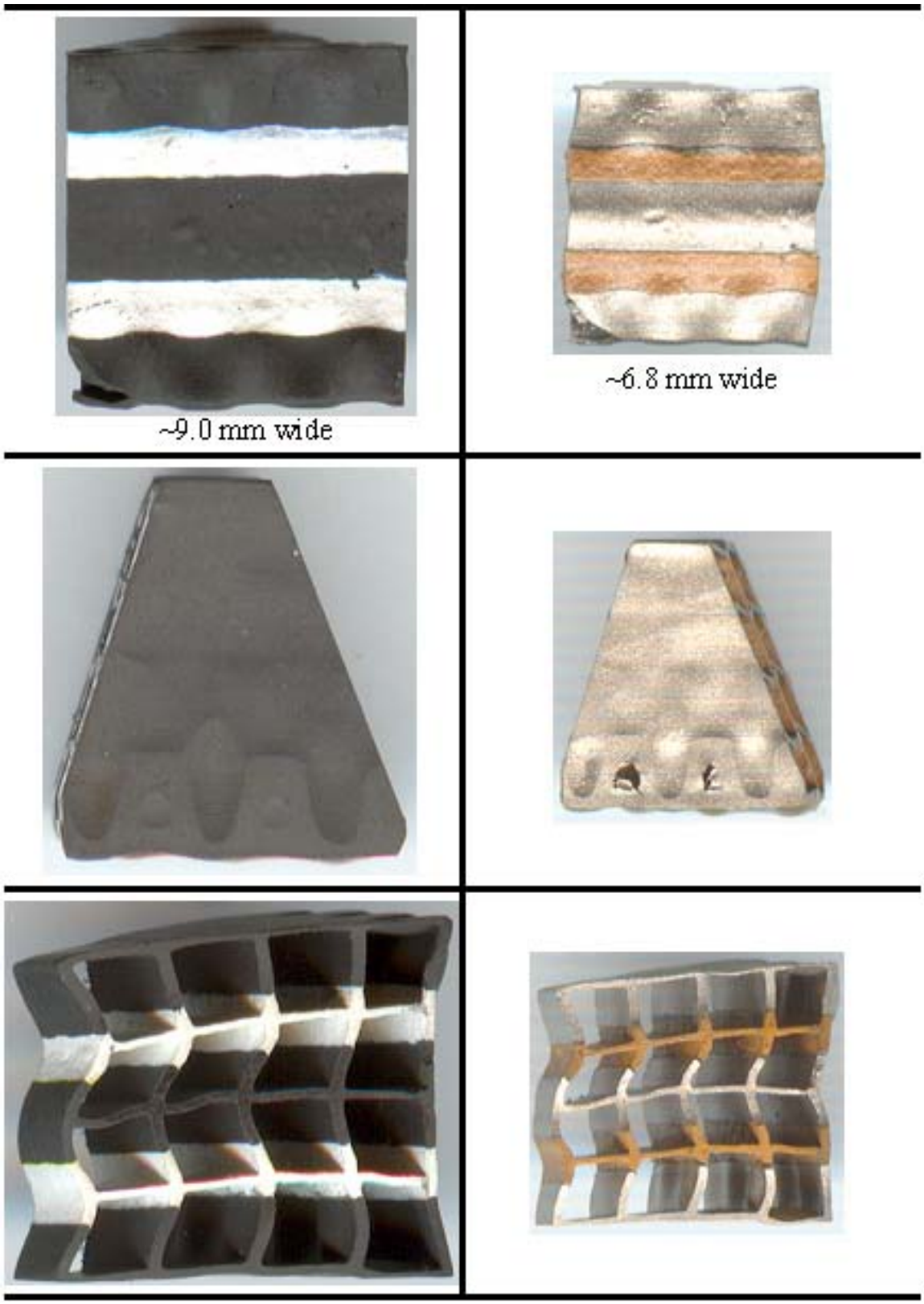

Figure IV.2: Pictures of Fe39Ni8Cr and ScSz hybrid structure in green state (left) and after processing (right) in 0.75 °C/min ramp to 1250 °C with 4 hour hold at 1250 °C and 8 °C/min cool down in 387 sccm Argon + 4% H_2. Pictures to scale with each other.

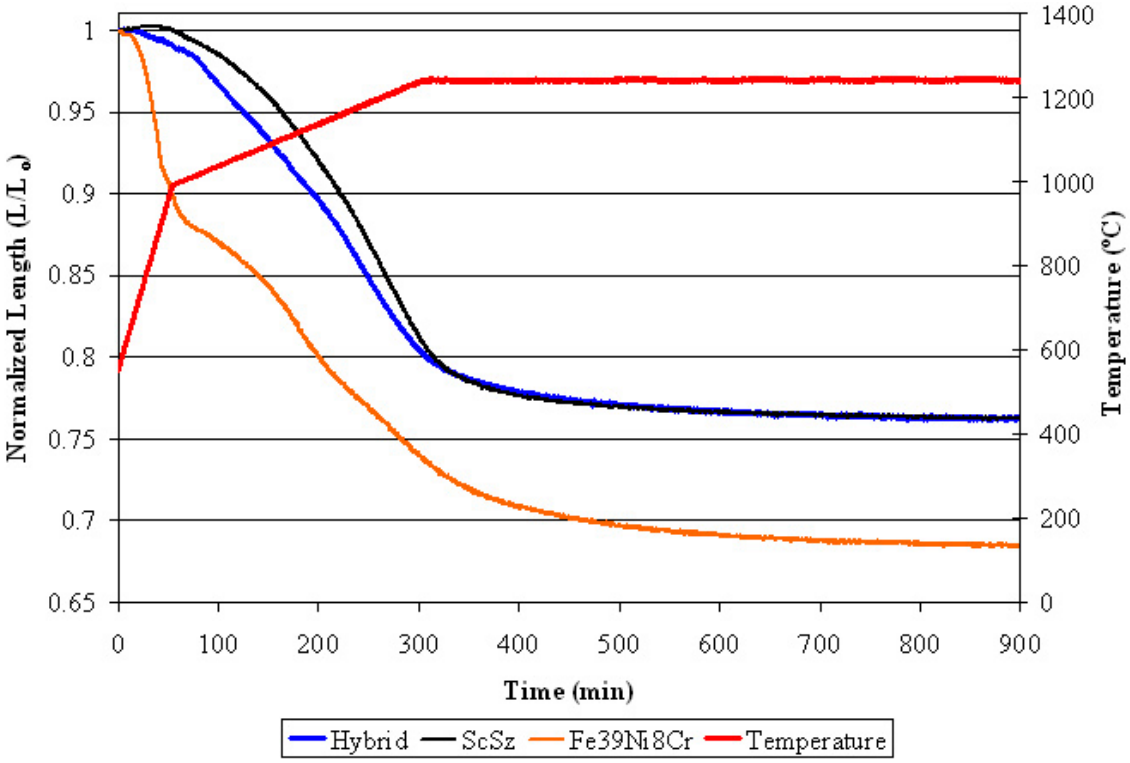

Figure IV.3: Comparison of constrained sintering curve of Hybrid Fe39Ni8Cr, ScSz system with unconstrained sintering curves from ScSz and Fe39Ni8Cr. All runs were performed in 387 sccm Ar + 4% H_2.

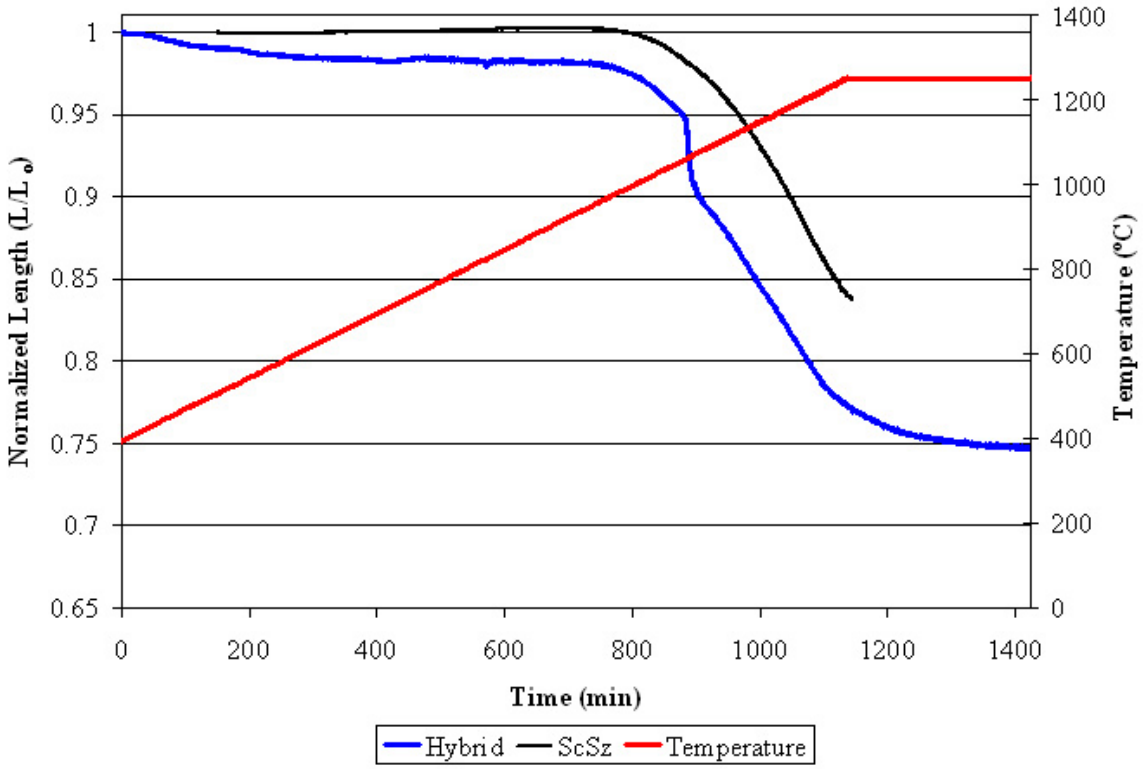

Figure IV.4: Comparison of constrained sintering curve of Hybrid Fe39Ni8Cr, ScSz system with unconstrained sintering curves from ScSz. All runs were performed in 387 sccm Ar + 4% H_2. Specimen shown in Figure IV.2.

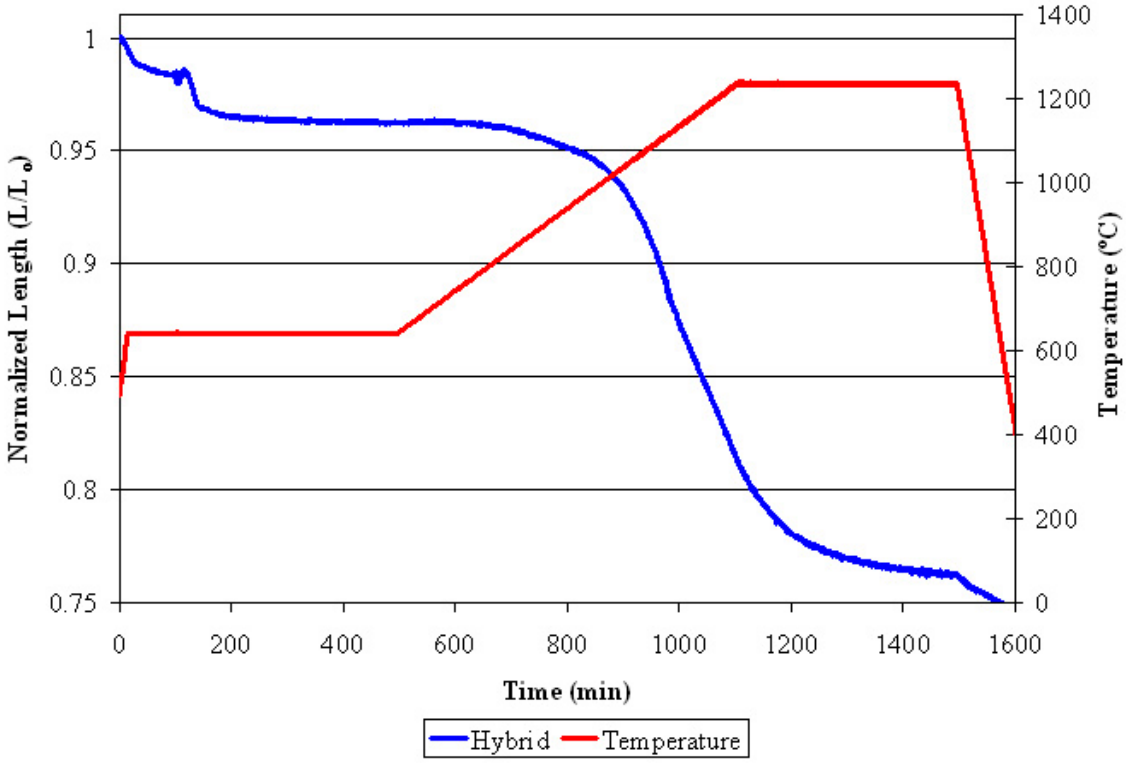

Figure IV.5: Constrained sintering curve of Hybrid Fe39Ni8Cr, ScSz system with isothermal hold during reduction, but prior to sintering. Artifact near 200 minutes assumed to be from specimen shape. All runs were performed in 387 sccm Ar + 4% H_2.

The developed model is strongly based upon the observed behaviors of the Fe39Ni8Cr and ScSz material system. However, the approach used to develop the model is general and can be used for any two material systems. If there is not adequate time to develop such a comprehensive model, but the predictive capabilities of the model are still desired, it is envisioned that the current set of material parameters could be modified to account for different iron alloy and zirconia based materials with just a few experiments, and a slight increase in model error. For example, if a modified thermal expansion coefficient and a single unconstrained free sintering curve (measured at a reasonable temperature ramp rate of 3 to 8 °C/min) were obtained, then the shrinkage behavior of the

material could be well characterized. Specifically, the sintering curve would most likely exhibit similar trends to the tested ScSz or Fe39Ni8Cr systems, just taking place at higher or lower temperatures. Therefore, the β and τ curves could be shifted in temperature and scaled in magnitude (the parameters most likely would not need to be scaled with temperature because particle size and solids loading will be similar to the experiments) until they predict a similar shrinkage to the observed shrinkage. The inherent assumption here is that the thermal expansion and sintering behavior of the materials is more radically affected with changes in material composition then the relaxation behavior which is a considered to be primarily a property of the bulk material (iron or zirconia).

IV.4 Conclusions and Applications for Model

The majority of the useful information will come after the model can be fully integrated and applied to different geometries. However, several interesting conclusions can be drawn just on the work to this point. First of all, the duration of the high temperature hold time that is required for the ScSz system to anneal the stresses that developed during constrained sintering can be crudely estimated with several simplifying assumptions. Specifically, if temperature and relative density are held constant, if the only mode of relaxation is assumed to be the bulk viscous flow of the ScSz system, if the stress in the constrained system is assumed to be due to a total sintering strain mismatch of 2% (which must be relaxed through viscous flow), and if the bulk viscous relaxation is driven by a constant hydrostatic driving stress of 1 MPa (which is on the order of the sintering potential), then the time required for the ScSz system to relax the stresses can be

estimated. With the above assumptions, Equations (III.15) through (III.18) can be rewritten as

$$\text{time} = \frac{\varepsilon}{\dot{\varepsilon}} \approx K_p\left(\bar{\rho},T\right)\frac{\varepsilon}{\sigma_m} \quad . \tag{IV.1}$$

Where 'time' represents the duration of the high temperature isothermal hold period required for the ScSz system to relax a fixed mismatch in sintering and reduction strains (ε) between the two constrained systems and is assumed to be 0.02, K_p is the temperature and relative density dependent bulk viscosity of the ScSz system, and σ_m is assumed to be constant, and the only hydrostatic stress present in the constrained system (roughly representative of the sintering potential) and was assumed to be 1 MPa. Solving Equation (IV.1) with the given assumptions under several different temperature and relative density conditions resulted in Figure IV.6.

Second, the cool-down temperature at which the ScSz system can viscously flow enough to fully relax stresses that develop in the constrained hybrid system can be estimated from Equations (III.15) through (III.18) with several simplifying assumptions. Assuming that the peak isothermal hold time is long enough to completely anneal the structure, then the rate of viscous relaxation must be equal to the mismatch in thermal expansion strain imparted by the constrained system upon cool down to relax the structure. Assuming only bulk viscous flow took place, then the following equation can be written from Equation (III.15).

$$\dot{\varepsilon}^{v} = \left(\overline{\alpha}_{Fe} - \overline{\alpha}_{ScSz}\right)\frac{dT}{dt} = \frac{\sigma_m}{K_p\left(\overline{\rho}\right)} \qquad \text{(IV.2)}$$

Where $\overline{\alpha}_{Fe}$ and $\overline{\alpha}_{ScSz}$ are the average thermal expansion coefficients of Fe39Ni8Cr and ScSz respectively, dT/dt is the cool down temperature ramp rate, σ_m is the average hydrostatic stress that the structure is assumed to be 'relaxed' at and was chosen to be 1MPa, K_p is the relative density dependent bulk viscosity as defined in Equation (III.16). Figure IV.7 shows the relaxation temperature of the ScSz system as a function of temperature cool down rate, and final relative density of the ScSz. The relaxation temperature assuming only viscous flow due to shear stresses was almost identical to that shown in Figure IV.7 if the 'relaxed' shear stress was considered to be 0.5 MPa instead of 1 MPa.

Third, the temperature at which the Fe39Ni8Cr system has the ability to relieve stresses can be bracketed using information from Figures II.30 and II.28. Specifically, no temperature effects were noticed in the 360 °C uniaxial test, while a slight relaxation was noticed in the 575 °C relaxation test. Therefore, it can be stated that the Fe39Ni8Cr system has some ability to relieve residual stresses in the constrained hybrid structure at temperatures as low as 575 °C.

Finally, the evolution of density in the unconstrained Fe39Ni8Cr system during reduction can be estimated using the equations developed in Chapter III as shown in Figures IV.8 and IV.9. From Figures IV.8 and IV.9 it is apparent that reduction in the given compact system ends up being almost a constant density process.

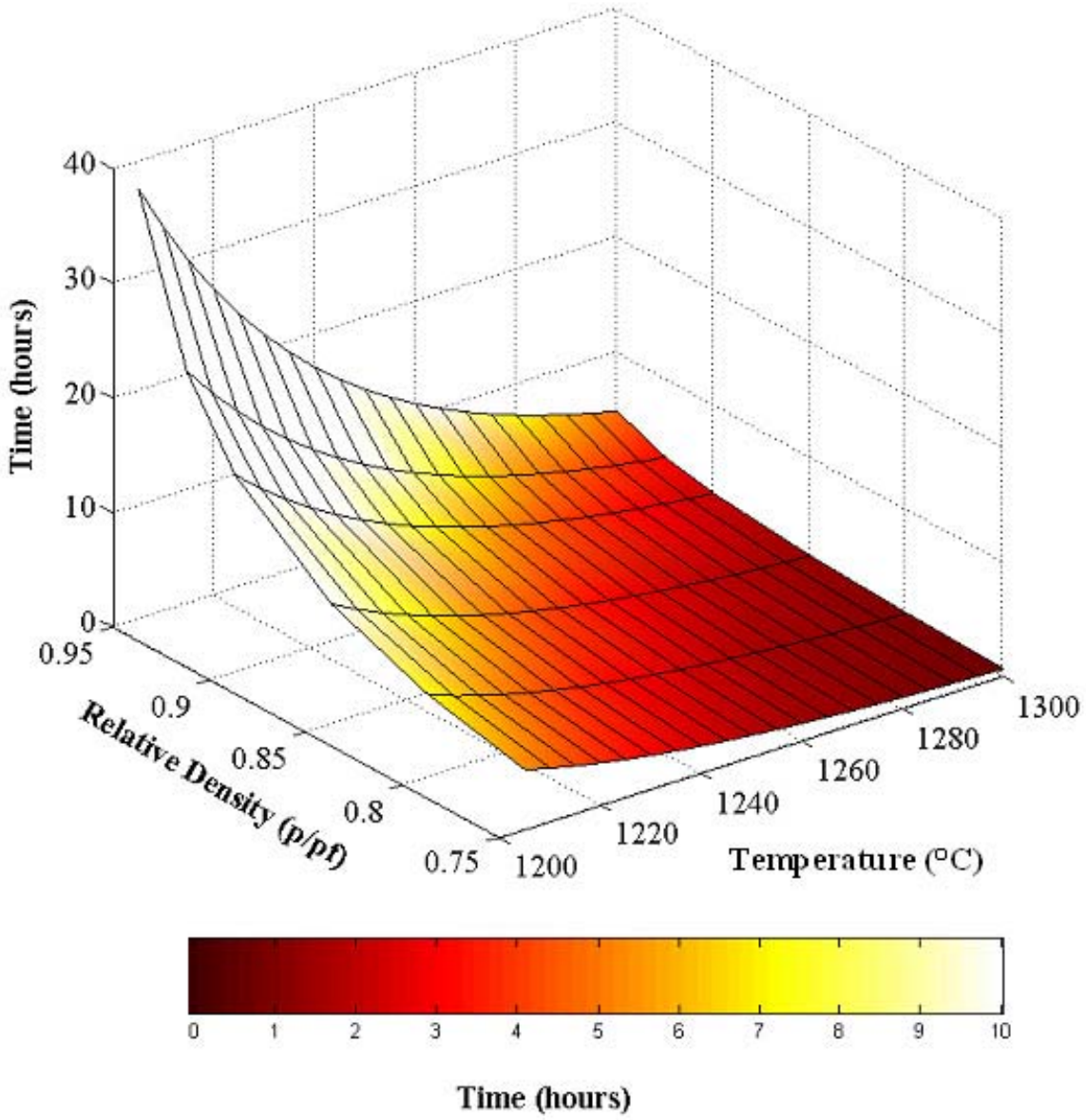

Figure IV.6: Estimated time required for ScSz system to relax 2% strain under 1 MPa hydrostatic driving stress at a constant temperature assuming only bulk viscous flow.

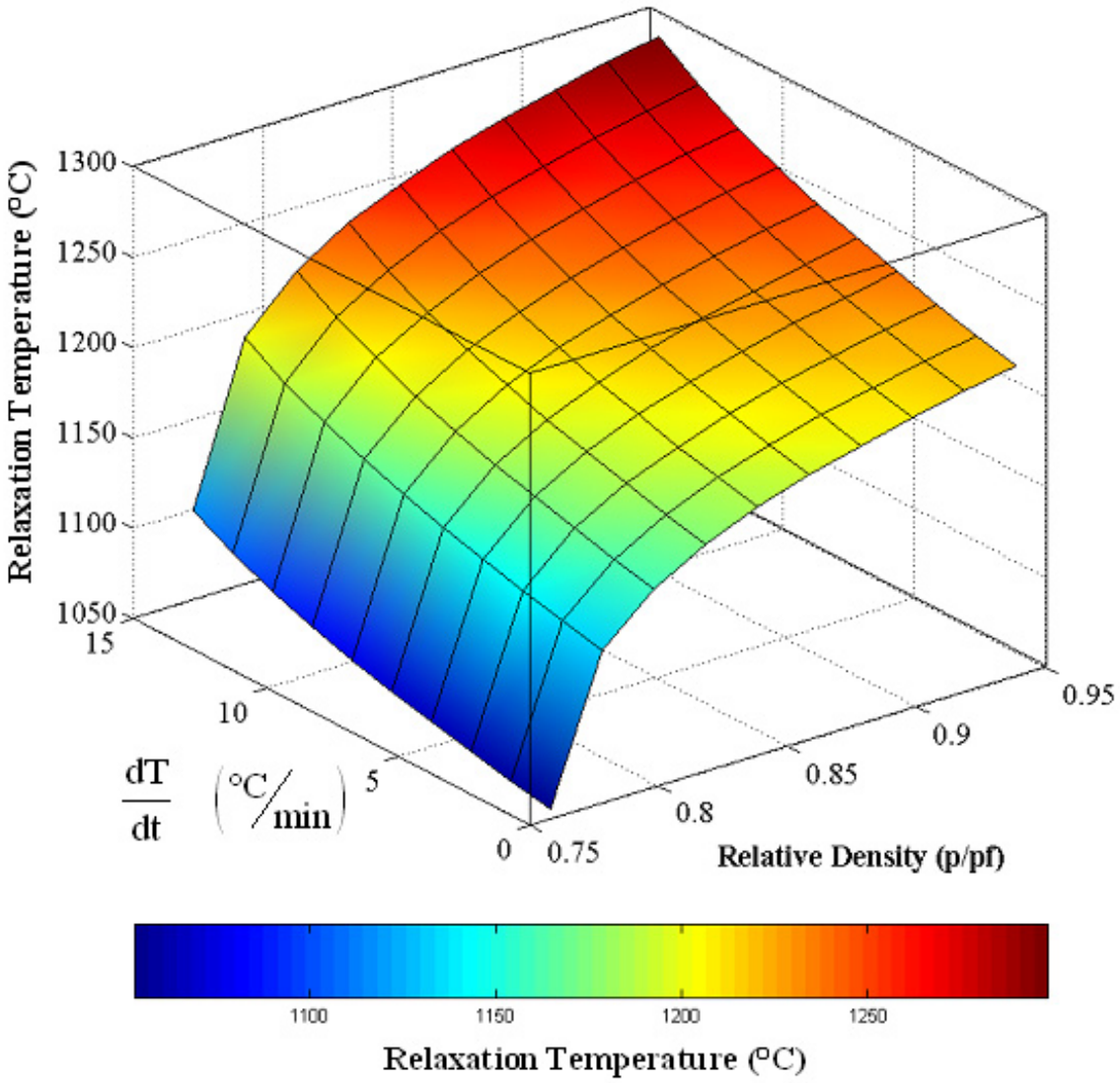

Figure IV.7: Estimated relaxation temperature of ScSz as a function of cool down temperature ramp rate and final relative density assuming a mean hydrostatic stress of 1 MPa is 'relaxed'.

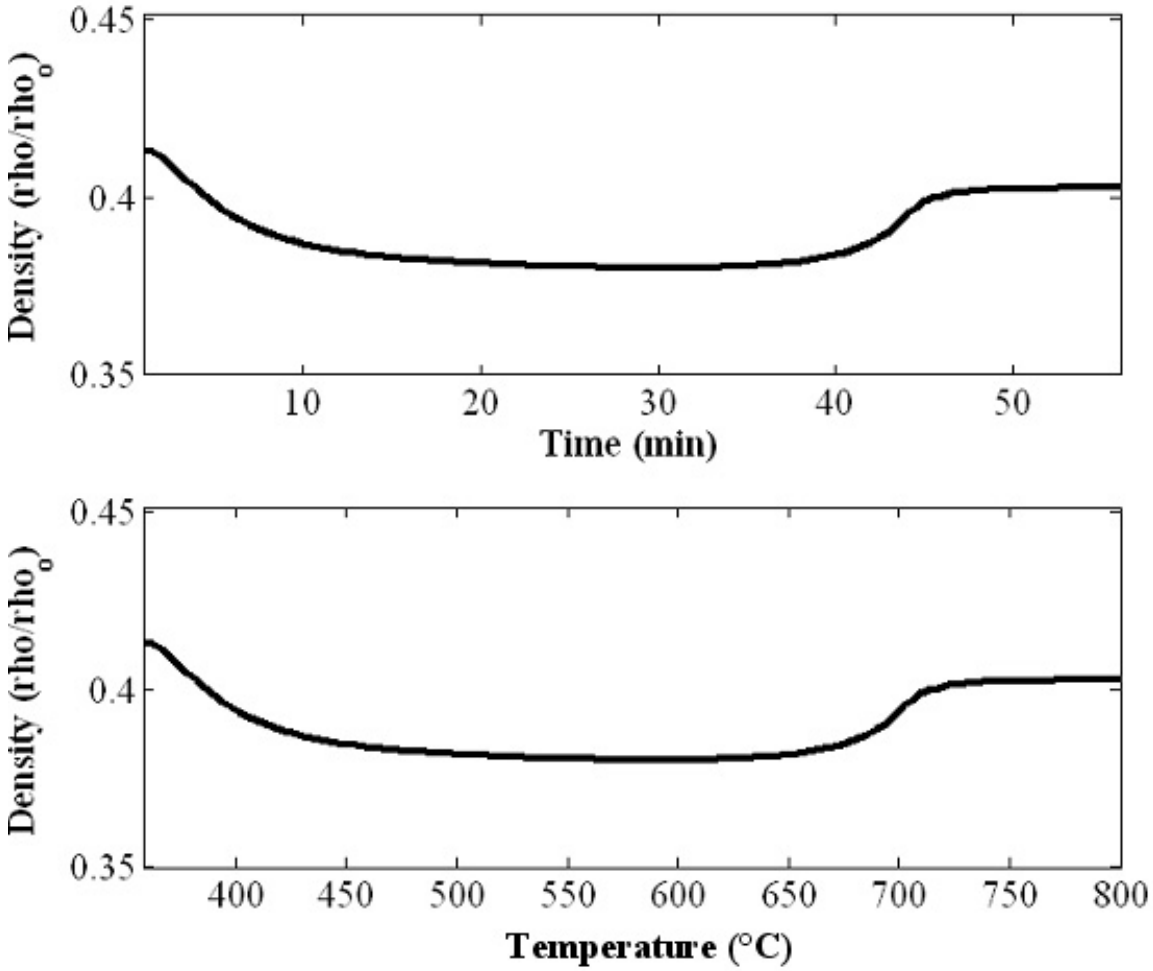

Figure IV.8: Modeled evolution of density in unconstrained reducing Fe39Ni8Cr sample being heated at 8 °C/min from 350 °C to 800 °C in 387 sccm Argon + 4% H_2. No substantial sintering had taken place, and the material was 88% reduced by 800 °C.

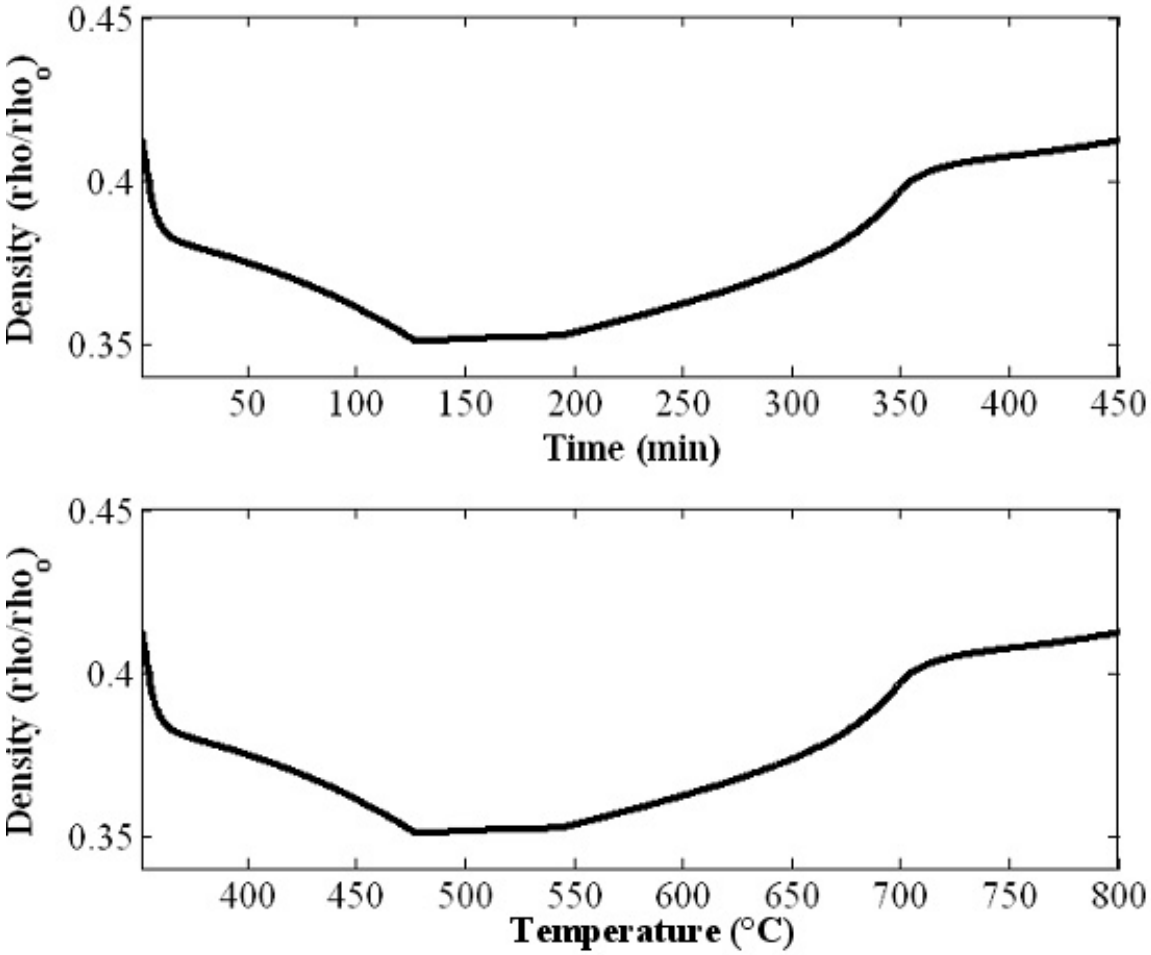

Figure IV.9: Modeled evolution of density in unconstrained reducing Fe39Ni8Cr sample being heated at 1 °C/min from 350 °C to 800 °C in 387 sccm Argon + 4% H_2. Slight sintering was occurring over 710 °C, and the material was 100% reduced by 542 °C.

Several applications for the model are foreseen after the model has been numerically implemented and validated. The first task would be to accurately determine the temperature where the stresses in the structure are fully annealed for a given temperature profile. Another possible application would be to investigate how the mismatch in sintering rates affects final porosity in the sample. Yet another possible application would be to determine an optimum heating schedule to minimize residual stresses and manufacturing stresses. The model could also be used to predict the affects

of different SOFC geometries on the stress level in the manufactured samples. In general, the model can be used to simulate the evolution of stresses in the SOFC body for any desired geometry under an array of different processing conditions. This concludes the yearlong study on SOFCs.

APPENDIX

The following is the derivation of the unconstrained densification rate of a sintering compact as published by C. Hsueh et al. in 1986 .(C. H. Hsueh 1986). Further manipulations were performed in the body of the 1986 paper that combined and rearranged terms until the form reported in Equation (III.9) was arrived at. However, to be concise only the generalized derivation is shown.

16. J. M. Vieira and R. J. Brook, *J. Am. Ceram. Soc.* **67,** 245 (1984).
17. J. M. Vieira and R. J. Brook, *J. Am. Ceram. Soc.* **67,** 450 (1984).
18. J. R. Porter, W. Blumenthal and A. G. Evans, *Acta metall.* **29,** 1899 (1981).
19. R. Raj and M. F. Ashby, *Metall. Trans.* **2,** 1113 (1971).
20. Z. Hashin, *J. appl. Mechan.* **29,** 143 (1962).
21. D. P. H. Hasselman, *J. Am. Ceram. Soc.* **45,** 140 (1962).
22. S. Timoshenko and J. N. Goodier, *Theory of Elasticity*, McGraw-Hill, New York (1951).
23. G. E. Mase, *Schaum's Outline Series: Theory and Problem of Continuum Mechanics*. McGraw-Hill, New York (1970).
24. R. M. Cannon, W. H. Rhodes and A. H. Heuer, *J. Am. Ceram. Soc.* **63,** 46 (1980).
25. C. Ostertag, Ph.D. thesis, Univ of California, Berkeley, To be published.
26. J. D. Eshelby, *Proc. R. Soc.* **A241,** 376 (1957).
27. R. M. Cannon. To be published.
28. C. Herring, *The Physics of Powder Metallurgy* (Edited by W. E. Kingston) (1951).

APPENDIX

The driving force for sintering: the "sintering stress"

The driving force for sintering is evaluated by assessing chemical potential gradients in the system. For this purpose, it is convenient to firstly consider atoms on the surface adjacent to the grain boundaries at 0 and 0′ [Fig. 13(a)]. Such atoms have a chemical potential dictated by the curvature of the surface [19, 27, 28].

$$\mu = \mu_0 + \gamma_s \Omega [1/R_1 + 1/R_2] \tag{A1}$$

where μ_0 is the standard chemical potential of the material, Ω is the atomic volume γ_s is the surface energy, R_1 is the in-plane radius of curvature [Fig. 13(a)] and R_2 is the out-of-plane radius of curvature.

Atoms on the grain boundaries, between 0 and 0′ derive their chemical potential from the stress *normal* to the grain boundary and from the grain boundary energy, γ_b [27, 28]. A useful approximation is

$$\mu \approx \mu_0 + \sigma^n \Omega + 2\gamma_b \Omega / l \tag{A2}$$

where l is the grain facet length (Fig. 13). The stress term derives directly from the work done by the local stress when an atom is added to the grain boundary [28]. The grain boundary energy term arises, because the grain size increases when an atom is added to a grain boundary [27]. The grain size change is most easily appreciated by assessing the response that accompanies addition of an atom to the boundaries of the grain array depicted in Fig. 13b. This process increases the average grain size from l to $l + 2\delta$ [Fig. 13(b)], such that the volume of matter added to a cube of material of side, d—which must equate with the atomic volume—is given by

$$6\delta l^2 (d/l)^3 = \Omega \tag{A3}$$

whereupon

$$\delta = \Omega l / 6d^3. \tag{A4}$$

The corresponding change in grain boundary area, ΔA, is

$$\Delta A = 3[(l + 2\delta)^2 - l^2](d/l)^3$$

$$= 12\delta l (d/l)^3 \tag{A5}$$

Substituting δ from equation (A4), then gives

$$\Delta A = 2\Omega / l. \tag{A6}$$

The change in grain boundary area represents a net energy increase, by virtue of the grain boundary energy γ_b, such that

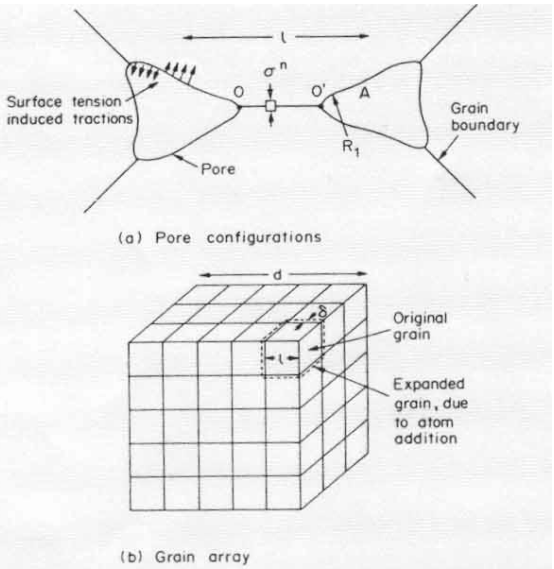

Fig. 13. Schematics of (a) the pore configuration and (b) the grain array used to describe the "sintering stress" and the body stress in a porous compact.

the associated chemical potential per atom becomes

$$\Delta\mu = \Delta A\, \gamma_b$$

$$= 2\Omega\gamma_b / l \tag{A7}$$

as expressed in equation (A2). Other geometries consistently yield the grain diameter as the pertinent dimension [27].

Further progress is achieved by recognising that continuity of chemical potential requires identical potentials on the surface and on the grain boundary at the junctions 0 and 0′. Consequently, the normal stress on the boundary, at the junction σ_0^n, becomes†

$$\sigma_0^n = -\gamma_s \kappa_0 + 2\gamma_b / l \tag{A8}$$

where κ_0 is the net pore curvature at 0 and 0′ ($\kappa = 1/R_1 + 1/R_2$). The stress σ_0^n can be used in conjunction with the usual flux relations and boundary conditions to evaluate the sintering rate [4, 19]. Specifically, symmetry requirements of the grain facet center ($d\sigma/dx = 0$), coupled with the flux relation $J = -(D/kT)(d\mu/dx)$], used in association with the mean stress on the grain array σ_m, yield a grain center approach rate

$$\dot{\delta} \sim D(\Sigma - \sigma_m) l^{-b} \tag{A9}$$

where $\Sigma = (\gamma_s \kappa_0 + 2\gamma_b / l)$ and b is a coefficient ≈ 2 or 3. Matter conservation requirements are then imposed

$$\dot{V} \sim \dot{\delta} l^2 \tag{A10}$$

to give a pore volume change rate

$$\dot{V} \sim D(\Sigma - \sigma_m) l^{-1} \tag{A11}$$

Finally, noting that the relative density change rate is related to the pore volume by

$$\dot{\rho} \sim (\dot{V}/l^3)\rho_f \tag{A12}$$

the sintering rate becomes [4, 19, 27]

$$\dot{\rho} \sim D(\Sigma - \sigma_m) l^{-a}, \tag{A13}$$

with $a = b + 1$.

Furthermore, since some regions will become fully dense while $\rho < \rho_f$. $\dot{\rho}$ must be qualified by the number of pores per grain, n, whereupon

$$\dot{\rho} = ng(\rho)(1 - \sigma_m/\Sigma) l^{-a} \tag{A14}$$

where $g(\rho)$ is weakly dependent on density [27].

†Though not strictly correct, equation (A8) provides a convenient means of illustrating the terms that dictate Σ in equation (A9).

The quantity Σ, which constitutes the net *driving force* for sintering, when conditions of zero stress ($\sigma_m = 0$) obtain, derives solely from *chemical potential* considerations. However, since Σ has units of stress, it has generally been termed the "sintering stress", even though elastic strains, indicative of the existence of an actual stress in the system of magnitude Σ, are not present.

The surface tension at the pore surface provides a distinctly different contribution to sintering than the "sintering potential" Σ. Surface tension induces an actual net mean stress within the sintering body, which superposes directly onto other sources of stress. Surface tensions within a thin surface layer impose normal tractions on the underlying body. When conditions of rapid surface diffusion obtain (typical of sintering temperatures), the tractions σ have magnitude,

$$\sigma = \gamma_s \kappa \tag{A15}$$

where κ is the surface curvature, as depicted in Fig. 13(a). Note that the tractions at 0 and A are of opposite sign by virtue of the change from concave to convex curvature of the pore surface. These tractions induce an actual mean stress in the body, which will be referred to as a *body stress*, σ_b. For spherical pores, radius R, the magnitude of σ_b is readily computed. The tractions created by the surface tension then have uniform magnitude, $\sigma = 2\gamma_s/R$. Furthermore, since the imposed mean stress is zero, the body stress must satisfy the mechanical equilibrium relation [13]. Thus, when grain boundary tensions are neglected

$$\sigma_b(1-f) + (2\gamma_s/R)f = 0 \tag{A16}$$

where f is the volume fraction of pores whereupon

$$\sigma_b = -2\gamma_s f/R(1-f). \tag{A17}$$

A *compressive* body stress is thus created. Clearly, σ_b has a very different form than Σ.

For pores of complex shape, such as that depicted in Fig. 13(a), R in equation (A17) is replaced by a radius of curvature integrated over the pore surface, $\langle R_c \rangle$. The radius of curvature involved in Σ (those at the junction 0) and in σ_b (integrated over the pore surfaces) are thus very different.

Finally, it is emphasized that actual stresses are also generated during sintering in the presence of heterogeneity. These stresses are termed *heterogeneity stresses*. Inside the heterogeneity the mean stress σ_m is spatially uniform, at least when the heterogeneity exhibits ellipsoidal symmetry [26].

REFERENCES

(2002). Fuel Cell Handbook, 6th ed. S. C. f. N. Gas. Morgantown, W.Va, U.S. Dept. of Energy, National Energy Technology Laboratory.

A. Atkinson, a. A. S. (2000). "Mechanical Behavior of Ceramic Oxygen Ion-Conducting Membranes." Solid State Ionics **134**: 59-66.

A. Jagota, K. R. M., and R. K. Bordia (1990). "Isotropic Constitutive Model for Sintering Particle Packings." J. Am. Ceram. Soc. **73**(8): 2266-2273.

B. J. Dalgleish, E. S., A. P. Tomsia, R. M. Cannon, and R. O. Ritchie (1994). "Interface Formation and Strength in Ceramic-Metal Systems." Scripta Metallurgica et Materialia **31**(8): 1109-1114.

B. Sudhir, a. A. H. C. (2001). "Compression Creep Characteristics of 8-mol%-Yittria-Stabilized Cubic Zirconia." J. Am. Ceram. Soc. **84**(11): 2625-2632.

Bammann, D. J. (1990). Modeling the Temperature and Strain Rate Dependent Large Deformation of Metals. Applied Mechanics Reviews.

Bhardwaj, M. (1986). "Principles and Methods of Ultrasonic Characterization of Materials." Advanced Ceramic Materials **1**: 311-323.

Bocchini, G. F. (1986). "The Influence of Porosity on the Characteristics of Sintered Materials." International Journal of Powder Metallurgy **22**(3): 185-202.

C. H. Hsueh, A. G. E., R. M. Cannon, and R. J. Brook (1986). "Viscoelastic Stresses and Sintering Damage in Heterogeneous Powder Compacts." Acta Metall **34**(5): 927-936.

Chakraborty, A. (1999). "Kinetics of the reduction of hematite to magnetite near its Curie transition." J. of Magnetism and Magnetic Materials **204**: 57-60.

Church, B. (2004). Inquiry into Coefficient of Thermal Expansion for Various Materials. P. Eisele. Atlanta**:** Recieved spreadsheet with measured %expansion of a variety of iron and zirconium based materials.

Church, B. C. (2002). High Conductivity Alloys for Extruded Metallic Honeycomb. Material Science and Engineering. Atlanta, Georgia, Georgia Institute for Technology.

Clark, J. L. (1999). Stainless Steel Hollow Sphere Foams: Processing and Properties. Material Science and Engineering. Atlanta, Georgia Institute of Technology.

Cocks, A. C. F. (1989). "Inelastic Deformation of Porous Materials." Mechanics and Physics of Solids **37**: 693-715.

D. J. Bammann, M. L. C., M. F. Horstemeyer, and L. I. Weingarten (1993). Failure in Ductile Materials Using Finite Element Methods. New York, Appl. Sci. Publ.

E. B. Marin, a. D. L. M. (1996). "Associative Versus Non-Associative Porous Viscoplasticity Based on Internal State Variable Concepts." International Journal of Plasticity **12**(5): 629-669.

E. B. Marin, a. D. L. M. (1998). "Models for Compressible Elasto-Plasticity Based on Internal State Variables." International Journal of Dammage Mechanics **7**(1): 47-83.

F.P.F. van Berkel, L. S. S., G.M. Christie (1999). Production of synthesis gas using SOFC technology. Proceedings of Solid Oxide Fuel Cells, Honolulu, HI, USA, Electrochem Soc.

Haase, J. W. E. a. K. (1976). "Measurement of the Rate of Reduction Reactions by the Torsion Technique." High Temperature Science **8**: 167-177.

Hayes, S. P. M. a. P. C. (1990). "In Situ Observations of the Gaseous Reduction of Magnetite." Metallurgical Transactions B **21B**: 141-151.

Hiroshi Mori, C.-J. W., Junichiro Otomo, Koichi Eguchi, and Hiroshi Takahashi (2003). "Investigation of the interaction between NiO and yittria-stabilized zirconia (YSZ) in the NiO/YSZ composite by temperature-programmed reduction technique." Applied Catalysis **245**: 79-85.

Huijsmans, G. M. C. a. J. P. P. (1997). State of the art SOFC component development at ECN. Proceedings of SOFC Meeting, Aachen, Germany, Electrochem. Soc.

Hurysz, K. (2003). Inquiry into Tensile Fracture Strength of Green Compacts. P. Eisele. Atlanta**:** Recieved spreadsheet from Dr. Hurysz with MOR data for 3mm in diameter cylindrical green compacts.

J. L. Clark, K. M. H., T. McCoy, R. Oh, and J. Cochran (In Press). Improving Binder Distribution in Extruded Ceramic Paste. Acers 105th Annual Meeting, Opryland, Tennesee.

J. M. McNaney, R. M. C., and R. O. Ritchie (1994). "Near-Interfacial Crack Trajectories in Metal-Ceramic Layered Structures." International Journal of Fracture **66**: 227-240.

Johnson, L. (2003). Finding and Utilizing the Master Sintering Curve, Northwestern University, Material Science and Engineering.

K. R. Venkatachari, a. R. R. (1986). "Shear deformation and Densification of Powder Compacts." J. Am. Ceram. Soc. **69**(6): 499-506.

K.S. Chan, S. R. B., K.P. Walker, and U.S. Lindholm (1984). A survey of unified constitutive theories. Second Symposium on Nonlinear Constitutive Relations for High Temperature Applications, NASA Lewis Research Center.

Kalpakjian, S., Schmid, and Steven (2003). Manufacturing Processes for Engineering Materials 4th ed. New Jersey, Prentice Hall.

Keyence (2001). User's Manual High Speed, High Precision Digital Micrometer LS-7500 Series. Osaka, Japan.

L. Chandra, R. P. T., E. P. Busso, and G. A. Webster (1997). Prediction of Stresses Generated During Sintering of a Constrained Thin Film. Thin-Film-Stresses and Mechanical Properties VII. Symposium, Boston, MA, USA, Mater. Res. Soc.

Li, S. N.-N. a. Y. F. (1992). "A new explicit algorithm for finite deformation elastoplasticity and elastoviscoplasticity: performance evaluation." Computer Structure **44**: 937-963.

Lu, G. Q. M. (1996). "Evolution of the pore structure of a ceramic powder compact during sintering." Materials Processing and Technology **59**: 297-302.

M. D. Sacks, a. T. T. (1984). "Preparation of SiO2 Glass from Model Powder Compacts: II, Sintering." J. Am. Ceram. Soc. **67**(8): 532-537.

M. Ortiz, a. J. C. S. (1986). "An Analysis of a new class of integration algotrithms for elastoplastic constitutive relations." international Journal of Numerical Methods in Engineering **23**: 353-366.

Malvern, L. E. (1969). Introduction to the Mechanics of a Continuous Medium. Upper Saddle River, NJ, Prentice-Hall, Inc.

McDowell, D. L. (1992). "A Nonlinear Kinematic Hardening Theory for Cyclic Thermoplasticity and Thermoviscoplasticity." International Journal of Plasticity **8**: 695-728.

Meyers (1994). Dynamic Behavior of Materials. Ontario, Interscience**:** Chapter 2. Elastic waves.

Nadler, J. (2003). The Hydrogen Reduction of Iron and Chromium Oxides. Material Science and Engineering. Atlanta, Georgia Institute of Technology.

Nguyen, Q. M., Takahashi, and Takehiko (1995). Science and technology of ceramic fuel cells. Amsterdam, Sara Burgerharts.

O. Kubaschewski, E. L. L. E. (1979). Metallurgical Thermochemistry 5th edition. Elmsford, NY, Pergamon. http://www-engr.sjsu.edu/ellingham/

P. Z. Cai, G. L. M., and D. L. Green (1997a). "Constrained Densification of Alumina/Zirconia Hybrid Laminates, II: Viscoelastic Stress Computation." J. Am. Ceram. Soc. **80**(8): 1940-1948.

P. Z. Cai, G. L. M., and D. L. Green (1997b). "Determination of the Mechanical Response of Sintering Compacts by Cyclic Loading Dilatometry." J. Am. Ceram. Soc. **80**(2): 445-452.

P.E. Evans, Y. Y. C. i. Y. (1970). "Creep in Yttria- and Scandia-Stabilized Zirconia." J. Am. Ceram. Soc. **53**(7): 365-369.

Perzyna, P. (1966). "Fundamental problems in viscoplasticity." Advances in Applied Mechanics **9**: 243-377.

R. K. Bordia, a. G. W. S. (1988a). "On Constrained Sintering - I Constitutive Model for a Sintering Body." Acta Metall **36**(9): 2393-2397.

R. K. Bordia, a. G. W. S. (1988b). "On Constrained Sintering - II Constitutive Model for a Sintering Body." Acta Metall **36**(9): 2399-2409.

R. O. Ritchie, R. M. C., B. J. Dalgleish, R. H. Dauskardt, and J. M. McNaney (1993). "Mechanics and Mechanisms of Crack Growth at or Near Ceramic-Metal Interfaces: Interface Engineering Strategies for Promoting Toughness." Materials Science and Engineering A **A166**: 221-235.

R. Raj, a. R. K. B. (1984). "Sintering Behavior of Bi-Modal Powder Compacts." Acta Metall **32**: 1003.

Scherer, G. W. (1977). "Sintering of Low-Density Glasses: I & II, Theory." J. Am. Ceram. Soc. **60**(5,6): 236-246.

Shaw, N. J. (1989). "Densification and Coarsening During Solid State Sintering of Ceramics: A Review of the Models." Powder Metallurgy International **21**(3): 16-33.

Tuller, H. L. (2003). Electroceramics: Application to Solid Oxide Fuel Cells, Materials Science and Engineering, Massachusetts Institute of Technology.

Y. Du, N. M. S., G. A. Tompsett, D. Zhang, J. Swan, and M. Bowden (2003). "Extruded Tubular Strontium and Magnesium Doped anthanum Gallate, Gadolinium Doped Ceria, and Yittria Stabilized Zirconia Electrolytes." J. of the Electrochemical Society **150**(1): A74-A78.